Super-resolution Wide-field Optical Microscopy by use of Evanescent Standing Waves

by

Euiheon Chung

M.S. Aerospace Engineering
Korea Advanced Institute of Science and Technology, 1998

Submitted to the Harvard-Massachusetts Institute of Technology
Division of Health Sciences and Technology
in partial fulfillment of the requirements for the degree of

Doctor of Philosophy
in Biomedical Engineering and Mechanical Engineering
at the
MASSACHUSETTS INSTITUTE OF TECHNOLOGY

February 2007

MASSACHUSETTS INSTITUTE OF TECHNOLOGY
FEB 2 1 2007
LIBRARIES

© 2007 Massachusetts Institute of Technology. All rights reserved.

Signature of author: _____
Harvard-MIT Division of Health Sciences and Technology
February, 2007

Certified by: _____
Peter T. C. So
Professor of Mechanical Engineering and Biological Engineering
Thesis Supervisor

Certified by: _____
Michael S. Feld
Professor of Physics
Director of G. R. Harrison Spectroscopy laboratory

Certified by: _____
George Barbastathis
Esther and Harold Edgerton Associate Professor of Mechanical Engineering

Certified by: _____
Paul Matsudaira
Professor of Biology and Biological Engineering

Accepted by: _____
Martha L. Gray
Edward Hood Taplin Professor of Medical and Electrical Engineering
Director, Harvard-MIT Division of Health Sciences and Technology

ARCHIVES

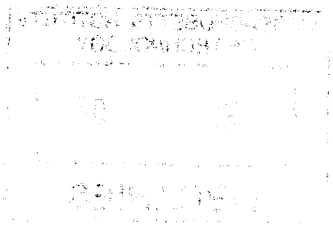

ARCHIVES

Super-resolution Wide-field Optical Microscopy by use of Evanescent Standing Waves

By

Euiheon Chung

Submitted to the Harvard-Massachusetts Institute of Technology
Division of Health Sciences and Technology on January 11, 2007 in partial fulfillment of
the requirements for the degree of Doctor of Philosophy
in Biomedical Engineering and Mechanical Engineering

ABSTRACT

The development of high resolution, high speed imaging techniques allows the study of dynamical processes in biological systems. Optical fluorescence microscopy is an essential tool for investigations in many disciplines in biology and medicine with molecular specificity. The resolution of optical far-field microscopy has been limited by the wave nature of light. In this thesis, a microscopy technique, standing wave total internal reflection fluorescence (SW-TIRF), has been developed with resolution beyond the classical diffraction limit. The SW-TIRF approach modifies the point-spread function to effectively decrease the excitation wavelength by utilizing an evanescent standing wave, carrying high spatial frequency information near the interface between the specimen and a high refractive index substrate. Evanescent standing wave illumination is used to generate a sinusoidal, high-spatial frequency, fringe pattern on the specimen providing lateral resolution enhancement. Furthermore, the less than 100 nm penetration depth of the evanescent field from the substrate ensures a thin excitation region resulting in low background fluorescence. The first experimental realization of SW-TIRF in an objective-launched geometry demonstrates the potential for super-resolution imaging at high speed in wide-field microscopy. The super-resolution has been realized with the effective point-spread function providing better than a fifth of the emission wavelength or approximately 100 nm, which is better than twice that of conventional microscopy. In addition, imaging biological specimens with SW-TIRF demonstrated the performance revealing the fine actin cytoskeleton structures of fibroblasts. On the other hand, the surface plasmons induced by evanescent fields at a specific angle can generate an enhanced electric field which can effectively excite fluorophores near a metal coated surface. We observed a unique doughnut-shaped point-spread function of surface plasmon coupled emission and explained it with theoretical modeling using vector field theory. The combination of surface plasmon resonance fluorescence imaging and SW-TIRF resulted in a novel high-resolution microscopy, the standing wave surface plasmon resonance fluorescence (SW-SPRF) microscopy. These findings may allow super-resolution imaging with even higher sensitivity and signal-to-noise ratio at high imaging speed.

Thesis Supervisor: Peter T. C. So
Title: Professor of Biological Engineering and Mechanical Engineering

Acknowledgements

It is my fortune to have Professor Peter So as my thesis advisor. He introduced me to the wonderland of biomedical optics and has been mentoring me throughout the course of my PhD research. I am most grateful for his passion, smile, faith, and endless encouragement.

Professors Michael S. Feld, George Barbastathis, and Paul Matsudaira generously took the role of my thesis committee and shared their expertise and kept me on the right track with enlightening discussions and invaluable suggestions. Their insightful questions and constructive advices have been very helpful for me to build a perspective in the field where engineering, science, biology, and medicine are converging.

Also I am grateful to Professor Matt Lang for giving his hands whenever I have questions in optical instrumentation. I learned much of microscopy from Professor Colin Sheppard in his course. Dr. Mattias Nagorni has shared his expertise on the deconvolution methods via emails. Dr. Juhyun Park and Sunyoung Lee helped me to prepare surface plasmon samples and to examine the samples with atomic force microscope.

Much of my thanks goes to members of Peter So laboratory. The inspiring and collaborative atmosphere in our lab allowed me to learn the joy of sharing expertise and knowledge. Dr. Barry Masters served as a role model by showing what is it to be a scholar. In particular, Daekeun Kim helped me not only with electronics instrumentation but also with sparkling discussions. Hyuk-Sang Kwon never hesitated to give his hands whenever I need. Maxine Jonas taught me how to culture cells and demonstrated how to be organized and effective. Hayden Huang has provided thoughtful mentoring with his humor. Yang-Hyo Kim proved to be an excellent helper for many experiments. Sharing joys and struggles with Heejin Choi, Jaewon Cha, Dimitrios Tzeranis, Karsten Bahlman, Timothy Ragan, and Jason Sutin in the So laboratory left me a great memory of MIT life. In addition, I would also like to acknowledge the former members of our laboratory - Ki Hean Kim, Lily Laiho, Judith Su, Serge Pelet, Michael Previte, and Siavash Yazdanfar - without whom I could not have grown as a researcher.

It has been a great pleasure for me to have chance to work with visiting scientists from various parts of the world. Interacting and helping with Carson Y. Y. Chen, Tiger Wen-Lin Bee, Wanrong Gao, Yan Cui, Rui rong Wang have been fun and rewarding. Especially, Wai Teng Tang has remained as a brilliant collaborator even after he returned to Singapore.

Working in an open environment at 500 Technology Square, I found it very helpful to interact and exchange experiences with various group members from the laboratories of Professors Paul Matudaira, Matt Lang, Peter Dedon, and Roger Kamm. Particularly, James G Evans and Victor Horodincu generously provided murine macrophage cells and helped finding out biological problems. I thank Winston Timp and Alec Robertson for their help with quantum dot and actin filament imaging. Also Junghyun Son helped with basic biochemical techniques.

Time spent with my friends in the Korean Graduate Student Association, especially – Chulmin Joo, Junsang Doh, Wonshik Choi, Yongkeun Park, Kwonmoo Lee, Jinkuk Kim, Hyungsuk Lee, Kyu Jin Cho, and Soohyung Kim - those who shared academic and nonacademic interest together.

My HST fellows have added vitality in my graduate life. In particular, I appreciate Cathy Modica's warmth and encouragement; the friendship with Nikola Kojic, Caroline Boudoux, Blanca Himes, David Nguyen, Grace Y. Kim, Taro Muso, Timothy Lu, Jenny Mu, Juwell Wu, Austin Huang, David Cochran, Josh Tam, Lisa Treat, Adam Siegel, Rajiv Saigal, Kenneth Roach, Kristy Shine and Kathleen Sienko. I had the privilege of having such well-rounded friends during the journey between Harvard and MIT.

I cannot fully express my life mentor, Moonhee Kim, along with Jaeyeon Jung and Yunseung Kim for their pursuit of finding another aspect of truth in our lives.

This thesis would not have been possible without my family's unconditional love and caring support. My wife, Hyejun Park, has been my life partner and our adorable girl, Haewon, has been the source of blessing to us as her name literally means. You have given me the meaning of my life. I also thank our parents and my twin brother, Euiyeop Chung, a life time alter ego, for their faith and encouragement, and I dedicate this thesis to them.

TABLE OF CONTENTS

LIST OF FIGURES

LIST OF TABLE

LIST OF ABBREVIATIONS

AFM: atomic force microscopy
CCD: charge-coupled device
CMOS: complementary metal-oxide semiconductor
FCS: fluorescence correlation spectroscopy
FWHM: full-width at half-maximum
iCCD: intensified charge-coupled device
ICS: image correlation spectroscopy
IL: interference lithography
NA: numerical aperture
NSOM or **SNOM**: near-field scanning optical microscopy
PID: proportiona, integrative and derivative
PSF: point-spread function
PZT: piezo-electric transducer
ROI: region of interest
SIL: solid immersion lens
SIM: structured illumination microscopy
SPCE: surface plasmon coupled emission
S-pol, P-pol: S-polarization, P-polarization
SPR: surface plasmon resonance
SPRF: surface plasmon resonance fluorescence
SSIM: saturated structured illumination microscopy
STED: stimulated emission depletion
STM: scanning tunneling microscopy
SW: standing wave
SW-SPRD: standing wave surface plasmon resonance fluorescence with linear deconvolution
SW-SPRF: standing wave surface plasmon resonance fluorescence
SW-TIRD: standing wave total internal reflection fluorescence with linear deconvolution
SW-TIRF: standing wave total internal reflection fluorescence
SW-TIRL: standing wave total internal reflection lithography
SW-TIRS: standing wave total internal reflection scattering
TIR: total internal reflection
TIRF: total internal reflection fluorescence

1. Introduction

1.1 Background and motivation

1.1.1 Microscopic image formation

In modern biological research, **optical microscopy** has provided a tool to observe the fine structures of samples under investigation. Optical microscopy even allows *in vivo* studies revealing the spatiotemporal nature of these living specimens. In particular, **fluorescence microscopy** provides molecular specificity by only visualizing biomolecules to which fluorescent dyes can be selectively bound under dark background. The widespread use of fluorescence microscopy has been accompanied by the rapid development of fluorescent labels and the advances in digital imaging that make quantitative analysis easier (Lichtman and Conchello, 2005). Unless otherwise specified, our discussion will be limited to the fluorescence microscopy in the following sections.

Far-field microscopic imaging is about measuring light distribution at the image space emitted from sample after passing through an optical imaging system. When a point object, substantially smaller than the wavelength of light, is imaged by a microscope, its image is significantly broader than its original size. The image of this effective point object is defined as the **point spread function** (PSF). PSF provides a measure of an optical system and has an important role in the image formation of a microscope. Likewise, PSF provides a measure of image resolution. The resolution depends on the **wavelength of light** and **numerical aperture** (NA) which is a number describing the amount of light that the objective lens can collect from a point source.

In fluorescence microscopy, an **image formation** can be described as the incoherent addition of the individual intensity images of fluorescent molecules in the sample. In other words, images of each fluorescent molecule can simply be added to form a final

image and this process can be described mathematically as a **convolution** of the fluorophore concentration distribution in the sample with the PSF of the optical system.

1.1.2 Limits of conventional microscopic resolution

The quest to image structural and functional biological information using far-field microscopy at high resolution has been hindered by both the wave nature and particle nature of light.

The **wave nature of light** in far-field microscopy leads to the Fraunhofer diffraction. Ernst Abbe (1873) first defined how the diffraction of light determines the image resolution and this depends on the wavelength and the NA of an objective lens used. The resolution of a fluorescence microscope can be defined as the minimal distance of two point objects which can be barely resolved in incoherent imaging. Commonly accepted **Rayleigh criterion** of resolution is satisfied when the central maximum of the PSF of one imaged point object falls within the first minimum of the other which is approximately equal to the full-width at half-maximum (FWHM) of the PSF (Goodman, 1996).

The **particle nature of light** poses a fundamental limit in the quantification of the detected signal due to quantum mechanical nature. Light can be considered as individual particles or photons. Even in perfect imaging condition and in absence of any other noise sources except the light signal itself, the measured signal fluctuates due to photon shot noise. The origin of the photon shot noise lies in the Poisson statistics of photons arriving at the detector that limits the accuracy of estimating the intensity of a source. This issue is practically important especially the inherently low light level imaging with fluorescence microscopes (Yariv, 1991).

Practically obtainable optical resolution is approximately half of the light wavelength used with oil immersion objectives based on the Abbe theory. A major limitation of optical imaging is that it cannot resolve objects with separation below several hundred

nanometers. Image resolution further degrades from this limit when the light level is low and photon shot noise starts to dominate. Improving spatial resolution beyond the diffraction limit is crucial for distinguishing fine details of samples in many life science applications and is the main subject of this thesis.

1.1.3 Review of super-resolution microscopy

Today **electron microscopy** can image biomedical specimens on the nanometer scale by utilizing the short wavelength of the electron matter wave. Though electron microscopy is a powerful high-resolution imaging tool, it suffers from being restricted to fixed specimen and the study of dynamic processes in a living biological sample is difficult (Koster and Klumperman, 2003). Further, the wide array of spectrally distinct fluorescent probes allows more specific biological information to be obtained in light microscopy. The other approach to enhance resolution is to use **scanning probe microscopes** such as scanning tunneling microscopy (STM), atomic force microscopy (AFM) and near-field scanning optical microscopy (NSOM or SNOM) (Betzig et al., 1991; Binnig et al., 1986; Binnig and Rohrer, 1986). While these techniques can achieve atomic resolution in solid-state samples, there is significant resolution degradation in soft biological specimens allowing resolution in the range of 50 – 100 nm (Betzig and Trautman, 1992). Furthermore, these scanning probe methods suffer from slow scanning speed on the order of minute per typical image and are limited to image upper surface of samples.

Given these limitations, there is a need to develop a completely optical imaging method with better than 100 nm resolution by utilizing its non-destructiveness, low cost, easy of use fluorescent labels with molecular specificity. The challenge of achieving **super-resolution in optical microscopy** beyond the diffraction limit has only been overcome in practice during the last couple of decades. In particular, extending lateral or transverse resolution has been exemplified with several techniques such as **stimulated emission depletion** (STED) microscopy, **saturated structured illumination microscopy**

(SSIM),**solid immersion lens** (SIL) microscopy, and **structured illumination microscopy** (SIM).

STED has achieved the highest far-field optical resolution reaching tens of nanometers using nonlinear photon-induced saturation depletion of the excited state in the outer regions of the excitation PSF. However, this technique suffers from relatively slow speed due to the point scanning nature (Hell and Wichmann, 1994; Westphal and Hell, 2005; Westphal et al., 2003). Furthermore, the need for efficient stimulated emission without causing saturation severely limits the number of suitable fluorophores. SSIM is almost an inverse version of STED using wide-field mode providing comparable super-resolution to STED. However, photobleaching in SSIM is a challenge in practice for biological specimens due to photodamage (Gustafsson, 2005). SIL microscopy takes advantage of high refractive index material replacing immersion oil, utilizing the evanescence field of SIL for near-field imaging, which also requires scanning (Mansfield and Kino, 1990). In contrast to these scanning methods except SSIM, the idea of SIM using wide-field detection has been proposed and has been implemented in different formats (Frohn et al., 2000; Gustafsson, 2000). This wide field detection allows faster data acquisition by encoding either diffraction grating illumination or standing wave illumination. This carries high frequency patterned illumination onto specimen providing up to a factor of 2 lateral resolution enhancements (Fedosseev et al., 2005; Frohn et al., 2000; Gustafsson, 2000). To decode the high frequency information, several images need to be taken with proper phase shift and general lateral resolution enhancement requires multiple rotations of this pattern.

1.1.4 Review of total internal reflection fluorescence microscopy

Total internal reflection fluorescence (TIRF) microscopy recently has emerged as the method of choice to probe cellular processes near the basal plasma membrane of adherent cells due to its unique capability of illuminating a very thin region on the order of 100 nm (Axelrod, 1981, 2001). The evanescent wave intensity decays exponentially from the

interface and this near-field excitation volume allows intrinsic optical sectioning to less than one-fifth of the excitation wavelength. The selective excitation of TIRF removes the out-of-focus noise, reduces photobleaching of fluorophores outside the focal plan, and is thus ideal for single molecule imaging (Tokunaga et al., 1997; Webb et al., 2006). On the other hand, TIRF doesn't allow deeper imaging into the interior of cells and the lateral resolution of TIRF remains the same as standard wide-field imaging.

1.1.5 Standing wave total internal reflection fluorescence microscopy

Even higher lateral resolution in wide-field mode can be achieved by combination of standing wave illumination and TIRF microscopy (Cragg and So, 2000; So et al., 2001). The **standing wave total internal reflection fluorescence** (SW-TIRF) microscopy is based on the generation of evanescent standing wave in TIRF geometry. In TIRF microscopy, evanescent waves are formed at the interface between the bottom surface of the specimen and its high refractive index substrate. Structured illumination can be formed by interfering two counter-propagating evanescence waves. In this approach, the excitation standing evanescent wave has an **effective wavelength** shorter than the free space excitation light by a factor of approximately $2n$ where n is the index refraction of the high refractive index substrate. The factor of 2 comes from the standing wave nature of the evanescent wave. The factor of n results from the fact that the evanescent wave has wavelength equal to that of the light in the high index medium which is equal to λ/n . In other words, the enhanced lateral resolution is possible since evanescent standing waves keep the standing wave spacing narrower than non-evanescent mode due to additional higher refractive index of a substrate. Since the standing wave modulation is inherently sinusoidal, to reconstruct the high resolution in the direction of the standing wave, a minimum of three images scan at different phase of the standing wave is required. The phase shift is in principle fast, and thus SW-TIRF doesn't necessarily increase the total image acquisition time compared to conventional wide-field imaging.

The lateral resolution of SW-TIRF mostly depends on the evanescent standing wave fringe period rather than the emission wavelength, which is proportional to the excitation wavelength in the substrate. As is the same with other high-resolution technique based on interference, there exists side-band artifact (Hell and Stelzer, 1992). This artifact can be easily removed by linear deconvolution provided that the emission PSF is narrow enough to keep the side-band lower than 30% during post image processing (Hanninen et al., 1995). Thus SW-TIRF technique effectively enhances the resolution even more than those of typical SIM methods.

1.2 Objectives

This dissertation describes the development of apparatus and methods to provide **wide-field super-resolution imaging technique** by the use of standing evanescent waves. In particular, SW-TIRF microscopy demonstrates the first time resolution enhancement of more than twice than that of traditional wide-field microscopy achieving lateral resolution of less than one fifth of the emission wavelength.

Several aims will be pursued in this thesis. First, the general formulation of the one-dimensional and two-dimensional SW-TIRF will be derived including different polarization modes analytically and numerically. Second, the implementation and the characterization of SW-TIRF microscopy apparatus will be discussed with experimental design and standing wave phase control. Third, we will demonstrate the first proof of principle of extended resolution with SW-TIRF and measurements with biological specimen. Finally, new contrast mechanisms using the standing wave total internal reflection will be explored based on surface plasmon resonance effect on the fluorescence emission.

Axelrod, D. (1981). Cell-Substrate Contacts Illuminated By Total Internal-Reflection Fluorescence. J Cell Biol *89*, 141-145.

Axelrod, D. (2001). Total internal reflection fluorescence microscopy in cell biology. Traffic *2*, 764-774.

Betzig, E., and Trautman, J.K. (1992). Near-Field Optics - Microscopy, Spectroscopy, and Surface Modification Beyond the Diffraction Limit. Science *257*, 189-195.

Betzig, E., Trautman, J.K., Harris, T.D., Weiner, J.S., and Kostelak, R.L. (1991). Breaking the Diffraction Barrier - Optical Microscopy on a Nanometric Scale. Science *251*, 1468-1470.

Binnig, G., Quate, C.F., and Gerber, C. (1986). Atomic Force Microscope. Phys Rev Lett *56*, 930-933.

Binnig, G., and Rohrer, H. (1986). Scanning Tunneling Microscopy. IBM J Res Dev *30*, 355-369.

Cragg, G.E., and So, P.T.C. (2000). Lateral resolution enhancement with standing evanescent waves. Opt Lett *25*, 46-48.

Fedosseev, R., Belyaev, Y., Frohn, J., and Stemmer, A. (2005). Structured light illumination for extended resolution in fluorescence microscopy. Opt Lasers Eng *43*, 403-414.

Frohn, J.T., Knapp, H.F., and Stemmer, A. (2000). True optical resolution beyond the Rayleigh limit achieved by standing wave illumination. Proc Natl Acad Sci U S A *97*, 7232-7236.

Goodman, J.W. (1996). Introduction to Fourier optics, 2nd edn (New York, McGraw-Hill).

Gustafsson, M.G.L. (2000). Surpassing the lateral resolution limit by a factor of two using structured illumination microscopy. J Microsc-Oxf *198*, 82-87.

Gustafsson, M.G.L. (2005). Nonlinear structured-illumination microscopy: Wide-field fluorescence imaging with theoretically unlimited resolution. Proc Natl Acad Sci U S A *102*, 13081-13086.

Hanninen, P.E., Hell, S.W., Salo, J., Soini, E., and Cremer, C. (1995). 2-Photon Excitation 4pi Confocal Microscope - Enhanced Axial Resolution Microscope For Biological-Research. Appl Phys Lett *66*, 1698-1700.

Hell, S., and Stelzer, E.H.K. (1992). Fundamental Improvement Of Resolution With A 4pi-Confocal Fluorescence Microscope Using 2-Photon Excitation. Opt Commun *93*, 277-282.

Hell, S.W., and Wichmann, J. (1994). Breaking The Diffraction Resolution Limit By Stimulated-Emission - Stimulated-Emission-Depletion Fluorescence Microscopy. Opt Lett *19*, 780-782.

Koster, A.J., and Klumperman, J. (2003). Electron microscopy in cell biology: integrating structure and function. Nat Cell Biol, SS6-SS10.

Lichtman, J.W., and Conchello, J.A. (2005). Fluorescence microscopy. Nature Methods *2*, 910-919.

Mansfield, S.M., and Kino, G.S. (1990). Solid Immersion Microscope. Appl Phys Lett *57*, 2615-2616.

So, P.T.C., Kwon, H.S., and Dong, C.Y. (2001). Resolution enhancement in standing-wave total internal reflection microscopy: a point-spread-function engineering approach. J Opt Soc Am A-Opt Image Sci Vis *18*, 2833-2845.

Tokunaga, M., Kitamura, K., Saito, K., Iwane, A.H., and Yanagida, T. (1997). Single molecule imaging of fluorophores and enzymatic reactions achieved by objective-type total internal reflection fluorescence microscopy. Biochem Biophys Res Commun *235*, 47-53.

Webb, S.E.D., Needham, S.R., Roberts, S.K., and Martin-Fernandez, M.L. (2006). Multidimensional single-molecule imaging in live cells using total-internal-reflection fluorescence microscopy. Opt Lett *31*, 2157-2159.

Westphal, V., and Hell, S.W. (2005). Nanoscale resolution in the focal plane of an optical microscope. Phys Rev Lett *94*, 143903.

Westphal, V., Kastrup, L., and Hell, S.W. (2003). Lateral resolution of 28 nm (lambda/25) in far-field fluorescence microscopy. Appl Phys B-Lasers Opt *77*, 377-380.

Yariv, A. (1991). Optical electronics / Amnon Yariv (Philadelphia :, Saunders College Pub.).

2. Theory of Standing wave total internal reflection fluorescence (SW-TIRF) microscopy

2.1 Introduction

In this chapter, we will describe an algorithm that allows SW-TIRF in one-dimension using a **point-spread function** (PSF) engineering approach and two-dimension by averaging the effective PSF in each direction. Experimentally translatable excitation light containing super-diffraction-limited spatial frequency components enables us to build the algorithm resulting in lateral resolution enhancement. In addition, the nature of standing evanescent wave will be investigated with S-polarization and P-polarization incident plane waves.

2.2 Image formation in SW-TIRF microscopy

2.2.1 Derivation of SW-TIRF point spread function

The image formation process in fluorescence microscopy can be described mathematically. Let $O(\vec{r})$ be the distribution of fluorescent object at position $\vec{r}$. Let $E(\vec{r})$ be the intensity distribution of excitation light. If $P(\vec{r})$ is the emission point-spread function (PSF), the image intensity of a fluorescent microscopy can be expressed as the convolution of the emitted light from the object modulated by the excitation with the conventional PSF:

$$I(\vec{r}) = [O(\vec{r})E(\vec{r})] \otimes P(\vec{r}). \qquad (2\text{-}1)$$

The emission PSF based on the Fraunhofer approximation can be described as

$$P(\vec{r}) = \left[\frac{2J_1(2\pi NA|\vec{r}|/\lambda_{emi})}{2\pi NA|\vec{r}|/\lambda_{emi}} \right]^2, \qquad (2\text{-}2)$$

where J_1 is the first-order Bessel function. NA is the numerical aperture of the objective. This intensity distribution is referred to as the **Airy pattern** which is the Fraunhofer diffraction pattern of a circular aperture (Goodman, 1996).

If $E(\vec{r})$ is uniform, this representation corresponds to wide-field fluorescence microscopy imaging. Here, the excitation intensity $E(\vec{r})$ is assumed to have two properties. First, $E(\vec{r})$ is translatable or its placement on the object plane can be experimentally controlled. Second, $E(\vec{r})$ carries higher spatial frequency components than the PSF which is realizable by use of evanescent standing wave.

With the first assumption, equation (2-1) can be written more generally as

$$I(\vec{r};\vec{r}\,') = [O(\vec{r})E(\vec{r}-\vec{r}\,')] \otimes P(\vec{r}), \qquad (2\text{-}3)$$

where $\vec{r}\,'$ is a position vector on the object plane that measures the translation of the excitation light profile relative to an arbitrary origin.

Let us restrict our discussion to one-dimensional geometry for now. Replacing the position vectors $\vec{r}$ and $\vec{r}\,'$ to x and x' respectively, we can re-write the equation (2-3) as

$$I(x;x') = [O(x)E(x-x')] \otimes P(x). \qquad (2\text{-}4)$$

If we define a composite image $I'(x)$ as a weighted sum of images recorded at a set of translational shift vectors $\{x'\}$,

$$I'(x) = \sum_{\{x'\}} f(x,x')I(x;x'), \qquad (2\text{-}5)$$

where $f(x,x')$ is an arbitrary weighting function. $I(x;x')$ is an intermediate image. Expanding the convolution integral in equation (2-4) explicitly,

$$I(x;x') = \int_{-\infty}^{\infty} O(x")E(x"-x')P(x-x")dx", \tag{2-6}$$

and exchanging the order of the integral and the summation in equation (2-6), one obtains

$$I'(x) = \int_{-\infty}^{\infty} O(x")\left[\sum_{\{x'\}} f(x,x')E(x"-x')\right]P(x-x")dx". \tag{2-7}$$

If $\{x'\}$ and $f(x,x')$ satisfies the following equation:

$$\sum_{\{x'\}} f(x,x')E(x"-x') = E(x-x"), \tag{2-8}$$

the equation (2-7) can be expressed as

$$I'(x) = O(x) \otimes [E(x)P(x)]. \tag{2-9}$$

The resultant image $I'(x)$ is the convolution of the fluorophore concentration distribution in the object $O(x)$ with an **effective PSF**, $E(x)P(x)$, which is the multiplication of the conventional PSF $P(x)$ and the structured excitation intensity $E(x)$. This excitation, which carries the high spatial frequency component of structured illumination, has been transferred into the PSF to generate an effective PSF. From the second assumption about the excitation field, this effective PSF contains high spatial frequency components which originate from $E(x)$. As a result, the composite image can have higher resolution than the intermediate images if we properly find a set of shift vectors $\{x'\}$ and a weighting function $f(x,x')$ that satisfies the equation (2-8). The algorithm can be implemented based on Fourier decomposition of $f(x,x')$ and the derivation is detailed in the literature (So et al., 2001).

The excitation intensity profile from evanescent standing wave above the surface of a high refractive index substrate can be approximately described as

$$E(x) = 1 + \alpha \cdot \cos\left(4\pi n \sin\theta \cdot x / \lambda\right), \tag{2-10}$$

where α is the contrast of the standing wave, n is the refractive index of a substrate, θ is the incidence angle of the excitation beam at the interface, and λ is the vacuum excitation wavelength. This formulation gives lateral resolution enhancement in the direction of the standing wave. The extension of this one-dimensional (1D) SW-TIRF theory to uniform lateral resolution enhancement can be achieved by superimposing the finite number of rotational SW-TIRF images (Chung et al., 2006; Cragg and So, 2000).

We can extend the formulation of one-dimensional SW-TIRF theory to achieve uniform resolution enhancement laterally by making the effective PSF axially symmetric. If the direction of the standing evanescent wave excitation is rotated by an angle φ from x axis, each intermediate image in 2D can be written as

$$I'(\vec{r},\varphi) = O(\vec{r}) \otimes [E(\vec{r},\varphi) P(r)], \tag{2-11}$$

where the PSF of the imaging optics $P(r)$ is axially symmetric by nature. The enhanced final image will have no directional preference if intermediate images from different rotational angle φ are averaged:

$$\begin{aligned} I''(\vec{r}) &= \frac{1}{\pi}\int_0^{\pi} I'(\vec{r},\varphi)\,d\varphi = O(\vec{r}) \otimes \left[P(r) \cdot \frac{1}{\pi}\int_0^{\pi} E(\vec{r},\varphi)\,d\varphi \right] \\ &= O(\vec{r}) \otimes \left[P(r) \cdot E'(\vec{r}) \right]. \end{aligned} \tag{2-12}$$

Let the position vector be $\vec{r} = r\cos\theta\hat{i} + r\sin\theta\hat{j}$ and the wave vector of the excitation wave be $\vec{k} = k\cos\varphi\hat{i} + k\sin\varphi\hat{j}$. The constant phase location of the standing wave can be expressed as $\vec{r}\cdot\vec{k} = kr\cos(\theta-\varphi)$. This yields an effective excitation of

$$E'(\vec{r}) = \frac{1}{\pi}\int_0^{\pi} E(kr\cos(\varphi))d\varphi, \tag{2-13}$$

where θ is eliminated from rotational symmetry. In practice, we can use finite numbers of the general polar angle in N equi-angular directions between $[0,\pi]$ resulting in the excitation intensity as

$$E''(\vec{r}) = \frac{1}{N}\sum_{i=0}^{N-1} E'\left(kr\cos\frac{i\pi}{N}\right). \tag{2-14}$$

2.2.2 SW-TIRF image reconstruction

Since the standing wave modulation is inherently sinusoidal, to reconstruct the high resolution in the direction of the standing wave, a minimum three image obtained at different phase of the standing wave is required. To generate a 1D SW-TIRF image, three wide-field images are required to be taken while each phase of the interfering standing wave excitation is changed by 120° with the specimen remained stationary. The phase difference of 120° is chosen to provide the highest signal-to-noise ratio (So et al., 2001). The superposition of the appropriately weighted images gives a high-resolution image in the standing wave direction. A simplified pictorial algorithm is depicted in **Fig.** 2.1. The standing wave in vertical direction is exciting sub-diffraction-limit fluorescent beads. The phase of standing wave are set at 0, 120, and 240 degrees in each (a, a1), (b, b1) and (c, c1). (a-c) shows the intermediate images on the CCD camera and (a1-c1) is the processed image after being multiplied by corresponding weighting functions containing the underlined standing wave information. The summation of these (a1-c1)

images gives a 1D SW-TIRF image with enhanced resolution in the vertical direction. (d) shows the original TIRF image for comparison. This can also be obtained by the summation of (a-c). For two-dimensional SW-TIRF, finite N equi-polar angles are chosen and corresponding 1D SW-TIRF images are superposed to generate one final enhanced image. This requires the total number of 3N wide-field images. In this thesis, we used two-directional averaging for demonstration of 2D SW-TIRF.

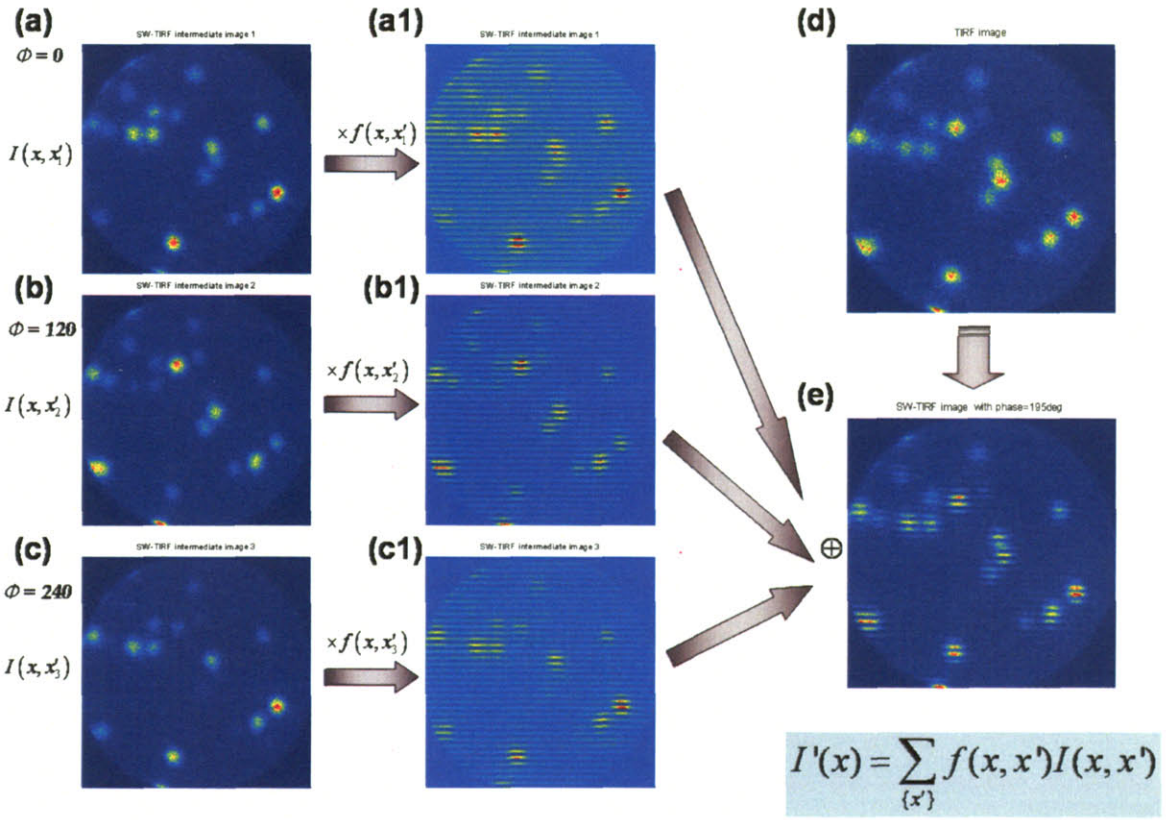

Fig. 2.1 The pictorial algorithm to generate a one-directional SW-TIRF image from three intermediate images with different standing evanescent wave phases. (a-c): intermediate images, (a1-c1): intermediate images multiplied by corresponding weighting functions, (d) original TIRF image, and (e) 1D SW-TIRF image.

2.2.3 Numerical simulation of SW-TIRF point spread function

As mentioned in 2.2.1, general lateral resolution enhancement can be obtained by superposition of the enhanced images in several directions. To determine how many directional images are required to get axially symmetric PSF in a practical sense, numerical simulation has been performed using a Matlab program (The MathWorks, Natick, MA) and the simulated effective PSF is described in **Fig.** 2.2.

For N number of directional scan, uniform angular separation was used and only the profiles of the thinnest PSF FWHM and the thickest PSF FWHM direction were presented since all the other directional profiles lies between these two. **Fig.** 2.2 (A) shows the shape of lateral PSFs with corresponding contour plots for N = 0, 1, 2, 3, 4 and 5. For N = 0, the PSF is the same as conventional TIRF or wide-field PSF. For N = 1, the thinnest PSF FWHM in the direction of standing wave propagation is achieved resulting in about 230% narrower PSF in the standing wave direction while the PSF FWHM in the perpendicular direction remains the same as the conventional TIRF (or N = 0 case). For N = 2, the difference of PSF FWHM in the thinnest and the thickest directions is less than 10%, and thus can be regarded as reasonably isotropic. Also it is noticeable that the two directional PSF profiles virtually converge as N increases.

Fig. 2.3 shows the shapes of lateral modulation transfer functions (MTFs) which are the absolute values of the Fourier transform of corresponding PSFs. As is notable in N = 1 case, the spatial frequency domain coverage is larger in the direction of thinnest direction compared to the thickest direction. This Fourier domain view provides complementary information to the space domain view. Though N = 3 or 4 would be better in terms of the isotropic shape of PSF, the two-directional SW-TIRF will be used for the experimental demonstration since using more directions will lengthen the total exposure time and compromise fast speed imaging. Future implementations of SW-TIRF will address this limitation.

In these simulations, the PSF FWHM of TIRF (without standing wave) is chosen to be 199 nm calculated using the nominal 1.45 numerical aperture of an Olympus objective. In the actual measurements, the measured PSF FWHM for the objective was about 260 nm which corresponds to that of NA 1.1 from numerical simulation using the ideal Airy pattern based on Fraunhofer diffraction theory. Similar results were observed in literatures (Frohn et al., 2000; Neil et al., 1997) and will be discussed in Chapter 4.

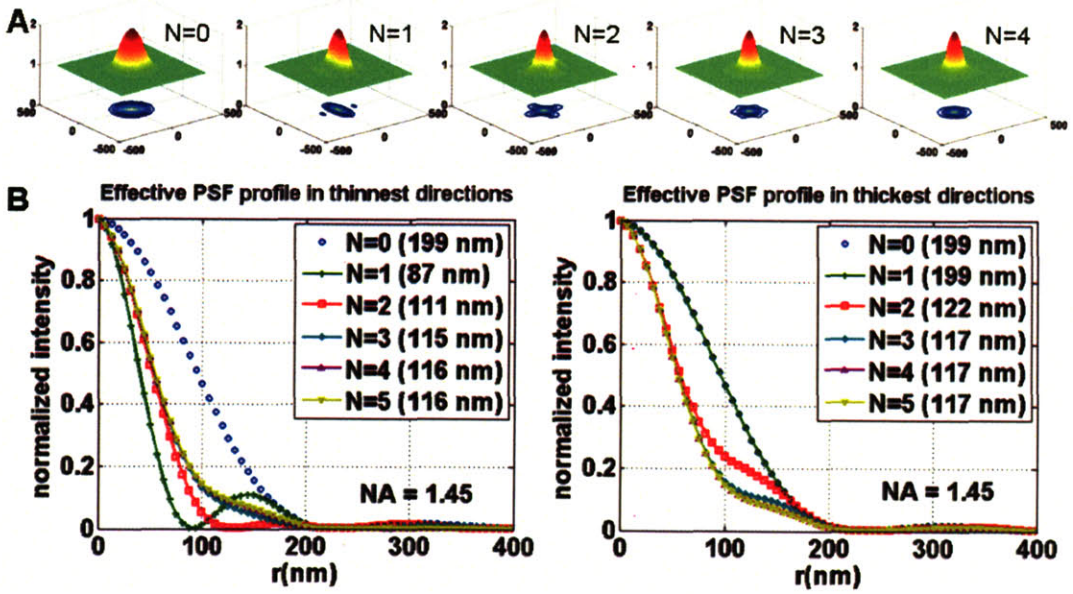

Fig. 2.2 (A) Effective PSF simulation of two-dimensional SW-TIRF for directions N = 0, 1, 2, 3, 4 and 5. N = 0 corresponds to the conventional TIRF. Anisotropy of PSF decreases as N increases. (N: number of scan directions), (B) Comparison of the PSF profile in the thinnest and the thickest direction. All other cross sectional profiles lie between these two profiles for corresponding N. Simulation condition: numerical aperture (NA) = 1.45, $\alpha = 1.0$, $\lambda_{exc} = 532$ nm, $\lambda_{emi} = 560$ nm, $n = 1.52$, $\theta_{incidence} = 67^\circ$ (or fringe period = 190nm).

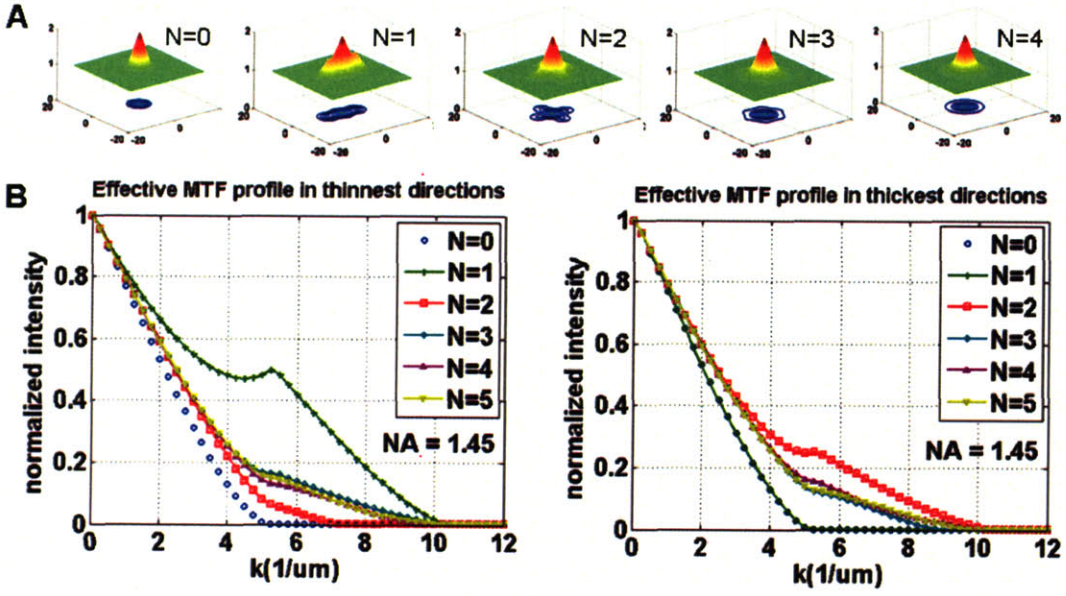

Fig. 2.3 (A) Effective MTF simulation of two-dimensional SW-TIRF for directions N = 0, 1, 2, 3, 4 and 5. N = 0 corresponds to the conventional TIRF. Anisotropy of MTF decreases as N increases, (B) Comparison of the MTF profile in the thinnest and the thickest direction of PSFs. The same simulation condition as in **Fig.** 2.2.

2.3 Polarization effect on standing wave excitation

In the previous sections, the nature of **standing wave** (SW) excitation was described in detail. When two plane waves meet forming a standing wave, there are basically two configurations of interest. One is **P-polarization** (P-pol) when the electric vector is in the plane of incidence which is formed by the incidence and reflected rays, and the other is **S-polarization** (S-pol) when the electric vector is perpendicular to the plane of incidence. In this section, the mathematical expression of standing wave excitations for S-pol and P-pol is derived in non-TIR and TIR geometry. Though most of the SW-TIRF experiments were performed under S-pol conditions, P-pol is of particular interest when the surface plasmon resonance effect is considered. Since we are also developing standing-wave surface plasmon resonance fluorescence (SW-SPRF) microscopy based on a similar principle to the one in SW-TIRF, the mathematical description can help understand and implement SW-SPRF microscopy, to be introduced in Chapter 5.

2.3.1 Polarization effect on standing wave excitation

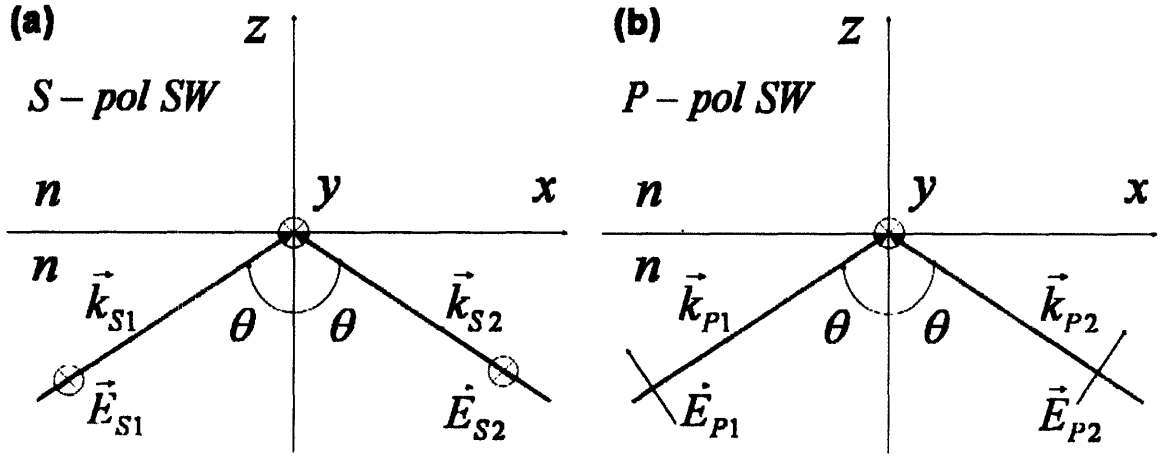

Fig. 2.4 Schematic illustration of the standing wave excitation from two electromagnetic plane waves with oblique incidence angle: (a) S-polarization and (b) P- polarization (the plane wave fronts are not illustrated in the diagram.).

Consider two plane waves crossing at equal incidence angles θ from opposite sides. Only the case of either S-pol or P-pol is considered. The geometry is depicted in **Fig.** 2.4 for further mathematical derivation.

In S-pol geometry, the two plane waves in **Fig.** 2.4 (a) can be described as

$$\vec{E}_{S1}(x,z) = \hat{y}E_0 \exp(k\sin\theta\cdot x + k\cos\theta\cdot z + \phi_1)$$
$$\vec{E}_{S2}(x,z) = \hat{y}E_0 \exp(-k\sin\theta\cdot x + k\cos\theta\cdot z + \phi_2), \qquad (2.15)$$

where E_0 is the amplitude of each incident plane wave and assumed to be the same in both. The wave vector is $k = 2\pi n/\lambda_0$ where n is the refractive index of the media, θ is the incidence angle and λ_0 is the wavelength of the excitation light. The phase of each wave is ϕ_1 and ϕ_2. Since the temporal dependence is irrelevant in terms of average intensity, it is neglected here. The average intensity for S-pol SW can be calculated as

$$\left|\vec{E}_{S1} + \vec{E}_{S2}\right|^2 = 2E_0{}^2\left[1 + 1\cdot\cos(2k\sin\theta\cdot x + \Delta\phi)\right], \qquad (2.16)$$

where $\Delta\phi = \phi_1 - \phi_2$. Interestingly, the final standing wave intensity distribution doesn't depend on the z axis and the combined phase is the difference between the incoming waves. In addition, the contrast of the standing wave is always 100%.

In P-pol geometry, the two plane waves in **Fig.** 2.4 (a) can be described as

$$\vec{E}_{P1}(x,z) = \hat{x}E_0\cos\theta\cdot\exp(k\sin\theta\cdot x + k\cos\theta\cdot z + \phi_1) + \hat{z}E_0\sin\theta\cdot\exp(-k\sin\theta\cdot x + k\cos\theta\cdot z + \phi_1) \quad \text{and}$$

$$\vec{E}_{P2}(x,z) = \hat{x}E_0\cos\theta\cdot\exp(-k\sin\theta\cdot x + k\cos\theta\cdot z + \phi_2) - \hat{z}E_0\sin\theta\cdot\exp(k\sin\theta\cdot x + k\cos\theta\cdot z + \phi_2). \qquad (2.17)$$

The average intensity distribution for P-pol SW is

$$\left|\vec{E}_{P1}+\vec{E}_{P2}\right|^2 = 2E_0{}^2\left[1+\cos 2\theta\cdot\cos\left(2k\sin\theta\cdot x+\Delta\phi\right)\right]. \tag{2.18}$$

This result is very similar to that of the S-pol case except that the contrast is not 100% but dependent on the incidence angle. Only when the incidence angle is near zero or near 90° does the contrast go to unity. On the contrary, the contrast vanishes when the incidence angle is 45°, the case when the polarizations of two beams are perpendicular.

2.3.2 Polarization effect on evanescent standing wave excitation

In this section, the electric field in the TIR geometry is investigated. From the boundary conditions of Maxwell's equation, the Snell's law holds as below for the propagating light waves between a medium 1 and 2:

$$n_1\sin\theta_1 = n_2\sin\theta_2, \tag{2.19}$$

where n_1 is the refractive index of medium 1 and n_2 is that of medium 2. θ_1 and θ_2 are the incidence and the refracted angle from the z axis. Let's consider the case of $n_1 > n_2$. Then, there exists the *critical angle* of $\theta_{cr} = \sin^{-1}\left(n_2/n_1\right)$. Even when the incidence angle is larger than the critical angle ($\theta_1 > \theta_{cr}$), the Snell's law holds and the angle of refraction can be written as

$$\sin\theta_2 = \left(\frac{n_1}{n_2}\right)\sin\theta_1 \triangleq \frac{1}{\beta}\sin\theta$$

$$\cos\theta_2 = i\sqrt{\left(\frac{n_1}{n_2}\right)^2\sin^2\theta_1 - 1} \triangleq \frac{i}{\beta}\sqrt{\sin^2\theta-\beta^2}, \tag{2.20}$$

where the refractive angle θ_2 can be expressed with the incidence angle θ and the refractive index ratio $\beta \triangleq n_2/n_1 = \sin\theta_{cr}$ (Born et al., 1999).

The electric field amplitude of the refracted light can be described by the *Fresnel equations*. The *amplitude transmission coefficients* for S-pol and P-pol are

$$T_{S2} = \frac{2n_1\cos\theta_1}{n_1\cos\theta_1 + n_2\cos\theta_2} E_{S1}$$
$$T_{P2} = \frac{2n_1\cos\theta_1}{n_1\cos\theta_2 + n_2\cos\theta_1} E_{P1}. \tag{2.21}$$

With super-critical incidence angle i.e. $\sin\theta > \beta$, the above equation can be expressed with the incidence angle and the refractive index ratio:

$$T_{S2} = \frac{2\cos\theta}{\cos\theta + i\sqrt{\sin^2\theta - \beta^2}} E_{S1}$$
$$T_{P2} = \frac{2\beta\cos\theta}{\beta^2\cos\theta + i\sqrt{\sin^2\theta - \beta^2}} E_{P1}. \tag{2.22}$$

From now on, the electric field amplitude of the incident light will be assumed to be unity for simplicity.

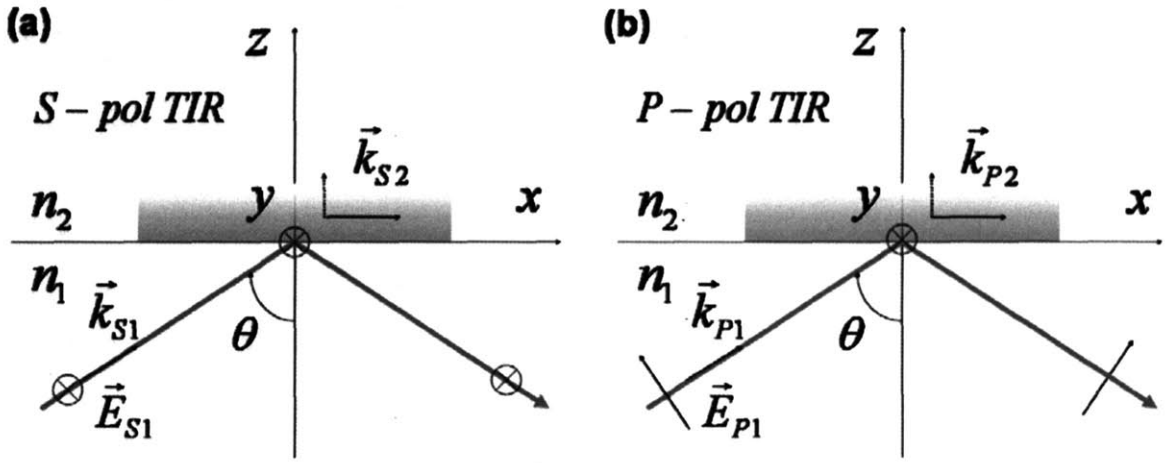

Fig. 2.5 Schematic illustration of the electromagnetic wave totally-internally-reflecting at an interface with supercritical incidence angle: (a) S-polarization and (b) P- polarization

Assuming the entering beam is infinitely wide or a plane wave, the intensity of the evanescent wave in the lower refractive index medium exponentially decays with perpendicular distance z from the interface as

$$I(z) = I(0)\exp\left(-z/\delta\right), \tag{2.23}$$

where the **penetration depth** is defined with the vacuum wavelength λ_0 :

$$\delta = \frac{\lambda_0}{4\pi n_1 \sqrt{\sin^2\theta - \beta^2}}. \tag{2.24}$$

This penetration depth is usually less than 100 nm and thus allows a very shallow excitation optical slice with low background in TIRF microscopy. The above relation holds for both S-pol and P-pol cases, and the geometry is illustrated in **Fig.** 2.5.

For S-pol incident light, the evanescent electric field vector direction remains purely normal to the plane of incidence:

$$\vec{E}_{S2}(\vec{r};\theta) = \hat{y}\, t_s(\theta)\exp(ik_1 \sin\theta \cdot x)\exp\left(-z/2\delta\right), \tag{2.25}$$

where

$$t_s(\theta) = \frac{2\cos\theta}{\sqrt{1-\beta^2}}\exp(-i\varphi_S), \tag{2.26}$$

$$\varphi_S = \tan^{-1}\left(\frac{\sqrt{\sin^2\theta-\beta^2}}{\cos\theta}\right), \tag{2.27}$$

and the wave vector is $k_1 = 2\pi n_1/\lambda_0$. Here the temporal dependence is neglected since it doesn't affect the final average intensity distribution.

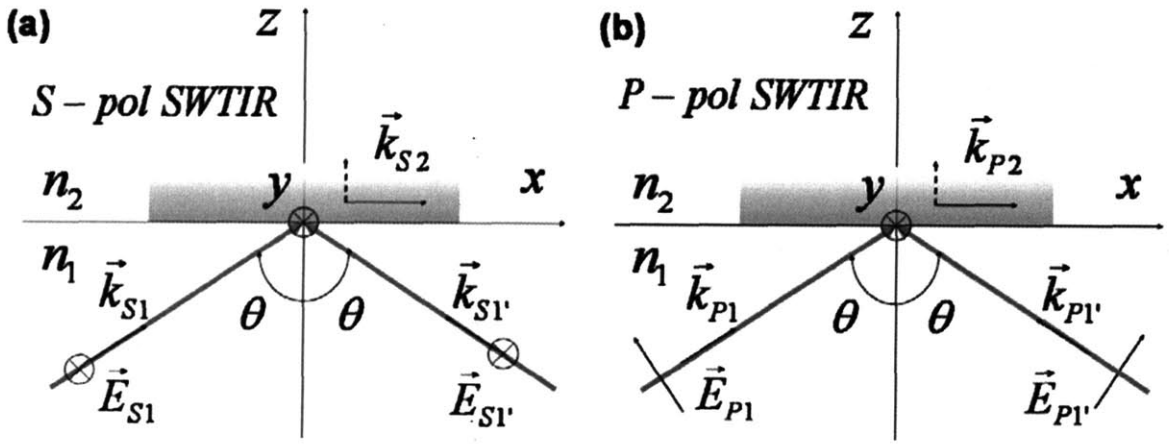

Fig. 2.6 Schematic illustration of the standing evanescent wave excitation from two electromagnetic plane waves with supercritical incidence angle: (a) S-polarization and (b) P- polarization

The standing evanescent wave with S-pol, described in **Fig.** 2.6 (a), can be written as follows:

$$\begin{aligned}\vec{E}_{S2,SW-TIR} &= \vec{E}_{S2}(\vec{r};\theta)+\vec{E}_{S2}(\vec{r};-\theta)\\ &= \hat{y}\,t_s(\theta)\exp\left(-z/2\delta\right)\left[\exp(ik_1\sin\theta\cdot x)+\exp(-ik_1\sin\theta\cdot x)\right].\\ &= 2\hat{y}\,t_s(\theta)\exp\left(-z/2\delta\right)\cos(k_1\sin\theta\cdot x)\end{aligned} \tag{2.28}$$

The intensity distribution is

$$\begin{aligned}I_{S2,SW-TIR} &= \left|\vec{E}_{S2,SW-TIR}\right|^2\\ &= 2\left|t_s(\theta)\right|^2\exp\left(-z/\delta\right)\left[1+1\cdot\cos(2k_1\sin\theta\cdot x)\right]\end{aligned}. \tag{2.29}$$

It is notable that the resultant interference fringe has always the contrast of 100% from S-pol SW-TIR case. In addition, the fringe spacing does not depend on the lower refractive index as long as the TIR condition holds.

For P-pol incident light, the evanescent electric field vector direction remains to be in the plane of incidence:

$$\vec{E}_{P2}(\vec{r};\theta) = t_P(\theta)\exp(ik_1\sin\theta\cdot x)\exp\left(-z/2\delta\right)\left[-i\hat{x}\sqrt{\sin^2\theta-\beta^2}+\hat{z}\sin\theta\right], \tag{2.30}$$

where

$$t_P(\theta) = \frac{2\cos\theta}{\sqrt{\beta^4\cos^2\theta+\sin^2\theta-\beta^2}}\exp(-i\varphi_P) \tag{2.31}$$

$$\varphi_S = \tan^{-1}\left(\frac{\sqrt{\sin^2\theta-\beta^2}}{\beta^2\cos\theta}\right). \tag{2.32}$$

Interestingly, the evanescent electric field vector is rotating in the plane of incidence with nonzero longitudinal components (Axelrod, 2003). Since the x and z component are different in the evanescent field, the electric field is elliptically polarized and 'cartwheel' along the x direction. The ratio of z-component to x- component is usually greater than unity and the z-component dominates if the incidence angle goes close to the critical angle.

The standing evanescent wave with P-pol, described in **Fig.** 2.6(b), can be written as follows:

$$\begin{aligned}\vec{E}_{P2,SW-TIR} &= \vec{E}_{P2}(\vec{r};\theta)+\vec{E}_{P2}(\vec{r};-\theta)\\ &= 2\,t_P(\theta)\exp\left(-z/2\delta\right)\left[i\hat{x}\sin\theta\sin\left(k_1\sin\theta\cdot x\right)+i\hat{z}\sqrt{\sin^2\theta-\beta^2}\cos\left(k_1\sin\theta\cdot x\right)\right]\end{aligned} \tag{2.33}$$

The corresponding intensity distribution is

$$\begin{aligned}I_{P2,SW-TIR} &= \left|\vec{E}_{P2,SW-TIR}\right|^2\\ &= 2\left|t_P(\theta)\right|^2\exp\left(-z/\delta\right)\left(2\sin^2\theta-\beta^2\right)\left[1-\left(\frac{\beta^2}{2\sin^2\theta-\beta^2}\right)\cdot\cos\left(2k_1\sin\theta\cdot x\right)\right]\end{aligned} \tag{2.34}$$

In comparison with the case of S-pol, the intensity distribution in P-pol forms similar standing wave in x-direction except the contrast of $\beta^2/\left(2\sin^2\theta-\beta^2\right)$ which varies with the incidence angle and the refractive index ratio.

To understand this contrast, it was simulated with several refractive indices and incidence angles in **Fig.** 2.7. The medium 2 was chosen among air (n = 1.0), water (n = 1.33), and cellular cytoplasm (n ~ 1.38). The medium 1 was chosen as typical coverslip glass (n = 1.515) for NA 1.45 objective and high refractive index coverslip glass (n = 1.78) for NA 1.65 objective.

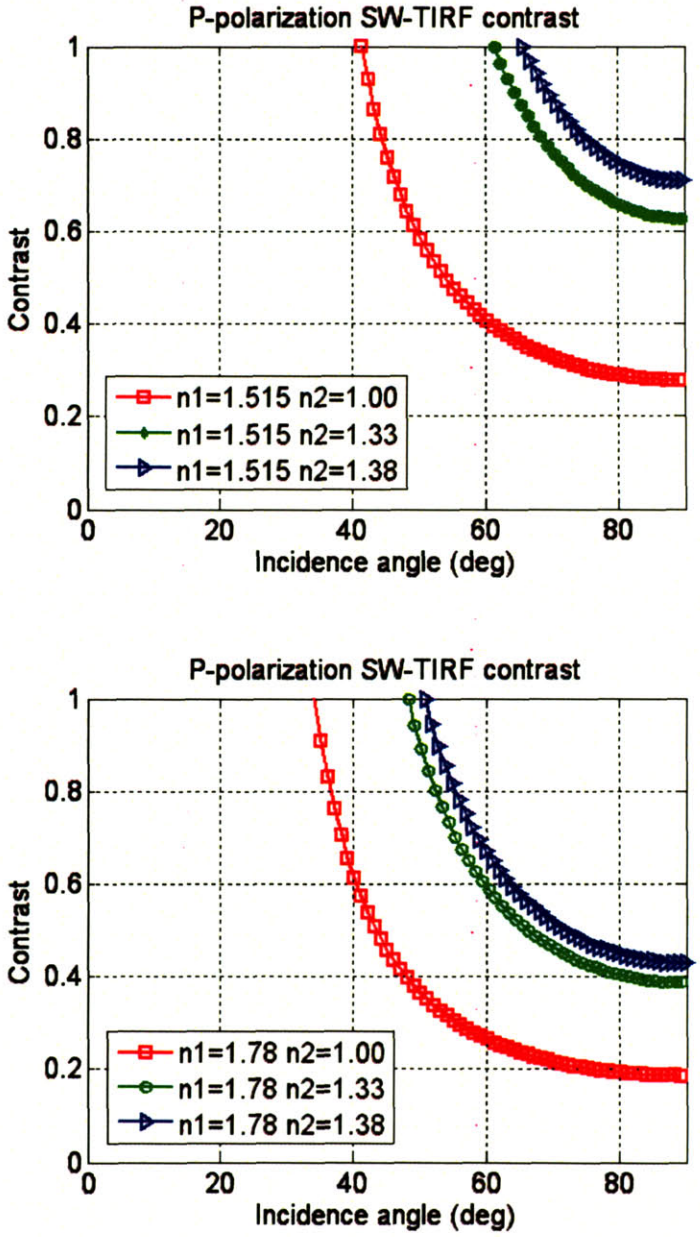

Fig. 2.7 The contrast of P-polarization evanescent standing waves: (Top) medium 1 as a typical BK7 coverslip glass (n = 1.515) and (Bottom) medium 1 as a high refractive index coverslip glass (n = 1.78). Three different medium 2 was calculated among air (n = 1.0), water (n = 1.33) and cellular cytoplasm (n ~ 1.38).

Since our system allows maximum incidence angle of 73° for NA 1.45 objective and 68° for NA 1.65 objective, respectively. NA 1.45 case is preferable to achieve contrast more than 75% while keeping high incidence angle to generate finer interference fringes.

The distribution of the evanescent field intensity for both S-pol and P-pol was simulated in **Fig.** 2.8. The exponential decaying nature of intensity distribution is common for both S-pol and P-pol as shown in **Fig.** 2.8 (c) and (d). While the contrast is constant of 100% for S-pol, it varies for P-pol as a function of the angle of incidence and refractive index ratio. The contrasts for S-pol and P-pol in the simulation were calculated as 1.0 and 0.77, respectively. This result suggests that P-pol SW-TIR is also feasible. However, this simulation is in contrary to one lithography literature and needs to be further confirmed experimentally (Ohdaira et al., 2006).

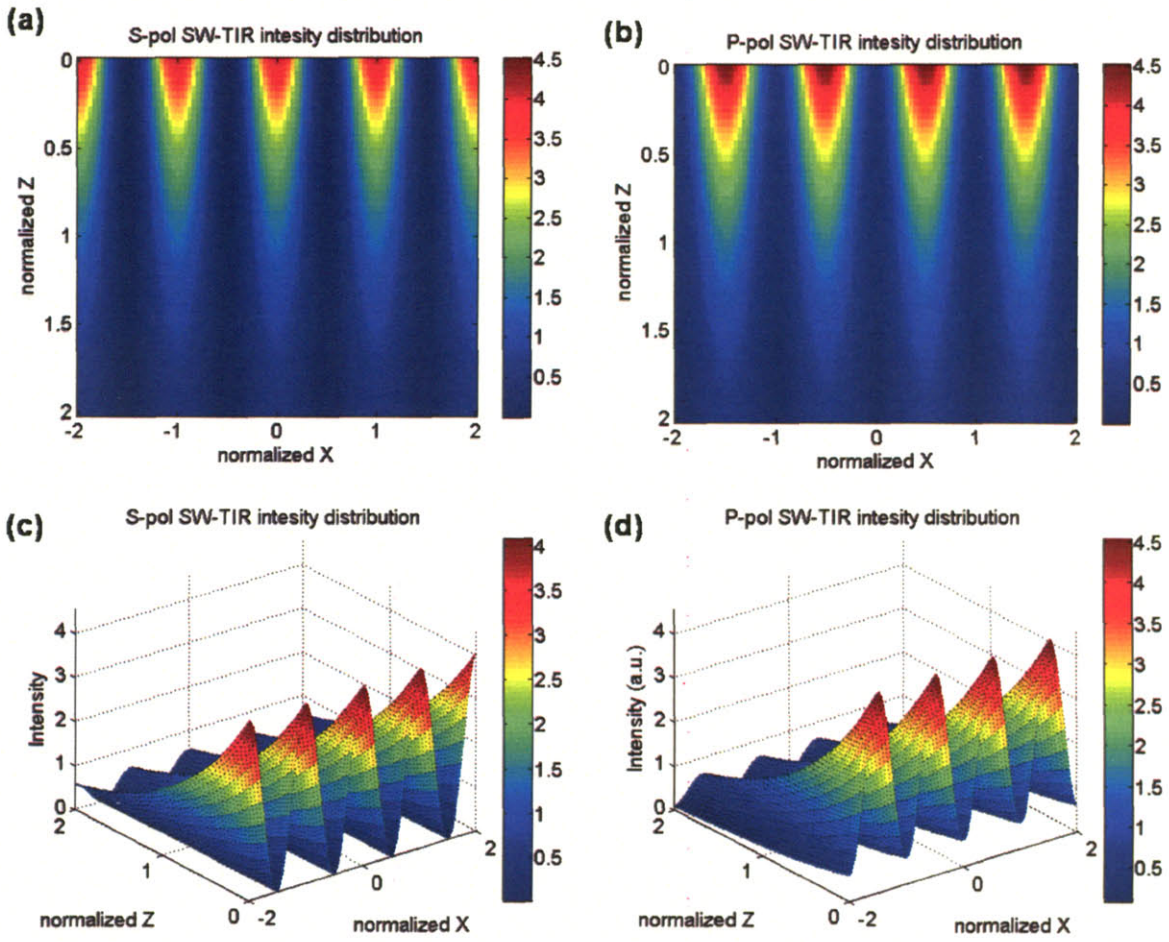

Fig. 2.8 SW-TIR intensity distribution for S-polarization (a, c) and P-polarization (b, d): x axis is normalized to one period of the evanescent standing wave ($\lambda_0 / 2\pi \sin\theta$) and z axis is normalized to the penetration depth. Simulation condition: λ_0 = 532 nm, θ = 73°, n_1 = 1.52 (standard glass) and n_2 = 1.33 (water).

2.4 Conclusions

In this chapter, the **general theory of SW-TIRF microscopy** is derived based on the PSF engineering approach. Originally one-dimensional SW-TIRF theory was extended to two-dimensional theory for general lateral resolution enhancement supported by numerical simulation. The modulations of sub-diffraction-limited fine standing wave fringes onto the specimen enabled the reconstruction of a high-resolution image by allowing the high spatial frequency information which bypasses the optical imaging system, which is basically a low pass filter. In addition, the general theoretical investigation of the polarization effect on the standing wave excitation revealed even P-polarized beams can form a standing wave with varying degree of contrast which can be utilized for some imaging mode using standing wave modulation.

In principle, the emission PSF plays a relatively minor role in setting the ultimate resolution limits. Instead, it is mostly limited by how small the structured excitation could be generated. If non-linear excitation is incorporated, even further resolution could be achieved. (Gustafsson, 2005), (So et al., 2001). Without incorporating any nonlinear optical technique, the PSF FWHM could have reached down to about 90nm with current setting. However, the Gaussian laser beam needs a little margin to generate uniform standing wave overlapping field on to the field of view. Further resolution of 69 nm could be achieved if currently available NA 1.65 objective with 457nm excitation is used.

Axelrod, D. (2003). Total internal reflection fluorescence microscopy in cell biology. In Biophotonics, Pt B (San Diego, Academic Press Inc), pp. 1-33.

Born, M., Wolf, E., and Bhatia, A.B. (1999). Principles of optics (Cambridge [England] ; New York :, Cambridge University Press).

Chung, E., Kim, D.K., and So, P.T.C. (2006). Extended resolution wide-field optical imaging: objective-launched standing-wave total internal reflection fluorescence microscopy. Opt Lett *31*, 945-947.

Frohn, J.T., Knapp, H.F., and Stemmer, A. (2000). True optical resolution beyond the Rayleigh limit achieved by standing wave illumination. Proc Natl Acad Sci U S A *97*, 7232-7236.

Goodman, J.W. (1996). Introduction to Fourier optics, 2nd edn (New York, McGraw-Hill).

Gustafsson, M.G.L. (2005). Nonlinear structured-illumination microscopy: Wide-field fluorescence imaging with theoretically unlimited resolution. Proc Natl Acad Sci U S A *102*, 13081-13086.

Neil, M.A.A., Juskaitis, R., and Wilson, T. (1997). Method of obtaining optical sectioning by using structured light in a conventional microscope. Optics Letters *22*, 1905-1907.

Ohdaira, Y., Noguchi, K., Shinbo, K., Kato, K., and Kaneko, F. (2006). Nano-fabrication of surface relief gratings on azo dye films utilizing interference of evanescent waves on prism. Colloids and Surfaces a-Physicochemical and Engineering Aspects *284*, 556-560.

So, P.T.C., Kwon, H.S., and Dong, C.Y. (2001). Resolution enhancement in standing-wave total internal reflection microscopy: a point-spread-function engineering approach. J Opt Soc Am A-Opt Image Sci Vis *18*, 2833-2845.

3. Instrument Development for Standing Wave Total Internal Reflection Fluorescence Microscopy

3.1 General considerations

To develop the SW-TIRF apparatus, one essential requirement is to generate a standing wave in **total internal reflection** (TIR) geometry. A standing wave can be generated with two counter-propagating beams or generated by an incident beam and its retro-reflection. In general, we found that standing waves generated by two counter-propagating beam with symmetric geometry is superior since the contrast can be degraded if the two interfering beams have different intensity and that happens in the non-symmetric configuration due to propagation loss of the excitation light. For TIR generation, the incident excitation beam should have a supercritical angle of incidence when it enters the interface of the high refractive index media, usually a coverslip, and low refractive index media, usually a sample containing medium. Basically, two difference geometries were of consideration and the schematic diagram is given in **Fig.**3.1.

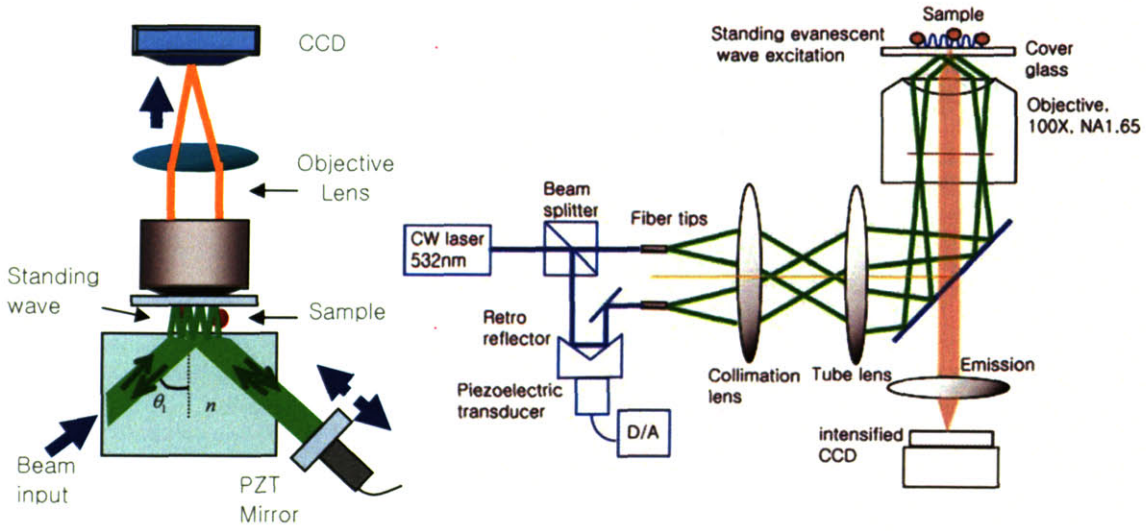

Fig. 3.1 Schematic diagrams of two different geometries for the SW-TIRF apparatus: (Left) the prism-launched SW-TIRF microscope, (Right) the objective-launched SW-TIRF microscope

One is a **prism-launched SW-TIRF** and the other is an **objective-launched SW-TIRF**. The former uses a laser beam entering from the side of a high refractive index prism. This setup can have a higher incidence angle and is relatively inexpensive to setup. However, the access to the sample is limited and the preparation of a biological specimen, such as a cultured cell medium, is not convenient. The objective-launched SW-TIRF has the advantage of completely open access to the sample which makes this setup preferable for biological sample imaging. In addition, this setup makes the conversion between conventional wide-field mode and SW-TIRF mode convenient by simply changing the displacement of the ends of the launching optical fiber. One drawback is the existence of stray light in the evanescent illumination. A small fraction of the illumination of the sample comes from excitation light scattered inside the objective lens. Another drawback of objective-launched system is the upper bound of the NA is limited to 1.65, the highest numerical aperture lens available to day. In contrast, prism with very high index material can be made with index reaching beyond 3 with some semiconductor material potentially allowing higher resolution. Originally, we built a prism-launched system but finally decided switching to an objective-launched system, mainly due to its merit in compatibility with biological preparation.

3.2 SW-TIRF optical setup

The objective-launched SW-TIRF optical setup is shown in **Fig.** 3.2 with the closed-loop standing wave phase control unit. The difference of this setup from the **Fig.** 3.1 (Right) is the addition of closed-loop feedback for SW phase control. The setup is basically using an inverted microscope: the evanescent SW wave excitation is generated using the side-port by focusing down two coherent beams at the back-focal-plane of a TIRF objective. The SW phase detection unit is setup to the opposite side of the microscope. The image detection is using the back port of the microscope with the additional relay optics to achieve enough final magnification which is not displayed in the figure.

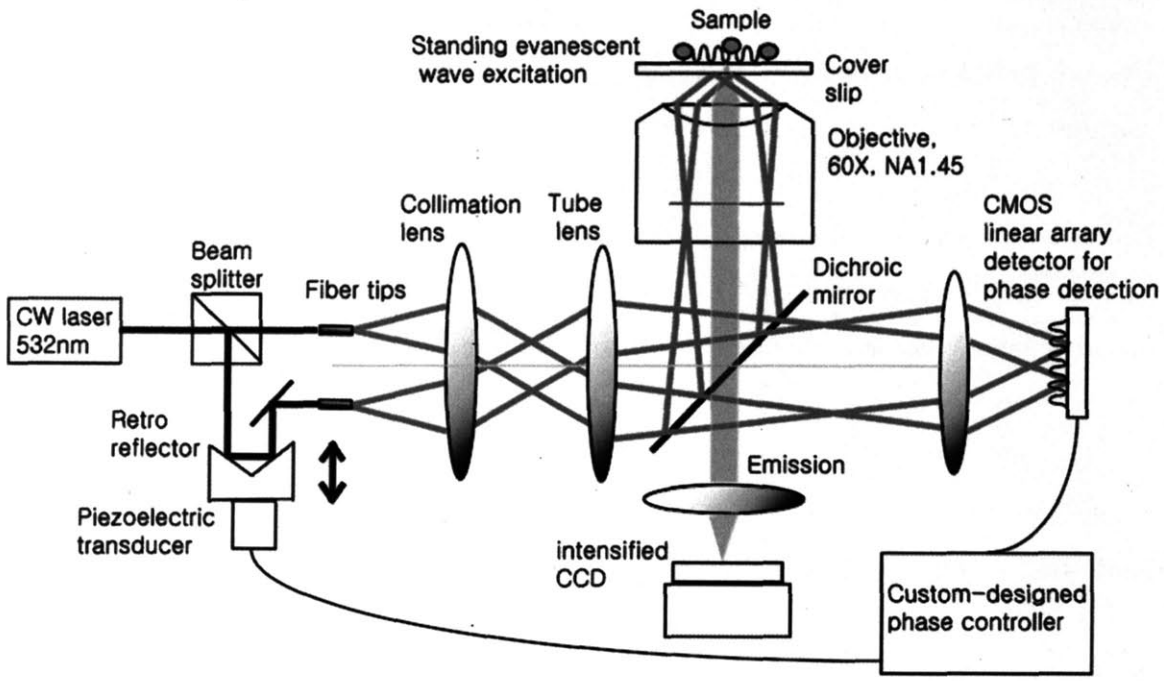

Fig. 3.2 Schematic of the objective-launched SW-TIRF microscope: A high NA objective is used to excite the sample at super-critical angle. The evanescent standing wave phase is controlled by driving a PZT attached to a retroreflector mirror. A linear CMOS array detector is used to estimate the standing wave phase with residual beams through the dichroic mirror.

3.2.1 Generation of evanescent standing wave excitation

- **The light source and the fiber optic light delivery**

The excitation light from a laser (532 nm, Verdi-10, Coherent) is delivered to the system via a single mode fiber through a fiber coupler (PAF-X-11-532-PC fiber coupler, OFR, Caldwell, NJ). This laser is a 5W, single wavelength Nd:YLF laser with a coherence length on the order of kilometers. Approximately 10% of the pumping beam was directed into the fiber coupler by using an AR-coated coverslip from Chroma. The isolation of the laser source from the optical setup was necessary to minimize the effect of the mechanical vibration of laser cooling. The final polarization of the single mode fiber output beam undergoes a slow variation over time due to the thermal expansion caused by the environmental temperature or external disturbances. This problem was

fixed by the use of polarization preserving fiber with an additional half-wave plate in front of the fiber coupler to accurately match the polarization axis of the fiber.

- **The beam splitting unit and the PZT actuator**

The fiber-delivered beam comes out of a fiber collimator and enters through a 50:50 beam splitter. One beam is reflected from a retro-reflecting mirror attached to a piezoelectric transducer (PZT, P-810.10, Polytec PI, Auburn, MA) to vary the optical path length for controlling the SW interference fringe phase. The other beam passes through a combination of a half-wave plate and a linear polarizer to match the intensity of two final beams entering into the objective lens.

- **The standing wave launcher**

Each beam is coupled into a single-mode polarization preserving optical fiber (Oz optics, Ottawa, Canada) and the end fiber tips are housed in mirror mounts placed on XYZ-translators. Precise orientation and position control of the fiber tips are required with 5 degree of freedom (X, Y, Z, yaw, and pitch) to place the corresponding excitation foci at the back aperture of the objective lens. The separation of two fiber tips with simple translation determines the final incidence angle onto a coverslip. The divergent beams emitted from these fiber tips are collimated by a collimation lens (f = 200mm) and focused down by a tube lens (f = 125mm). To keep our TIRF illumination in S-polarization state, a linear polarizer is put in between the collimation lens and the tube lens (not shown in the diagram). This polarizer can be rotated to generate a P-polarization state for some studies.

- **The generation of standing evanescent excitation**

The excitation beams enter the modified epi-illumination light path of an inverted microscope (Olympus, IX-71) through its side port and are reflected by a dichroic mirror (z532dc, Chroma, Rockingham, VT) and focused at the back aperture of a high numerical

aperture (NA) objective lens (Olympus Plan Apo 60X NA1.45). The collimated beams emerging from the objective enter the specimen/coverslip interface at a supercritical angle with the beam diameter of several hundred μm. The incident angle is set at $67 \pm 0.5°$ which is above the critical angle of 65.2° assuming the index of the specimen as 1.38 and that of the coverslip as 1.52. By simply translating the excitation fiber launcher position, the setup can systematically vary the incidence angle over a range of from 41.2° to 72.5° which makes it easy to switch imaging modes between the SW fluorescence microscope to the SW-TIRF microscope.

- **The standing wave illumination spot size**

The beam diameter at the output of the objective lens was about 300 μm. Since the field of view on the CCD camera is about 12×12 μm^2, this large spot size ensures uniform sample illumination within the field of view even though the beam has originally Gaussian intensity profile.

With the current design, conventional TIRF images can simply be obtained by blocking one of the beams and a conventional wide-field image can be taken by locating one beam at the center or optical axis while blocking the other. This will be used for the comparison of different imaging modes.

3.2.2 Imaging components

The fluorescence emission is collected by the same objective and transmitted through the dichroic mirror along the emission path. An additional barrier filter (HQ545LP, Chroma, Rockingham, Vt) is used to further attenuate the scattered excitation light. The emission out of the bottom port is transmitted through a 16 times magnification relay optics before focusing onto a 12-bit intensified CCD (iCCD) camera (Pentamax, Princeton Instrument now Roper Scientific, Trenton, NJ) with the effective pixel size of 22.6μm. With the 60× lens, the total magnification of this system is 960. The residual excitation beams, leaked

through the back of the dichroic mirror, exit through a hole bored in the back wall of the dichroic mirror cube. The residue excitation beams are expanded to form an interference pattern on a CMOS sensor for the SW phase detection.

3.3 Standing wave phase control

3.3.1 Standing wave stability and noise sources

The SW-TIRF system is basically an interferometer. Due to the thermal expansion and mechanical instability of the excitation beam path, the phase of the standing-wave can drift over time (~ 100° /min) and degrade the quality of the final reconstructed image. Thus, it is required to use a closed-loop feedback control of the SW phase. Since the evanescent standing wave spacing (about 190 nm for typical SW-TIRF experiment) on the coverslip is below the resolution of the imaging system (measured about 260 nm with NA 1.45 objective), an indirect way of phase estimation is devised. This is done by generating another alternative interference pattern onto a CMOS camera (S9227, Hamamatsu, Bridgewater, NJ) with about 10X magnification relay optics at the back of the dichroic mirror mount.

3.3.2 Standing wave phase extraction algorithm

From the output of the CMOS array, an algorithm is implemented to calculate the fringe period and estimate the SW phase in real time. We came up with two ideas how to implement this. One idea was Fourier transforming the CMOS data and getting the period and phase from the amplitude and phase component of the transformed result. From Matlab simulation, this phase extraction appeared to be problematic. Even a little noise could be amplified hindering the extraction of the phase information. In addition, the computation time of the Fourier transform interferes with the real time processing. The other idea was to estimate the SW phase in the space domain given that the intensity

signal is basically sinusoidal. This method turned out to be very stable and can operate well even with contrast less than 0.1 in the presence of significant noise. The algorithm is described below.

Assume that the Nyquist limit is satisfied and the AC component of the normalized fringe pattern can be described as $\cos\left(2\pi(i-1)/M+\phi_0\right)$, where i is the pixel position along the CMOS array and M is the closest integer number to the actual fringe period. The fringe phase, ϕ_0, can be obtained from $\phi_0=\tan^{-1}\left(\sin\phi_0/\cos\phi_0\right)$ after forming and solving the matrix equation below.

$$\begin{bmatrix}\overline{p}_1\\ \overline{p}_2\\ \cdots\\ \overline{p}_M\end{bmatrix}=\begin{bmatrix}1 & -0\\ \cos\frac{2\pi}{M} & -\sin\frac{2\pi}{M}\\ \cdots & \cdots\\ \cos\frac{2\pi}{M}(M-1) & -\sin\frac{2\pi}{M}(M-1)\end{bmatrix}\begin{bmatrix}\cos\phi_0\\ \sin\phi_0\end{bmatrix} \tag{3-1}$$

Here, $\overline{p}_i$ is the average AC intensity value of the ith pixel within the period of M. Since about 50 fringes can be recorded by the CMOS array, the 50 values were averaged to provide a single average pixel value of $\overline{p}_i$.

Interestingly, this equation turns out to be a simple algebraic expression for both $\cos\phi_0$ and $\sin\phi_0$ with a common constant factor:

$$\begin{aligned}\cos\phi_0&=\sum_{i=1}^{M}\overline{p}_i\cdot\cos\frac{2\pi}{M}(i-1)\\ \sin\phi_0&=-\sum_{i=1}^{M}\overline{p}_i\cdot\sin\frac{2\pi}{M}(i-1)\end{aligned} \tag{3-2}$$

In our setup, the CMOS array has 512 pixels with the pixel size of 6.4μm. Hence M, which is approximately equal to 6 pixels, denotes the number of pixels corresponding to

one period of fringes. In principle, M can be estimated by Fourier transform of the signal and taking closest integer of the corresponding pixel value. However, the algorithm described above works even when the actual fringe period is a bit off from an integer value.

3.3.3 Feedback controller design and noise reduction

The SW phase drift was removed by a feedback control system utilizing an embedded microprocessor (SBC0486, Micro/sys, Montrose, CA) driving the piezo-driven retro reflector. The feedback signal is provided by the estimated phase of the interference pattern on the CMOS. Typical proportional, integrative, and derivative (PID) control scheme was used and the gains were tuned using Zigler-Nichols method (Palm, 2000). We identified the noise sources such as the chiller for laser cooling, room air conditioner, and the ambient air flow. By Fourier transformation of the phase signal over time, the contribution of each noise source were evaluated and minimized. The slow drift of the phase could be minimized by covering most of the beam path and attaching optical fibers on rigid part. The fast fluctuation was reduced by isolating any mechanically moving sources from optical table except a cooling fan inside the iCCD used. Later we even modified the iCCD camera such that a toggle switch was installed at the power line of cooling fan allowing the fan to be turned off during data acquisition. Since the dominant noise source of the standing wave phase was this fan, we could achieve much cleaner data by temporarily stopping the fan during the measurement time usually less than a second. The iCCD performance was intact even about several minutes without running the fan. Also, one major vibration source was the room air conditioner which was turned off during imaging.

After turning on the feedback controller, the SW phase fluctuation was within 3°, smaller than 120^{th} of one period. This fluctuation was small enough not to cause visible problem in the final SW-TIRF image. SW phase error could come from the sample, to be discussed in Section 4.3.

3.3.4 Validation

The active phase control system provides sufficient phase stability to ensure proper SW-TIRF images. **Fig.** 3.3 shows the capability of current feedback controller. Once this controller was installed, we evaluated the accuracy and precision of this phase control system based on the CMOS detection. Since there is no way to directly observe the standing evanescent wave, the fringe spacing is about 190 nm and the best resolution with NA 1.45 lens was about 260 nm in PSF FWHM, we devised an indirect way to confirm the presence and stability of this standing evanescence wave. We imaged sparsely distributed point-like objects, 0.04μm fluorescent microspheres (peak excitation at 540 nm, peak emission at 560 *nm*, F-8792, Molecular Probes, OR) while changing the standing evanescent wave excitation from phase 0° to 720°. By plotting several different spots of blinking points with respect to phase, we demonstrate clean and stable sinusoidal illumination can be imposed on the specimen as is evidenced in **Fig.** 3. 4.

The fact that P-pol standing wave contains some contrast as described in Chapter 3.2 enabled to use the same phase control approach, originally for S-pol SW geometry. The SW-TIRF using P-pol was also confirmed in the way described above. As predicted in section 2.3.1, the P-pol SW gave a lower contrast yet enough for the current controller to work. This aspect led us to attempt even standing wave surface plasmon resonance fluorescence microscopy using only P-polarization, to be described in Chapter 5.

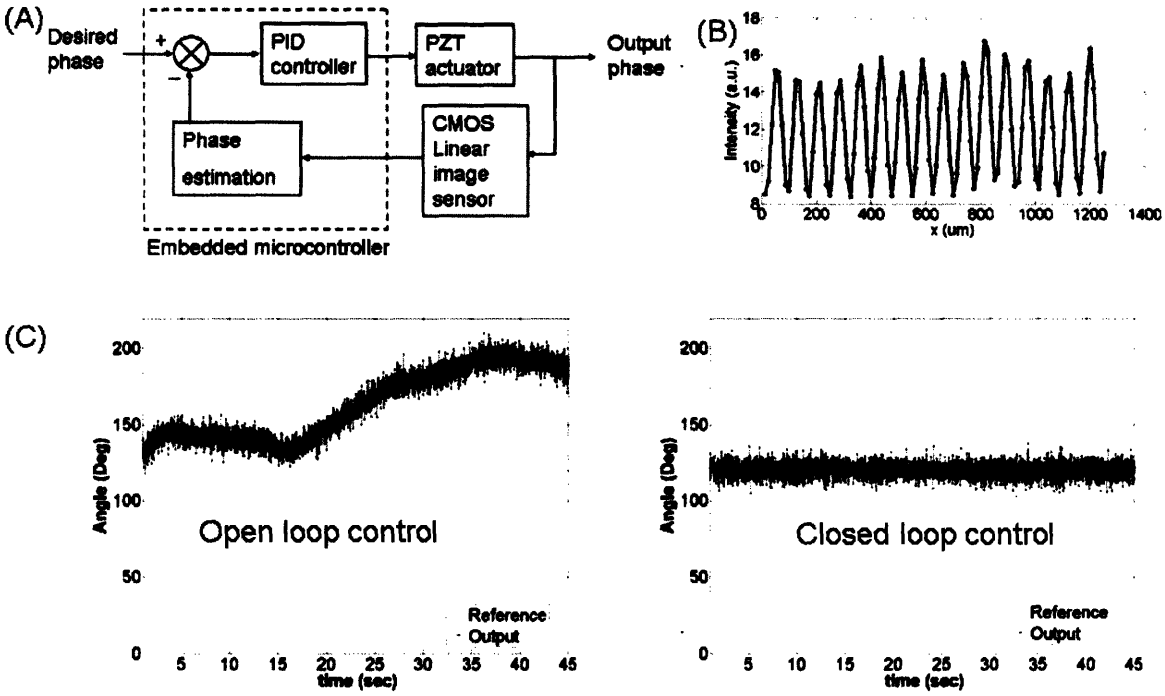

Fig. 3.3 Standing-wave phase control with closed-loop feedback controller
(A) Schematic diagram of the standing wave phase closed-loop control unit. The embedded microcontroller monitors the output phase from the CMOS detector and this estimated phase is used to control input in real-time (~70Hz).
(B) Typical fringe pattern on CMOS image sensor. The invisible evanescent standing wave on the sample can be indirectly monitored with this alternative way.
(C) Standing wave fringe phase measurement with a feedback loop open (left) and closed (right). Reference angle: 120°, measurement duration: 0.2 – 45 sec. The standard deviation of the fluctuation is less than 3° .

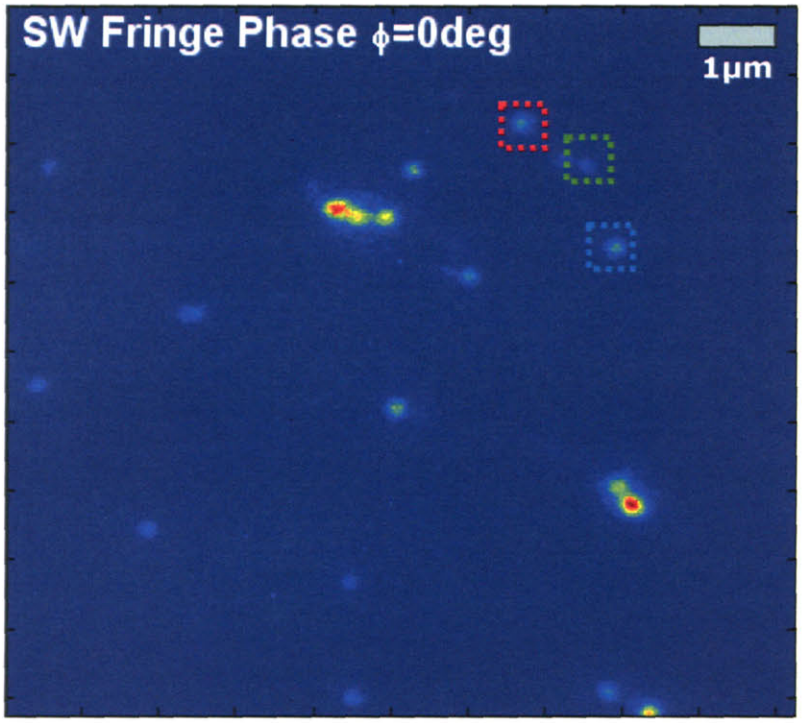

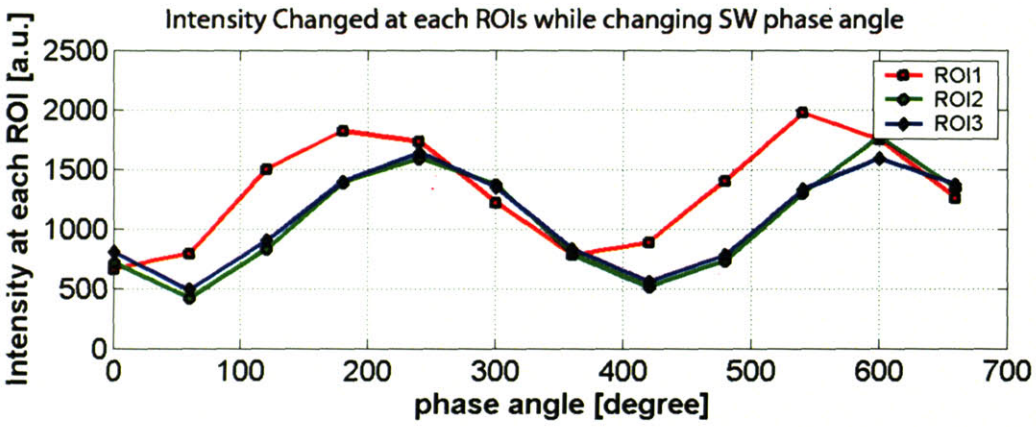

Fig. 3.4 Validation of the standing evanescent wave: the SW wave direction is vertical and the phase angle is changed from 0° to 660° by the step size of 60°.
(Top) One wide-field image with 0.04μm fluorescent microspheres sample at the standing wave phase of 0°. Three small rectangles are chosen regions of interest (ROI). (Bottom) The intensity trace at these three ROIs while changing the underlying standing evanescent wave. Note the lowest intensity signal is not zero which comes from the presence of background noise.

3.4 SW-TIRF system characterization and data acquisition

3.4.1 Calibration of pixel resolution

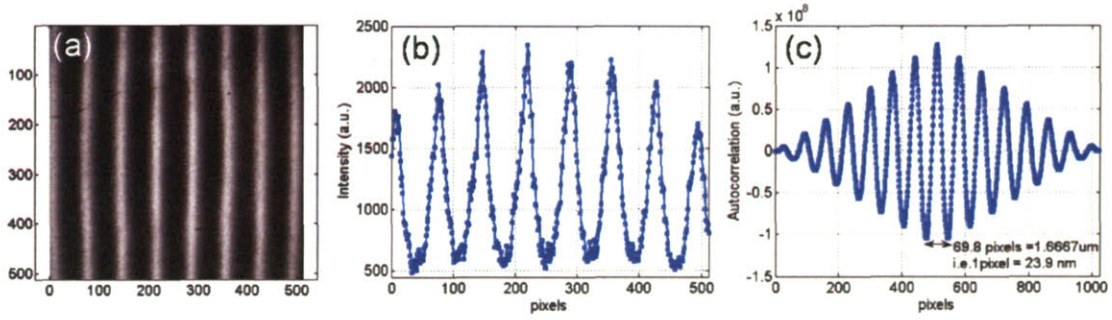

Fig. 3.5 Calibration of the pixel resolution and the field of view
(a) Direct Ronchi ruling image with bright light under typical SW-TIRF condition.
(b) Vertical average of the Ronchi ruling image in (a)
(c) Autocorrelation of the average

Even though there can be an approximate estimate of the field of view from the magnification of the objective lens and relay optics, it is best to measure the field of view directly imaging a known object. We determined the pixel resolution by using a glass Ronchi ruling (Edmund Optics, Barrington, NJ) with known spacing of 600 lp/m or 1.6667μm/period. **Fig.** 3.5 shows the method used to measure pixel resolution and the field of view. First, images were taken with the lines in vertical and horizontal directions. Then, the image was averaged to the direction parallel to the lines to generate a one dimensional plot. The autocorrelation of the image was used to determine the pixel resolution since there was noise even in the averaged images. With NA 1.45 objective, one pixel corresponds to ~ 23.9 nm and the field of view was ~ 12 × 12 μm^2. The reason we chose this method was to minimize the effect of image distortion which appears to be the result of spherical aberration. With the relatively large effective pixel size of 22.6μm of our CCD camera, we had to use rather large magnification relay optics (~16 times) in front of the CCD camera resulting image distortion. This effect could be reduced in the future with lower magnification relay optics by using a camera with smaller pixel size.

3.4.2 Calibration of evanescent standing wave fringe period

As mentioned before Chapter 3.3.4, the direct imaging measurement of the evanescent standing wave period was not trivial due to its sub-diffraction limit structure. Instead, a thin uniform layer of fluorescent sample was prepared and the SW emission was imaged by gradually increasing the incident angles from sub-critical angle, where SW can be imaged, to a super-critical angle where the SW cannot be imaged due to the resolution limit. This actual measurement of imaging SW fringes was matched with the theoretical calculation from geometry within 2 % and could be extrapolated to the setup angle of $70 \pm 0.5°$.

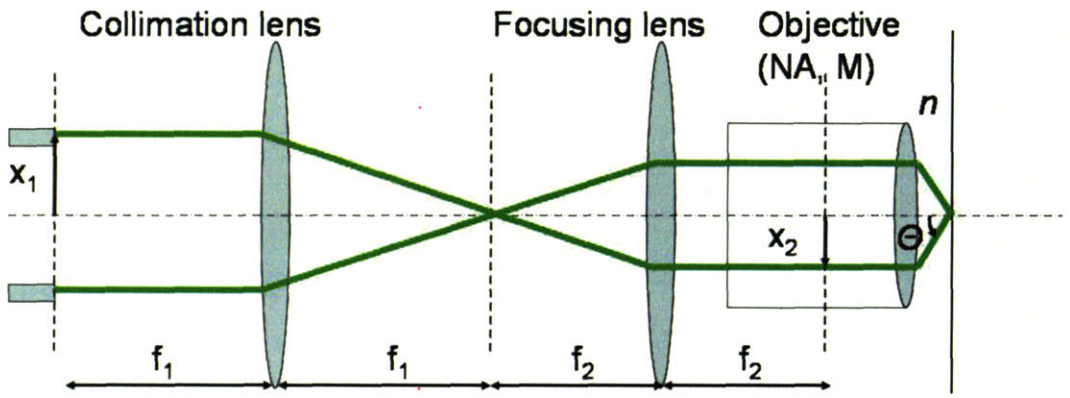

Fig. 3.6 Schematic diagram of SW-TIRF excitation geometry to calculate the standing evanescent wave fringe period: Only the center lines of the excitation beams are depicted. f_1 and f_2 are the focal lengths of the collimation lens and the focusing lens. The objective lens has magnification of M, with standard tube length of f_{TB} and a numerical aperture of NA. θ is the incidence angle of the entering beam.

To calculate the standing evanescent wave fringe spacing, a simplified diagram is described in **Fig.** 3.6. The fringe spacing at the sample plane is $p = \lambda / 2n\sin\theta$, where λ is the excitation beam wavelength, n is the refractive index of the immersion oil, and θ

is the incidence angle. From the sine condition of the objective lens (Richards and Wolf, 1959), the displacement of each beam, x_2, can be related to the angle θ via $x_2 = (f_{TB}/M)n\sin\theta$. Thus the fringe spacing can be expressed as a function of x_1:

$$p(x_1) = \frac{1}{2}\left(\frac{f_{TB}}{M}\right)\left(\frac{f_1}{f_2}\right)\frac{\lambda}{x_1}. \tag{3.3}$$

Experimentally, we increased the x_1 from its smallest value until the fringe of a thin layered sample was not distinguishable. Since we have pixel resolution, the fringe spacing can be obtained by counting the number of fringes in the field of view. Table 3.1 shows the comparison between the estimated value and the measured values.

x_1 (mm)	$\theta_{estimation}$ (°)	$p_{estimation}$ (nm)	$p_{measurement}$ (nm)	Error (%)
2.41	19.4	529.8	529.8	0.001
3.00	24.4	425.6	433.6	1.88
3.50	28.8	364.8	370.4	1.54
4.00	38.2	319.2	324.1	1.54
6.85	70.4	186.4	Not available	Not available

Table 3.1 Comparison between the estimated fringe spacing and the measured spacing

The estimated value is obtained from equation (3.3). With the current setup, the tube length is 180 mm and the magnification of the objective is 60. The error is within 2% and is used to extrapolate the fringe spacing of the standing evanescent wave. This is a pretty good match to have only about one period error over the entire field of view. The error may come from i) spherical aberration due to significant relay optics, ii) error in the manual counting of the fringe image, and iii) a slight misalignment of the optical setup. For example, the typical SW-TIRF setup used x_1 of 6.85 mm and the spacing was estimated as 186.4 nm. This value was used for our image reconstruction.

3.4.3 Data acquisition procedure and image reconstruction

The raw images from the iCCD camera were stored using a desktop computer with Windows 98, running the WinView (Roper Scientific, Trenton, NJ). The image data acquisition was synchronized with the real-time feedback control of the SW fringe phase by the embedded microprocessor (SBC0486, Micro/sys, Montrose, CA) using custom written software in C (Turbo C++ Version 3.0). The typical exposure time for each raw image was about 0.1- 0.2 sec with the total excitation power entering into the objective less than 10 mW. To minimize the photobleaching of the fluorophore, a mechanical shutter was used to restrict the illumination during the image acquisition. Non-fluorescent immersion oil (Olympus, n = 1.516 at 23˚C) was used. Each image was subtracted by a background image of the same sample without fluorophore under the same conditions.

Post image reconstruction and digital image analysis were performed on an IBM Thinkpad laptop computer (T40) using Matlab (Version 7.1, Mathworks, Natick, MA) software. The electronic post-processing takes a few seconds and potentially real-time reconstruction would be feasible with the development of computing technology.

Palm, W.J. (2000). Modeling, analysis, and control of dynamic systems, 2nd edn (New York, Wiley).

Richards, R., and Wolf, E. (1959). Electromagnetic diffraction in optical systems. II. Structure of the image field in an aplanatic system. Proc Roy Soc (London) A *253*, 358-379.

4. Results of Standing Wave Total Internal Reflection Fluorescence Microscope Measurements

Total internal reflection fluorescence microscopy was combined with standing wave microscopy to enhance the lateral resolution more than twice than that of conventional wide-field or TIRF microscopy. This new technique has been demonstrated with fixed biological specimen. The comparison between **wide-field** (WF), TIRF, and SW-TIRF (with linear deconvolution) shows that SW-TIRF can reveal the fine structural details of actin cytoskeleton with high signal-to-background ratio close to the basal plasma membrane of cells.

4.1 SW-TIRF point spread function measurements

The experimental measurement of point-spread function (PSF) of SW-TIRF microscope is demonstrated by imaging sub-diffraction limit fluorescence beads. This characterizes the resolution of SW-TIRF system. In addition, semiconductor crystal quantum dot imaging was performed.

4.1.1 Materials and methods

Fluorescent polystyrene microspheres (F-8792, Molecular Probes, OR), with nominal diameter of 44nm and peak emission at 560nm and excitation at 540nm, were sonicated for several minutes. 10μl solution was loaded on a cover slide followed by covering with a standard coverslip glass (22mm X 22mm square, No.1.5 thickness). The coverslip was sealed with clean nail polish to slow down the evaporation of water. Initially, most beads were moving due to Brownian motion. After overnight, most beads are attached on the coverslip and were ready for imaging. The number concentration of microspheres was adjusted to get about 10-30 beads in the microscope field of view (~ 12μm X 12μm).

4.1.2 Point spread function measurements of SW-TIRF microscope

A comparison of conventional TIRF PSF and 1D SW-TIRF PSF images is shown in **Fig.** 4.1. The sample contains fluorescent polystyrene microspheres in the deionized water. The intensity profiles in the standing wave (SW) direction show that the SW-TIRF PSF has narrowed by 239% improvement over the TIRF PSF in terms of FWHM. However, SW-TIRF has two prominent side lobes with amplitudes slightly less than 30 % of the main peak. This observation is consistent with theoretical prediction, **Fig.** 2.2(A), if the NA of the microscope objective were about 1.1. While the theoretical NA of the objective is supposed to be 1.45, the lower NA value is consistent with conventional TIRF measurement where PSF with FWHM of 260 nm is measured. This performance characteristic of the objective is consistent with in-house measurement by Olympus (Eiji Yokoi, personal communication) and will be further investigated in section 4.3. Nonetheless, since the relative height of side lobes compared to the main peak is less than 30%, linear deconvolution can quickly eliminate side lobes as shown in **Fig.** 4.1(c) (Hanninen et al., 1995). The PSF FWHM of the main peak remains unchanged after linear deconvolution. Prior to the SW-TIRF image reconstruction, no imaging processing was applied.

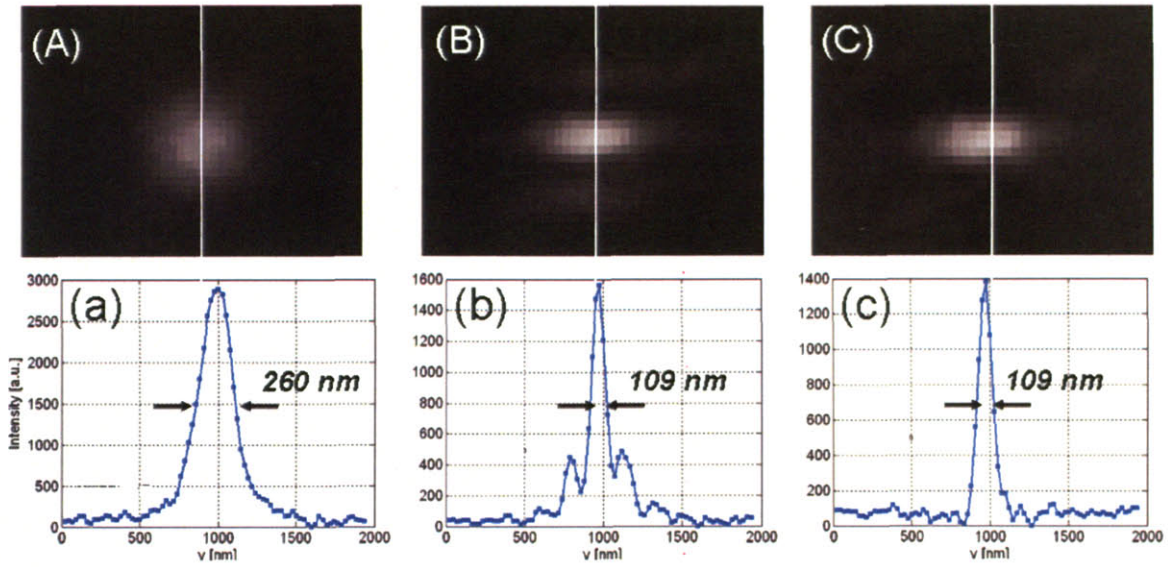

Fig. 4.1 Effective PSF measurement of (A) conventional TIRF, (B) 1D SW-TIRF and (C) 1D SW-TIRF with linear deconvolution with 0.04μm fluorescent bead. The evanescent standing excitation is in the vertical direction. The corresponding vertical intensity profile is (a), (b) and (c). These vertical profiles show a narrower PSF FWHM for SW-TIRF in comparison with that of conventional TIRF. (Experimental condition is the same as that of numerical simulation: NA = 1.45, λ_{exc} = 532 nm, λ_{emi} = 560 nm, n = 1.52, and $\theta_{incidence} = 67 \pm 0.5^{\circ}$ except the contrast was typically measured about 0.9).

4.1.3 Imaging semiconductor nanocrystals (quantum dots)

Semiconductor nanocrystal quantum dots possess ideal characteristic of point objects for PSF measurements. Their small size of 10-25 nm is far below the diffraction limit. Their long-term photostability is far superior to organic fluorescent dye molecules. Their broad excitation and narrow emission spectrums allow convenient multi-spectral imaging (Michalet et al., 2005). The sample preparation was similar to that of polystyrene microspheres except using quantum dots (Qdot565 streptavidin conjugated, Invitrogen). It was recognized that the quantum dots are prone to lose their signal if stored in diluted solution. In addition, their blinking nature was adverse to the SW-TIRF technique based on the quantitative signal of intermediate images.

The result is displayed in **Fig.** 4.2 with several region of interests (ROI) analyzed. The total input power into the objective was ~ 4.6mW. The results of 1D SW-TIRF gave higher lateral resolution of more than 2.5 times in one direction demonstrated in ROI 1 and 2. Interestingly, the ROI IV did not show enhanced resolution which might be due to the blinking of the quantum dot. Several different ways of blinking suppression were tried without success (Hohng and Ha, 2004). The use of betamercaptoethanol seems to work at first but is toxic to biological specimen and hence has minimal long term utility. In addition, the quantum dots lost their signals and degraded in a few days. By chance, quantum dot products from a different source (Evident technology, Troy, NY) were found to have much less blinking and were used for subsequent experiments, to be described later.

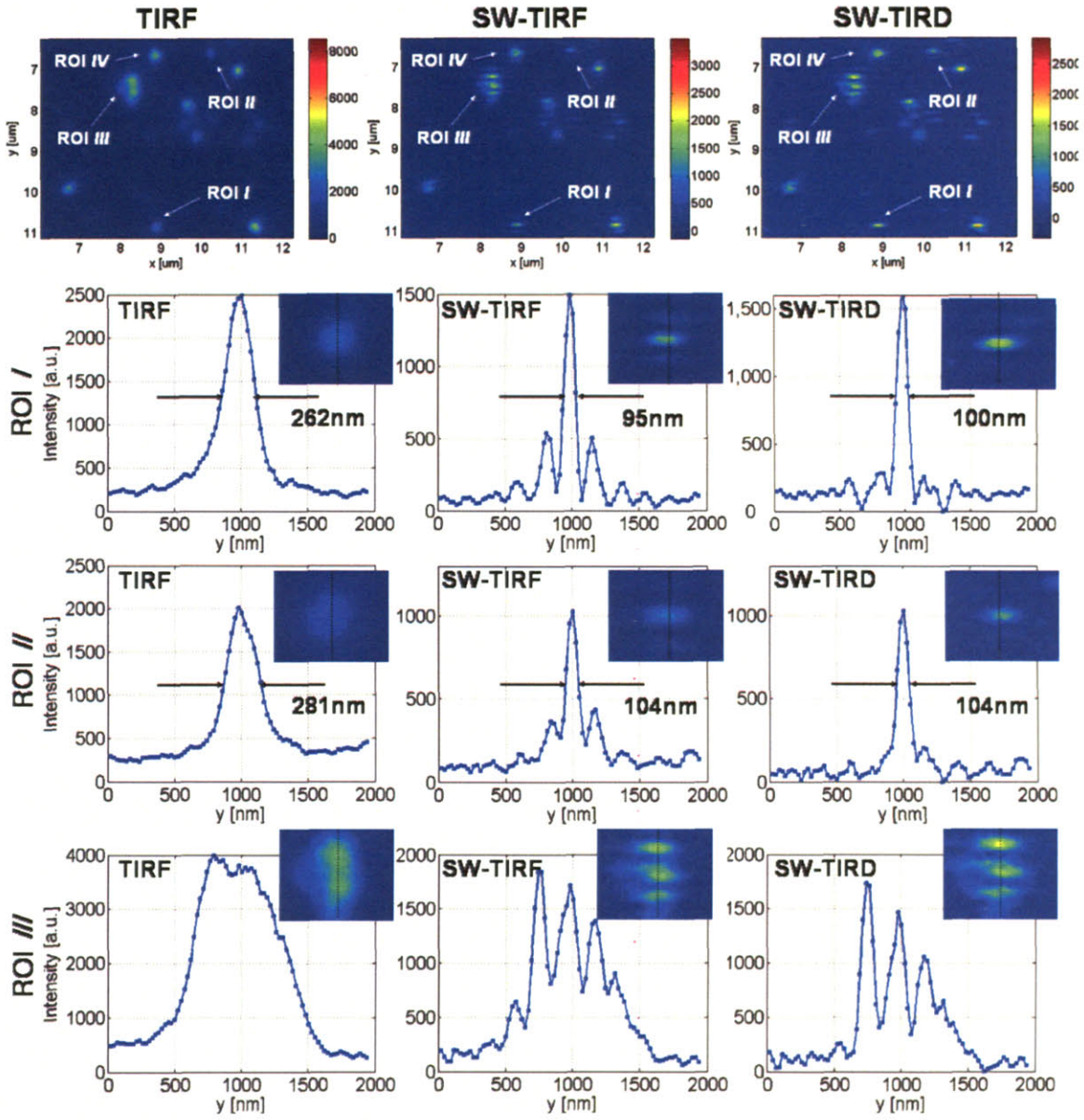

Fig. 4.2 The comparison of conventional TIRF, 1D SW-TIRF and SW-TIRD of semiconductor quantum dots. The standing wave direction:vertical , the exposure time: 1.0 sec, input power into the objective: 4.6 mW.

4.2 SW-TIRF measurement of Biological Specimens

With the SW-TIRF system established, a fixed biological specimen was imaged to demonstrate the high-resolution capability of SW-TIRF in biological systems.

4.2.1 Materials and methods (Cell culture and fluorescent labeling of the actin cytoskeleton)

Fibroblasts (NIH 3T3) were grown in standard 100mm x 20mm cell culture dishes (Corning, VWR, West Chester, PA) in DMEM (Cellgro®, Mediatech, Herndon, VA) supplemented with 10% fetal bovine serum (Invitrogen, Carlsbad, CA) and penicillin-streptomycin (100 units of penicillin per ml media, and 100 μg streptomycin per ml media, Invitrogen). Cells were cultured at 37°C in 5% CO_2. 24 hours prior to the labeling experiments, fibroblasts were plated on 35 mm glass-bottom cell culture dishes (MatTek, Ashland, MA) coated with collagen I (1 $\mu g/cm^2$, Cohesion Tech, Palo Alto, CA).

On the day of the experiments, the cell confluency had reached about 60%. At room temperature, cells were then fixed with 3.7% formaldehyde in phosphate buffered saline (PBS, Mediatech) for 10 minutes, washed twice with PBS, and extracted with 0.1% Triton X-100 in PBS for 5 minutes. To reduce nonspecific background staining, fixed cells were then incubated in PBS containing 1% bovine serum albumine (BSA, Polysciences) for 20 minutes. For F-actin labeling, cells were then incubated with 165-nM AlexaFluor® 532 phalloidin (Molecular Probes) for 20 minutes and washed three times with PBS. Ms. Maxine Jonas in our laboratory has taught and helped with the fibroblast preparation protocols.

4.2.2 Imaging actin cytoskeleton: one-dimensional SW-TIRF

Imaging of biological specimen is demonstrated in **Fig.** 4.3. Since the SW propagation is in vertical direction, one-dimensional (1D) SW-TIRF gives resolution enhancement only

in vertical direction. Wide-field (WF) image A(a) has higher background noise level while conventional TIRF image B(b) shows significantly lower background compared to WF due to the shallow evanescent excitation of about 73nm. However, the lateral resolution remains about the same with WF and TIRF. C(c) and D(d) show the SW-TIRF image and that with linear deconvolution, respectively. The SW-TIRF images reveal finer detail of the cellular actin cytoskeleton resulting in 235% enhancement in terms of lateral resolution compared to the WF image which demonstrates the high resolution capability of this system in the application of imaging cellular actin cytoskeleton. Stripe artifact is noticeable in SW-TIRF images due to the side lobes of the SW-TIRF PSF. This can be minimized by linear deconvolution of the SW-TIRF image.

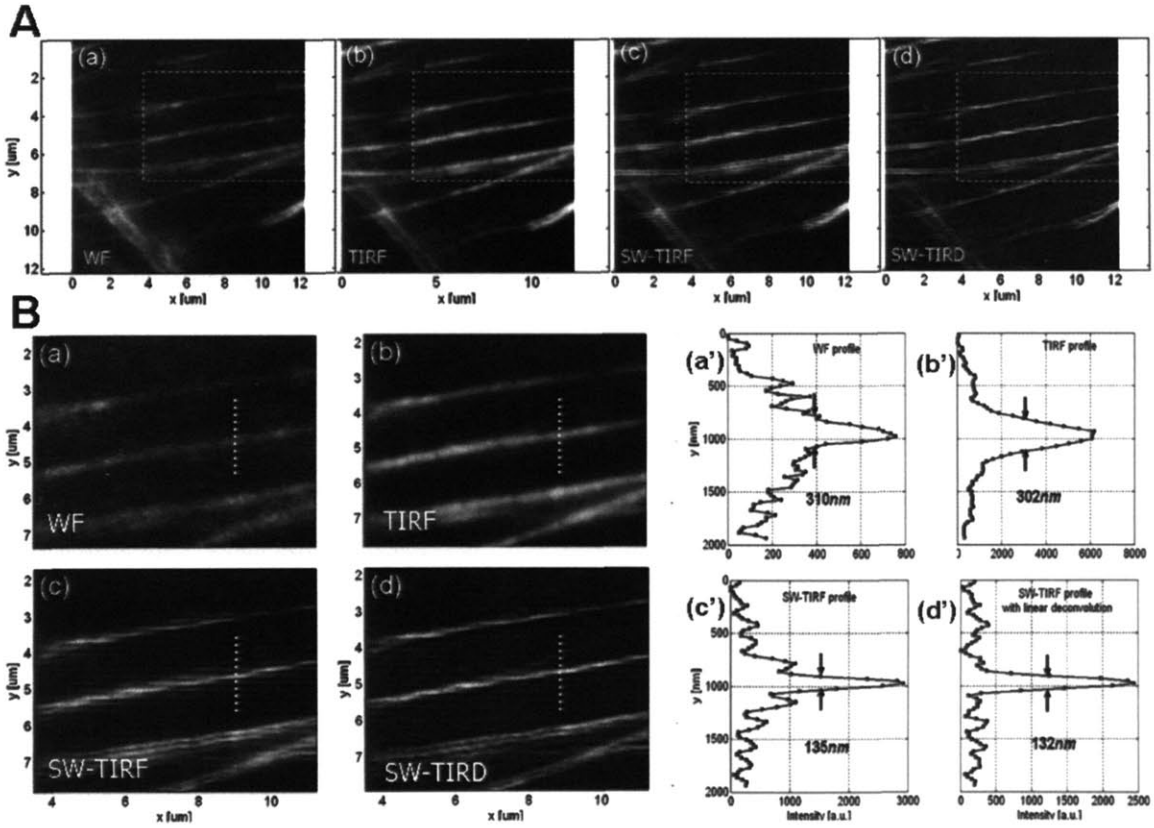

Fig. 4.3 F-actin cytoskeleton in mouse fibroblast cells (NIH 3T3) imaged with (a) Wide-field (WF), (b) conventional TIRF, (c) 1D SW-TIRF and (d) 1D SW-TIRF with linear deconvolution (SW-TIRD). (a,b,c,d) are enlarged insets of corresponding image from A(a, b, c, d). B(a1, b1, c1, d1) are the vertical profiles of dashed line in the corresponding image B(a, b, c, d). The evanescent standing excitation is in the vertical direction.

4.2.3 Imaging actin cytoskeleton: two-dimensional SW-TIRF

F-actin cytoskeleton structure of a single fibroblast cell was imaged by two-dimensional (2D) SW-TIRF in **Fig.** 4.4 showing resolution enhancement in both directions. Here, the superposition of two perpendicular directional 1D SW-TIRF was used to generate one 2D SW-TIRF image. For this, the sample was mounted in a mechanical rotataional stage. First, 1D SW-TIRF image was taken. Then, the sample was rotated by 90°. A low magnification CCD camera mounted on a different microscope port was used to ensure the region of interest remain within the field of view of the high magnification CCD camera during this rotation. Special care was required to minimize the inevitable photobleaching of the actin phalloidin by minimizing the excitation power during this sample rotation. To compensate the signal reduction from photobleaching, the 1D SW-TIRF images from the orthogonal orientations were normalized before the superposition. **Fig.** 6 A (a) and (b) show that TIRF decreases the out-of-focus noise to improve the signal-to-background ratio compared to conventional WF imaging at the cost of observing only near the surface region. In inset 1 of **Fig.**6 B, SW-TIRF can reveal the 190 nm separated actin fibers which is not resolvable with either WF or TIRF. In **Fig.** 6 C second row, FWHM of actin fiber is narrowed from 286 nm to 127 nm by more than twice. In third row, SW-TIRF can distinguish actin fibers separated by 190 nm. It is recognized that not all the actin fibers in one image are in focus due to the slight changes of actin fiber height from the bottom surface. These results clearly demonstrate the superior high-resolution capability of SW-TIRF over conventional WF or TIRF. Major difficulty of imaging biological specimen compared to the fluorescent beads is photobleaching problem. The beads are bright and can last relatively long period under continuous excitation while the actin phalloidin needs an extra care to minimize the total illumination time before fading away.

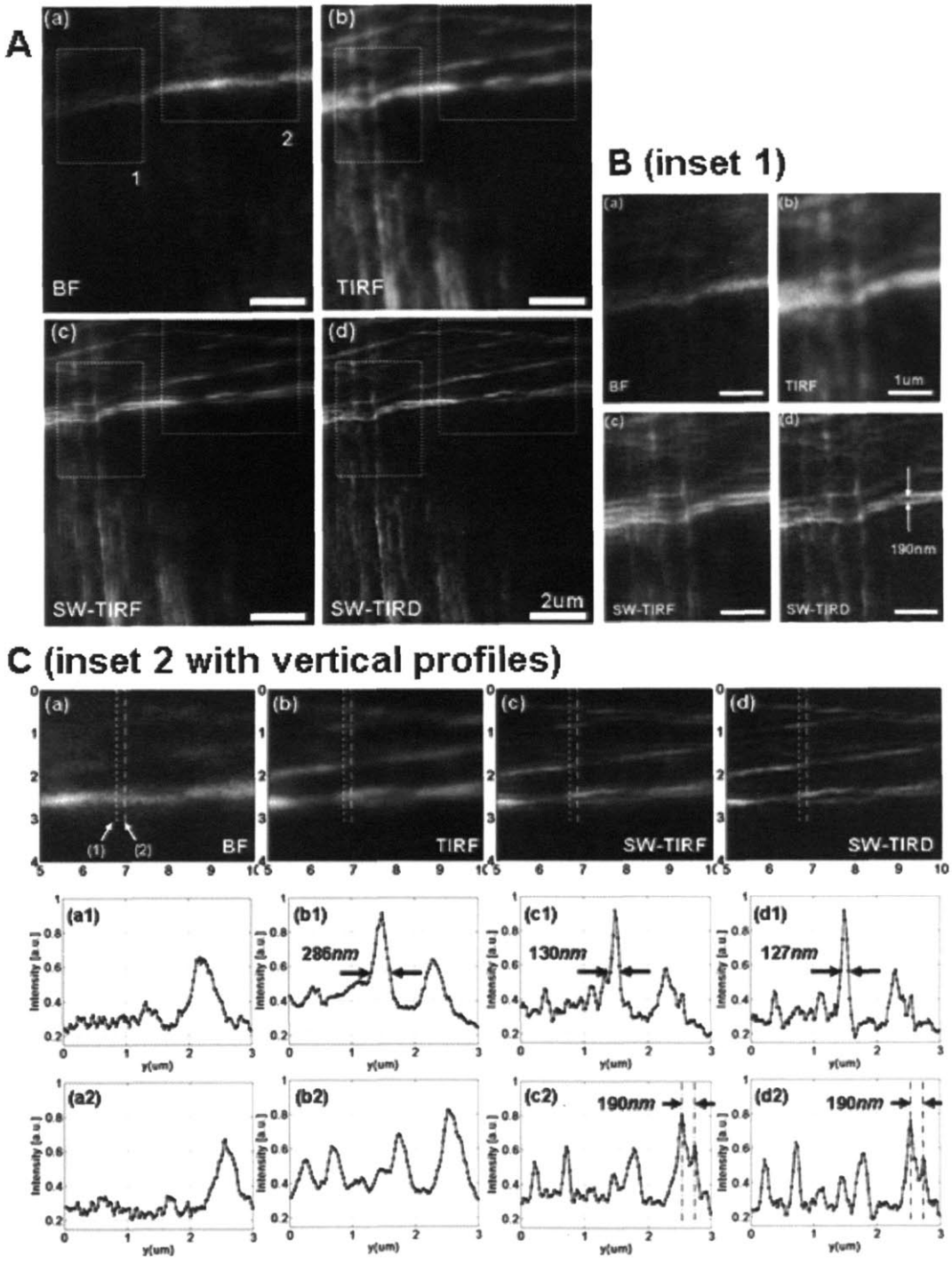

Fig.4.4 F-actin cytoskeleton in mouse fibroblast cells (NIH 3T3) imaged with (a) Wide-field, (b) conventional TIRF, (c) 2D SW-TIRF and (d) 2D SW-TIRF with linear deconvolution (SW-TIRD). Subfigure A compares the four different imaging modes and Subfigure B and C are the enlarged inset 1 and 2 marked in subfigure A. In subfigure C, the second and third rows are the vertical profiles of (1) and (2) in subfigure C(a).

4.3 Discussion

Total internal reflection fluorescence microscopy and a lateral version of standing wave microscopy were combined. This new technique has been demonstrated with fixed biological specimen for the first time. The comparison between WF, TIRF, and SW-TIRF shows that SW-TIRF can reveal the fine structural details of actin cytoskeleton with high signal-to-background ratio close to the basal plasma membrane of cells. Other complementary imaging modality such as atomic force microscopy could be combined with TIRF (Mathur et al., 2000; Sarkar et al., 2004) to provide high resolution imaging on the apical surface. We have further implemented SW-TIRF in objective-launched geometry instead of using prism-launched method to facilitate the ease of imaging cellular specimens.

From the theory of diffraction-limited imaging originally proposed as the Airy function, the ideal PSF FWHM is calculated to be 199 nm with NA of 1.45 and with the emission wavelength of 560 nm. In contrast, the measured PSF FWHM was 260 nm under the same condition with 44 nm bead. Since the relative height of side lobes of SW-TIRF depends on the shape of the original PSF, a discussion regarding the origin of this non-ideal PSF would be useful. First, the high NA microscope objective may not achieve the ideal modulation transfer function due to strong attenuation of marginal rays (Neil et al., 1997). Second, the emission from the fluorescent beads is not actually monochromatic at 560 nm but peaked at 560 nm with long spectral tail into the longer wavelength region. Third, the effect of bead size adds some broadening to the final PSF FWHM. However, from numerical simulation by convoluting the finite bead model with airy function gives the broadening of PSF FWHM of less than 5 % with a 44 nm size bead. Fourth, there exists cross talks between iCCD pixels due to the coupling fibers which connects the microchannel plate in the image intensifier to the CCD chip. The pixelation error is increased by a factor of 1.5 due to the fiber coupling ratio resulting in the effective pixel size of 22.6 μm instead of the physical pixel size of 15 μm (Stelzer, 1998). Other potential reasons could be the misalignment of the optical setup and the aberration of the relay optics. The broadening of PSF FWHM by 20 % was also reported in other systems (Frohn et al., 2000).

Frohn, J.T., Knapp, H.F., and Stemmer, A. (2000). True optical resolution beyond the Rayleigh limit achieved by standing wave illumination. Proc Natl Acad Sci U S A *97*, 7232-7236.

Hanninen, P.E., Hell, S.W., Salo, J., Soini, E., and Cremer, C. (1995). 2-Photon Excitation 4pi Confocal Microscope - Enhanced Axial Resolution Microscope For Biological-Research. Appl Phys Lett *66*, 1698-1700.

Hohng, S., and Ha, T. (2004). Near-complete suppression of quantum dot blinking in ambient conditions. J Am Chem Soc *126*, 1324-1325.

Mathur, A.B., Truskey, G.A., and Reichert, W.M. (2000). Atomic Force and Total Internal Reflection Fluorescence Microscopy for the Study of Force Transmission in Endothelial Cells. Biophys J *78*, 1725-1735.

Michalet, X., Pinaud, F.F., Bentolila, L.A., Tsay, J.M., Doose, S., Li, J.J., Sundaresan, G., Wu, A.M., Gambhir, S.S., and Weiss, S. (2005). Quantum Dots for Live Cells, in Vivo Imaging, and Diagnostics. Science *307*, 538-544.

Neil, M.A.A., Juskaitis, R., and Wilson, T. (1997). Method of obtaining optical sectioning by using structured light in a conventional microscope. Optics Letters *22*, 1905-1907.

Sarkar, A., Robertson, R.B., and Fernandez, J.M. (2004). Simultaneous atomic force microscope and fluorescence measurements of protein unfolding using a calibrated evanescent wave. Proc Natl Acad Sci U S A *101*, 12882-12886.

Stelzer, E.H.K. (1998). Contrast, resolution, pixelation, dynamic range and signal-to-noise ratio: fundamental limits to resolution in fluorescence light microscopy. Journal Of Microscopy-Oxford *189*, 15-24.

5. Fluorescence Microscopy using Surface Plasmon Resonance

Surface plasmon resonance fluorescence (SPRF) microscopy is a wide-field optical imaging technique that utilizes the enhanced evanescent electromagnetic field of surface plasmons to excite fluorophores near to the surface of a metal film. The field enhancement effect of the surface plasmon resonance near to the metal film leads to efficient excitation of the fluorophores and strong fluorescence emission, thus increasing the signal to ratio of the image. Through back and front focal plane imaging of sub-diffraction-limited fluorescent beads, the experimental emission characteristics is compared with theoretical simulation. To our surprise, with an excitation at the surface plasmon angle, we found that the anisotropic emission of the fluorescent beads, collected through the metal layer, results in a doughnut-shape point spread function with multiple concentric rings which is explored with theoretical modeling.

5.1 Motivation

TIRF microscopy is commonly used for the imaging studies of the activities near the basal cellular membrane taking the advantage of a shallow evanescent excitation. TIRF has been used to monitor biomolecular interactions such as ligand-receptor binding (Schmid et al., 1998), ion channel dynamics on cell membranes (Sonnleitner et al., 2002), and endocytosis or excocytosis (Beaumont, 2003). The exponentially decaying evanescent field ensures that the excitation of fluorophores is confined within approximately 100nm from the interface between high and low refractive index media. This extremely thin excitation penetration depth is less than one fifth of the wavelength and is usually not observable in free space leading better rejection of background fluorescence than other imaging modalities like confocal or two-photon microscopy.

A variation of TIRF consists of putting a thin layer of metal coating on the coverslip glass substrate to produce surface plasmon resonance and to induce fluorescence emission. This technique has recently been applied to the study of the interactions between actin

and myosin cross-bridges in muscle contraction (Borejdo et al., 2006b). In essence, the fluorophores near the surface are excited by the enhanced evanescent field of the surface plasmons induced on the metal surface. The emission light, coupled back through the metal layer, exits through a collection lens and is captured by detection optics. This imaging technique of utilizing surface plasmon-coupled emission (SPCE) in a TIRF configuration offers several advantages over the conventional TIRF such as the reduction in detection volume due to the quenching near the metal surface and better suppression of background noise (Borejdo et al., 2006b). Henceforth, we propose this as a novel microscopy technique titled as the **surface plasmon resonance fluorescence** (SPRF) microscopy with a high NA TIRF objective lens.

5.2 Background

5.2.1 Electromagnetic field enhancement based on surface plasmon resonance (SPR)

Surface plasmon is the surface electromagnetic wave propagating along a metal and dielectric interface originating from collective electronic oscillations. Surface plasmon resonance (SPR) involves the resonant energy transfer between evanescent wave and surface plasmons resulting in the evanescent field enhancement. The nature of SPR is illustrated in **Fig.** 5.1. The geometry of electric field is perpendicular to the interface and thus only allows the SPR with P-polarized light with supercritical incidence angle.

A hemicylindrical or hemispherical prism is typically used in the Kretschmann-Raether configuration to induce surface plasmons (Raether, 1987). Using SPCE for an efficient fluorescence detection method with high sensitivity was first proposed by Lakowicz group. Their observation of fluorescence emission by illuminationg the fluoropheres near to a silver-coated glass substrate, revealed the highly directional nature of the emission with a potential increase in the collection efficiency up to 50% (Lakowicz et al., 2003).

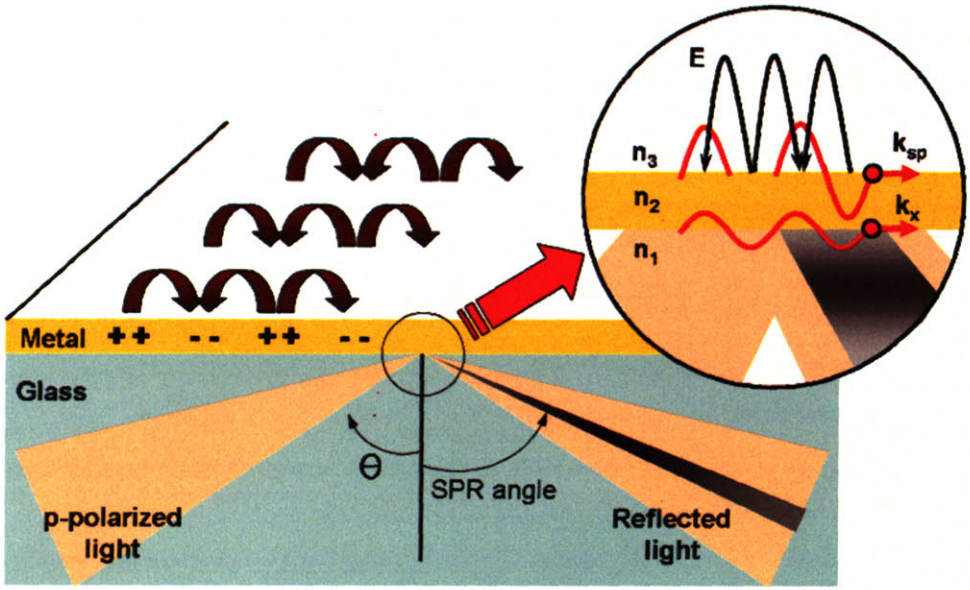

Fig. 5.1 Surface plasmon resonance (SPR) is excited by the P-polarization incident light at a metal/glass interface in a TIR geometry. The SPR enhances the evanescent field amplitude, E. SPR can be observed as a dip in the reflected intensity at a specific angle of reflection (SPR angle). The SPR requires the condition that the wave vectors for the photon k_x and plasmon k_{sp} are equal in magnitude and direction for the same frequency of the waves. θ is the incidence angle and SPR angle is usually greater than the critical angle.

5.2.2 Surface plasmon coupled emission (SPCE) in surface plasmon resonance fluorescence (SPRF) microscopy

A number of applications using SPCE has been found in the areas of biotechnology and biological measurements (Gryczynski et al., 2004; Lakowicz, 2004). For example, Malicka et al. demonstrated the use of SPCE in DNA hybridization measurements (Malicka et al., 2003), while Borejdo et al. extended the fluorescence correlation spectroscopy with SPCE to improve signal-to-noise ratio (Borejdo et al., 2006a).

The excitation by P-polarized light at the SPR angle in the Kretschmann-Raether geometry with a high NA TIRF objective lens is described in **Fig.** 5.2. Fluorophores near the metal coated surface are excited by the evanescent field of the surface plasmons. The

emission light is coupled through the metal layer and results in an interesting hollow cone shape of radiation at the back focal plane of the objective. SPCE is highly P-polarized and strongly depends on emission wavelength.

To our knowledge, there has not been any theoretical study of the image formation process of SPRF, especially the PSF characteristics. The angular emission pattern of SPCE will be studied at the image plane of the microscope (front focal plane) as well as its Fourier plane which corresponds to the back aperture of the objective or back focal plane. PSF measurements will also be presented. We propose a theoretical model for SPRF microscopy and derive its theoretical PSF within a 4F optical system to explain the observed PSF in our setup. The comparison between the theoretical prediction and the experimental data reveals an interesting nature of SPCE emission and pave the potential way for a new high sensitivity imaging modality.

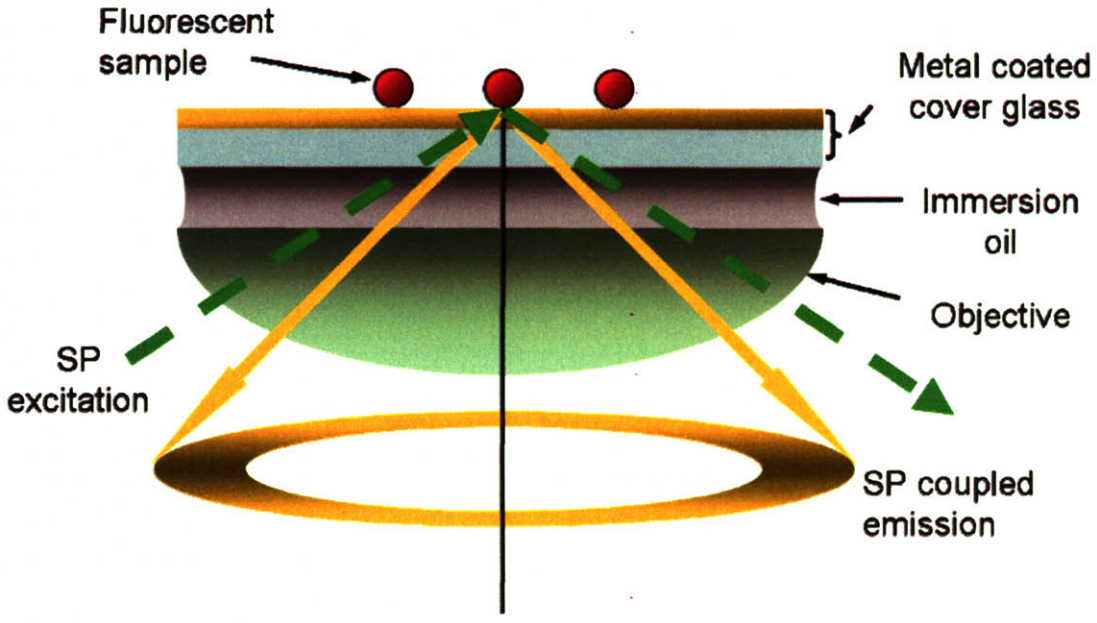

Fig. 5.2 The generation of surface plasmon coupled emission (SPCE) using a high NA TIRF objective for both excitation and collection of the emission

5.3 Theoretical simulations and experiments

5.3.1 SPR reflectance from a gold-coated substrate

Using Fresnel equation of three-layer model corresponding to the air/metal/glass layers, the reflectance with respect to the incidence angle is calculated in **Fig.** 5.3. For numerical simulation, gold (Au)-coated coverslip interfacing with air is used and the reflectance shows a very sharp dip near the SPR angle. The reflection is highly dependent on the incident angle. The angle with lowest reflectance corresponds to the SPR angle.

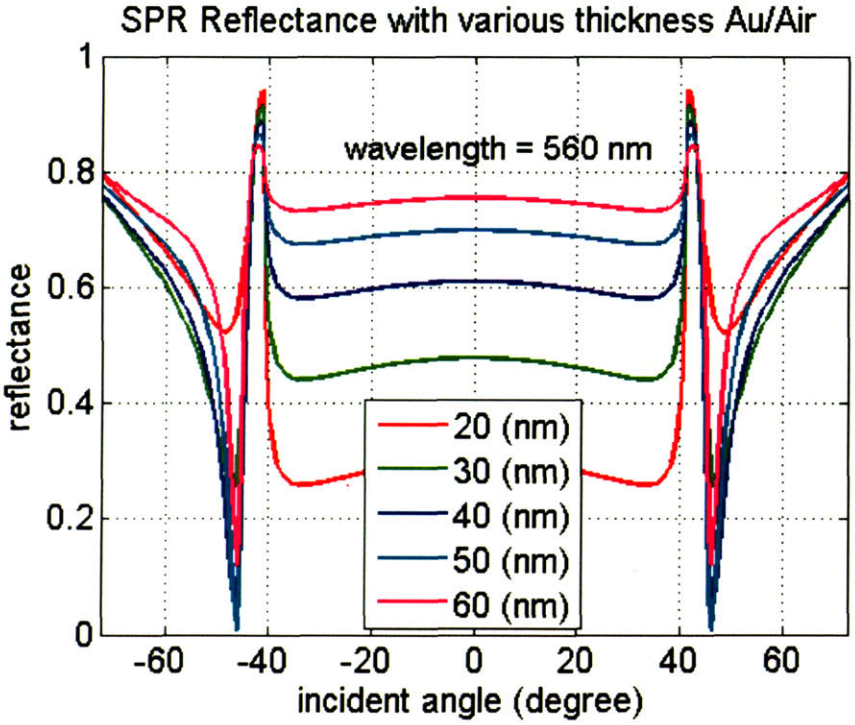

Fig. 5.3 Total reflectance with respect to incident angle for various gold coating thicknesses using the Fresnel equation of three-layer model (glass/metal/air): The emission wavelength is assumed to be 560nm.

5.3.2 SPRF experimental setup with back and front focal plane imaging

The schematic of the SPRF microscopy is shown in **Fig.** 5.4. An inverted microscope (Olympus, IX-71) was used for normal imaging plane (front focal plane) and back focal plane imaging (Fourier plane of the image plane). Fluorescent beads with nominal diameter of 0.1μm (Molecular Probes now Invitrogen, peak excitation and emission are 540 and 560nm) were placed on a glass with a thin layer of gold (Au, 50nm thickness) using vapor deposition (EMF, Ithaca, NY). The sample was excited with a continuous was laser source (532nm, Verdi-10, Coherent). Emission light was collected with a high NA objective (Olympus Plan Apo, NA 1.45, 60X). A barrier filter (HQ545LP, Chroma, Rockingham, VT) was used to block the scattered excitation light. For back focal plane (BFP) imaging, the emission light exciting from the tube lens was captured on a CCD camera (Dage-MTI 100, Michigan City, IN). The front focal plane (FFP) image was magnified by 16 times and captured with an intensified CCD (Pentamax, Princeton Instrument, Trenton, NJ). The experimental setup is similar to that in (Chung et al., 2006) except that only a single beam was used with an additional back focal plane imager.

The conditions at which SPCE occurs were determined empirically and verified with theoretical calculations. This was done to ensure the PSF measurements were performed under SPCE condition. The polarization of the excitation beam was controlled by a linear polarizer between L1 and L2 in **Fig.** 5.4.

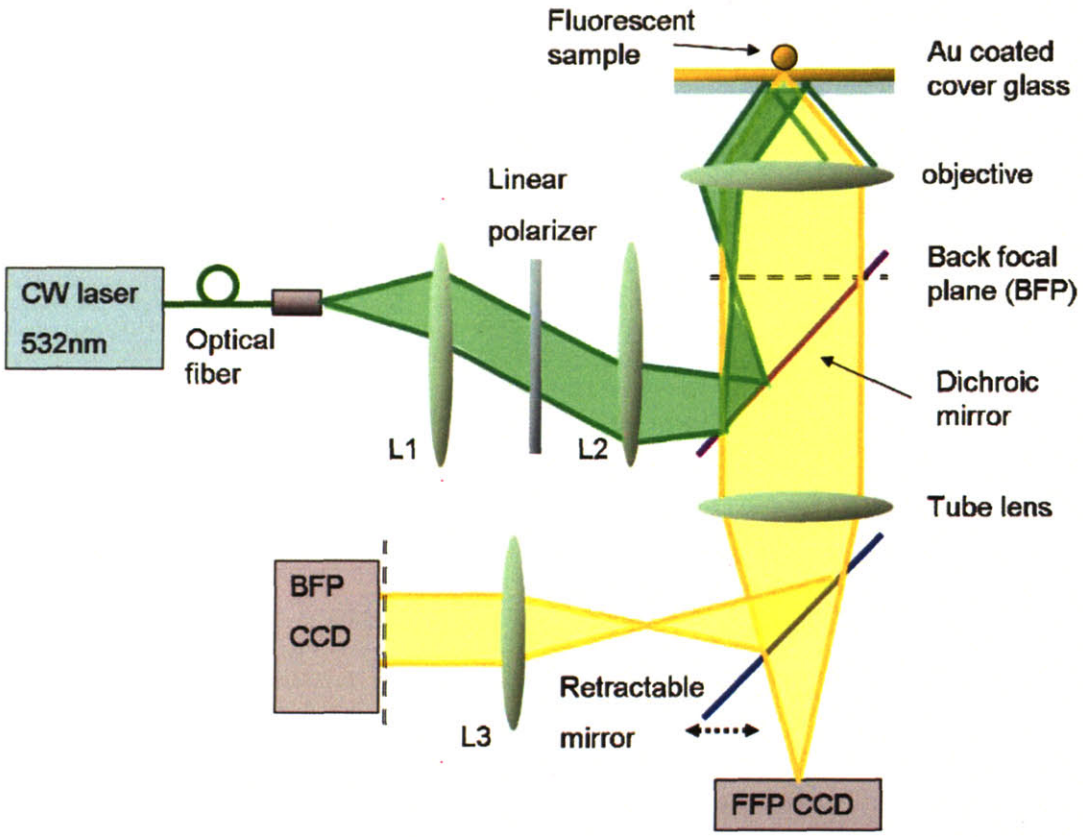

Fig. 5.4 Schematic diagram of the experimental setup of SPRF microscope: A high NA TIRF objective is used to collect the anisotropic SPCE. Both the back focal plane and the front focal plane images are capture by moving the retractable mirror in the setup. L1: collimating lens (f = 200mm), L2: focusing lens (f = 125mm), L3: BFP imaging lens, BFP: back focal plane, and FFP: front focal plane.

Fig. 5.5(a) shows the back focal plane image that was captured at the SPR angle i.e. the angle with strongest emission. The left panel shows the result of using a P-polarized excitation beam and the right panel was using a S-polarization with the same incidence angle. It is clear that SPR occurs only for a P-polarization excitation (Raether, 1987). Furthermore, the hollow cone of emission demonstrates the SPCE near SPR angle (Gryczynski et al., 2004; Kostov et al., 2005; Lakowicz, 2004; Mattheyses and Axelrod, 2005). For each of the P- and S-polarized excitation beams, the images of the BFP were obtained with various angles of incidence from 20° to 60° in steps of 5 or 10°. The comparison of collected fluorescence between experimental results and theoretical calculations is shown in **Fig.** 5.5(b). The radiant energy detected for the various

incidence angles was compared with that of the theoretical calculation in **Fig.** 5.5(c). The experimental results indicate that the SPR angle in our setup was approximately 45°. This is very close to the simulated value of 44.7°. These observations confirm that the SPCE phenomenon has occurred for a P-polarized excitation beam tuned at the SPR angle. In other words, the surface plasmons were induced and localized on the metal surface resulting in the excitation of the fuorophores near the metal surface. However, the simulation has much broader angular distribution than the theory. The reasons could be that the actual emission is actually spread over a broad range of wavelengths and the thickness of the metal layer was not very uniform which might smear the theoretically sharp peak. The fluorophore emission was then coupled back through the metal layer and collected by the high NA objective lens, leading to the hollow cone image in the BFP. Subsequently, the PSF images of SPRFM were obtained under the same resonance conditions.

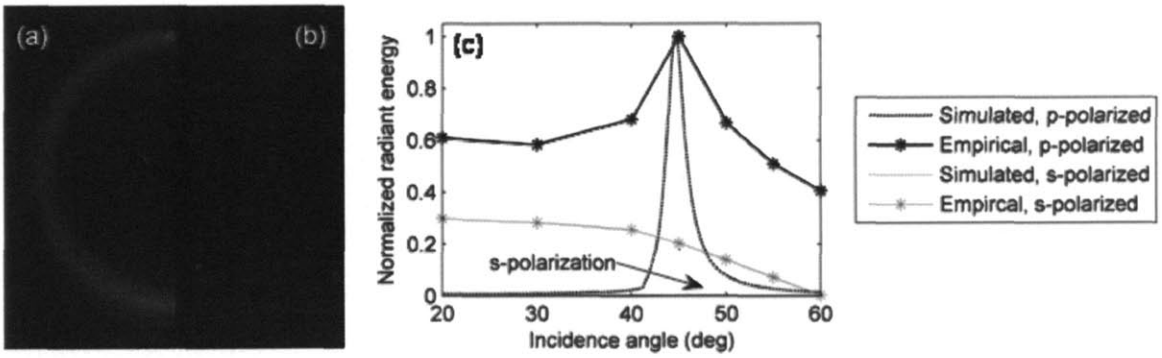

Fig. 5.5 Back focal plane image near the SPR angle (a) SPR occurs when *p*-polarized light in the glass is incident at the interface at the resonant angle of ~ 45°. This is evident by the hollow cone of radiation at the back focal plane, (b) No enhancement is observed when *s*-polarized light is used, and (c) A comparison of the detected fluorescence vs excitation angle for p-polarized and s-polarized light. From theory, the SPR angle is 44.7° which is very close to the experimental result

5.3.3 SPRF point spread function measurements

The FFP image of a 0.04μm fluorescent bead is in **Fig.** 5.6. Since the beads are of sub-diffraction-limited size, the image shows a unique doughnut shape PSF. To determine whether the PSF depends on the incidence angle, measurements were performed at two different incidence angles, at SPR angle (~45°) and at typical SW-TIRF microscopy angle (~70°). The results in **Fig.** 5.7 demonstrate the PSF shape is independent on the incident angle. However, the image obtained at 70° is much dimmer even with twice longer exposure time than at 45°, this is expected due to the low efficiency of plasmon coupling far from the resonance condition. Interestingly, this aberrant PSF shape were not observable with 0.1 μm beads because of the averaging effect of the larger bead size smearing the fine detail of SPRF PSF.

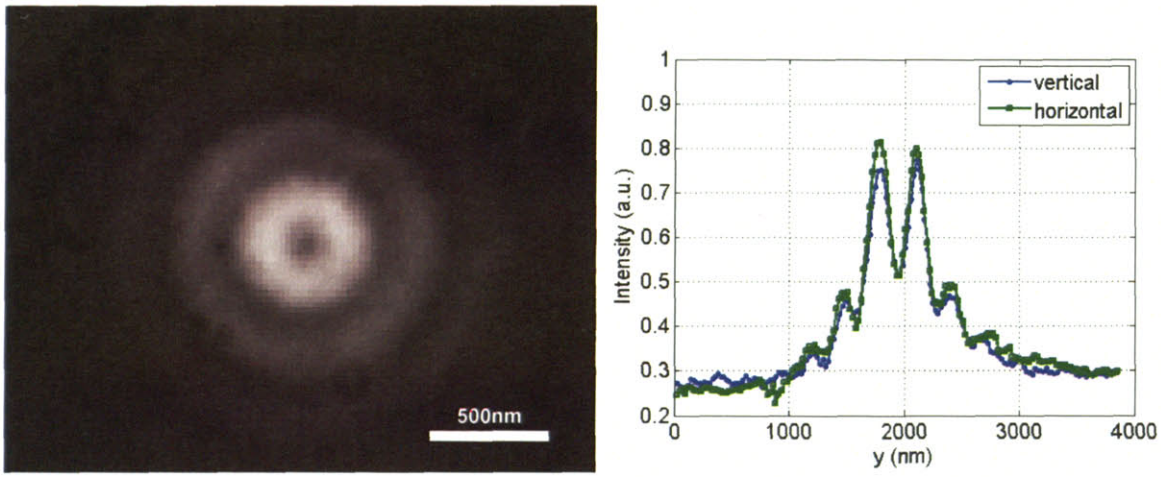

Fig. 5.6 The PSF image of the SPRF microscope with its vertical and horizontal profile. The sample was 0.04μm fluorescent microspheres (Molecular Probes now Invitrogen, peak excitation/emission: 540/560 nm) on top of Au (50nm)-coated coverslip glass. A TIRF objective (Olympus Plan Apo, NA 1.45, 60X) with immersion oil was used at the SPR angle. This image is averaged from 20 image data.

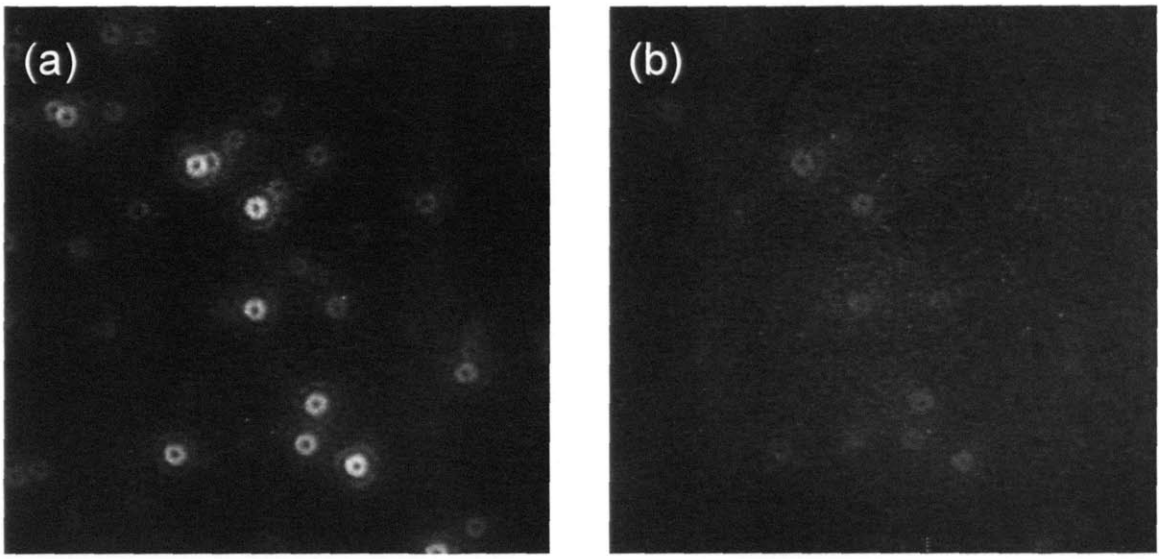

Fig. 5.7 PSF images at (a) SPR angle and at (b) nominal TIRF angle under the same condition except the exposure time: 4sec for SPR angle and 8sec for TIRF angle. SPR angle of ~ 45° and nominal TIRF angle of ~ 70° was used. Field of view is ~ 12 x 12 μm^2.

5.4 Theoretical modeling of SPRF microscope image formation

In this section, the interesting doughnut-shape PSF was explained based on vector field theory. The unique nature of SPRF microscopic image formation is modeled and used to compare with the experimental observation. This work was mostly done in collaboration with Mr. Wai Teng Tang and Prof. Colin Sheppard of the National University of Singapore. Only the core concept will be described and the detail can be found in the paper we are preparing.

5.4.1 Fluorescence excitation of a dipole in the object space

In SPRF microscope, dipoles on the metal-coated glass slide are excited by a P-polarized incident plane was shown in **Fig.** 5.8. n_1 denotes the refractive index of the object space, n_2 is the refractive index of the metal layer and n_3 is the refractive index of the glass slide. The dipole is placed as a distance d from the metal surface. k_3 is the wave number of the incident plane wave in medium 3 with an incidence angle of θ_i, and is given as $k_3 = 2\pi n_3 n/\lambda_0$, where λ_0 is the wavelength of the incident light in vacuum.

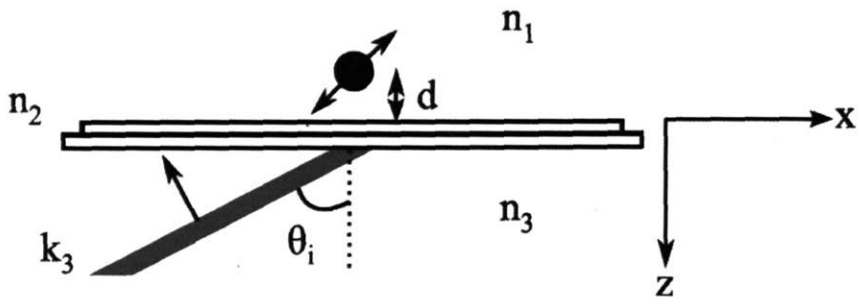

Fig. 5.8 Fluorescence excitation of dipole by a P-polarized incident plane wave

As the SPRF microscopy setup is essentially the same as TIRF system (Axelrod, 2001), the excitation field $\vec{E}_i$ of SPRF is simply given by

$$\vec{E}_i = -\frac{n_3}{n_1}\tau_P \exp(ik_3 \sin\theta_i \cdot x)\exp\left(-k_3\sqrt{\sin^2\theta_i - (n_1/n_3)^2}\cdot z\right) \times\left\{-i\hat{x}\sqrt{\sin^2\theta_i - (n_1/n_3)^2} + \hat{z}\sin\theta_i\right\}, \quad (5.1)$$

where $\hat{x}$ and $\hat{z}$ denote the unit vectors in the x and z direction and τ_P is the three-layer Fresnel coefficient for P-polarized light given by

$$\tau_P = \frac{t_P^{32} t_P^{21} \exp(ik_2 t\cos\theta_2)}{1 + r_P^{32} r_P^{21} \exp(2ik_2 t\cos\theta_2)}, \quad (5.2)$$

where t_P^{32} and t_P^{21} are the Fresnel coefficients for each of the respective two-layer interfaces and θ_2 is the angle in the metal layer given by the Snell's law defined in Chapter 2.

5.4.2 Electric field in the image space

Fig. 5.9 shows the typical setup of a 4F system for SPRF imaging. The point dipole $\vec{p} = \vec{\mu}\exp(i\omega t)$ at a distance d away from the first interface is excited by the field calculated in Eqn. (5.1) and emits light at a different wavelength λ from the excitation wavelength λ_0. Region 2 is a thin metal layer of thickness t with an index of refraction n_2. A high NA objective is placed in medium 3 and the tube lens in medium 4.

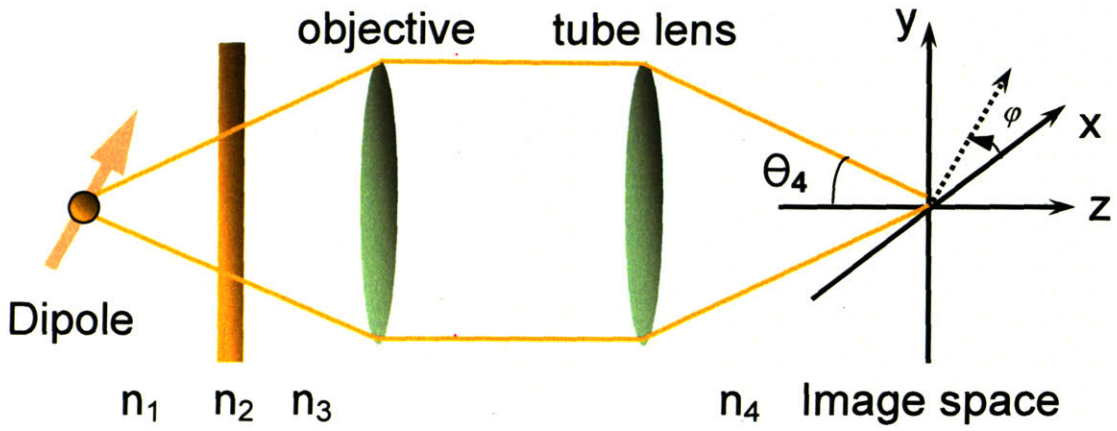

Fig. 5.9 A schematic view of the SPRF microscopy imaging process with a 4F optical system

Due to the highly polarized emission of SPCE and the high NA objective used, a full vectorial formulation will be derived for the model shown in **Fig.** 5.9, since a scalar treatment of the model does not take into account these effects and would be considered inadequate here. Using the vectorial Debye integral of Richards and Wolf, the field in the image space of the tube lens is given by

$$\vec{E}_4(r,\varphi,z) = -\frac{ik_4}{2\pi}\iint_{\Omega}\vec{E}_4'\sin\theta_4\exp\left(ik_4 r\sin\theta_4\cos(\phi-\varphi)\right) \times\exp\left(ik_4 z\cos\theta_4\right)\exp(i\Phi)\,d\theta_4 d\phi, \tag{5.3}$$

where the coordinates of a point in the image space are given by (r,φ,z), k_4 is the wave number in medium 4, θ_4 is the polar angle of the wave vector in medium 4 and ϕ is the azimuthal angle of the wave vector. It is assumed that as the wave propagates through the lenses, the meridional plane i.e. a plane containing the chief ray and the optical axis, of the propagation remains constant. Φ denotes the wave front aberration function which is a measure of the path difference between the wave front at the exit aperture of the tube lens and the wave front of an ideal spherical wave (Wolf, 1959).

To obtain the electric strength vector $\vec{E}_4$ in Eqn. (5.3), we start by considering the field emitted by the dipole in medium 1 which is subsequently transmitted into medium 3, and then propagate the waves through the 4F system into the medium 4. We note that although Torok solved the problem of the propagation of dipole waves through dielectric interfaces (Torok, 2000), we do not use his approach here, primarily because it was assumed that the distance of the dipole from the first interface is large and consequently, the contribution of the dipole evanescent wave was ignored. On the contrary, when considering SPRF, it is important to treat the case where the fluorophores are close to the metal surface, within the order of ten nanometers scale, which implies that the near field emission cannot be ignored. Therefore, we follow the procedure given by Arnoldus and Foley (Arnoldus and Foley, 2004) to obtain the field in medium 3. We note that the field in medium 3 has also been derived by Hellen and Axelrod (Hellen and Axelrod, 1987) in a similar way.

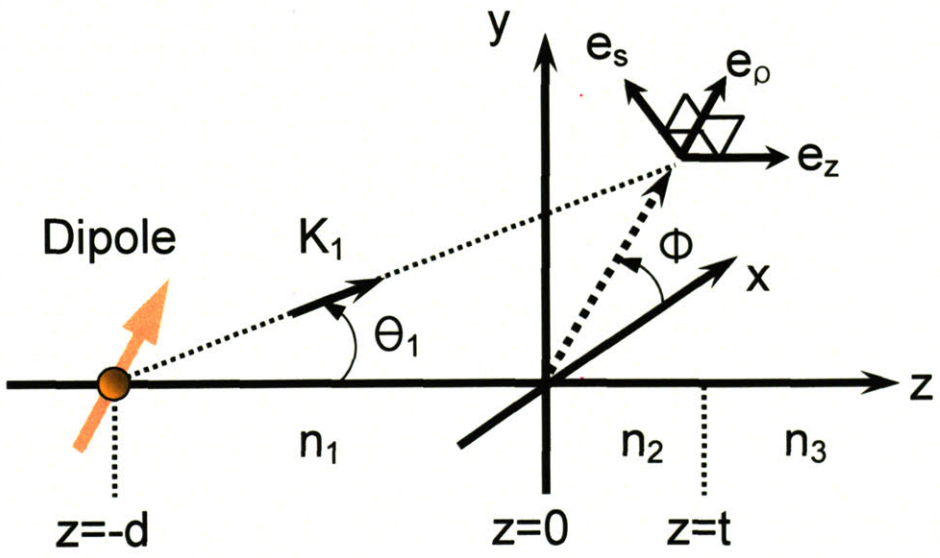

Fig. 5.10 Axis convention used in the derivation of the field in medium 3

Fig. 5.10 shows the axis convention that is used for obtaining the expression for the diple radiation in medium 3. The complex amplitude of the dipole source field in an infinite medium with the index of refraction n_1 is given by

$$\vec{E}_1(\vec{r}) = -\frac{i}{2\pi n_1^2}\int d^2k_{\parallel}\frac{1}{k_0\nu_1}\left[k_1^2\vec{p} - \left(\vec{p}\cdot\vec{k}_1\right)\vec{k}_1\right]\exp\left[i\vec{k}_1\cdot\left(\vec{r}+d\hat{z}\right)\right], \tag{5.4}$$

where $\nu_1 = \sqrt{n_i^2 - \alpha^2}$ and $\alpha = k_{\parallel}/k_0$ as introduced in (Arnoldus and Foley, 2004), and

$$\vec{k}_1 = \begin{cases} \vec{k}_{\parallel} + k_0\nu_1\hat{z} & for\ z > -d \\ \vec{k}_{\parallel} - k_0\nu_1\hat{z} & for\ z < -d \end{cases} \tag{5.5}$$

In Eqn. (5.5), the field in medium 1 is efficiently represented by an angular spectrum of plane waves, where the limits of integration indicate that both evanescent waves and traveling waves are taken into consideration.

To obtain the field in medium 3, it is necessary to decompose plane waves propagating in the positive z direction into their P and S components, so that the Fresnel transmission coefficient for the three-layer system can be applied. The detailed calculation procedure will be published (Tang, 2007) and the resultant intensity in the image space can be obtained from the electric field written in Eqn. (5.1).

5.4.3 Comparison of SPRF point spread functions between theory and experiment

The theoretical PSF and the experimental PSF are compared in **Fig.** 5.11(a) and (b) respectively. In general, their PSF look similar and it is evident that they exhibit doughnut-like structures with multiple concentric rings of diminishing intensity extending outwards. It is notable that the PSF is unique in that the central region has a "valley" that is not normally seen in conventional microscopy.

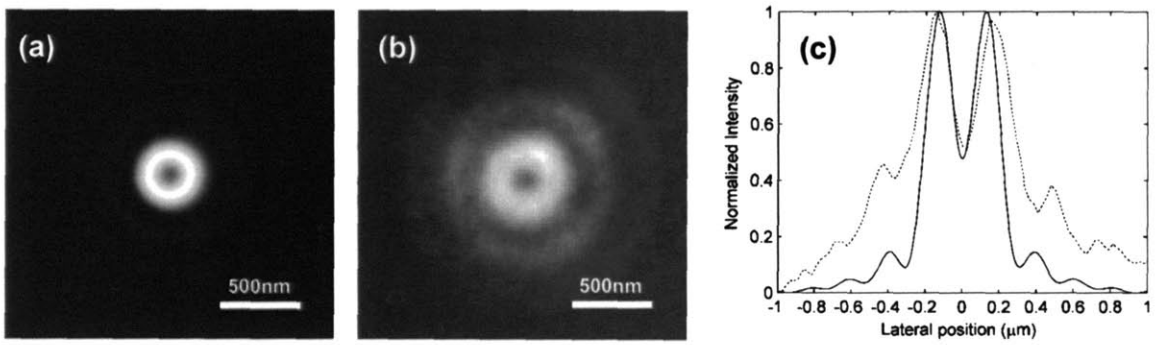

Fig. 5.11 A comparison of the calculated and experimental PSFs (a) Theoretical PSF, (b) Experimental PSF, (c) Cross-sectional profiles of the PSFS. The PSF of SPRF microscopy is shown with a black solid line and the experimental PSF is shown with dashed lines.

This effect is caused by the anisotropic emission of SPCE as a result of introducing a thin metal layer onto the glass coverslip. **Fig.** 5.11(c) compares the cross-section of the experimental PSF with that of SPRF theory. If we were to ignore the dip in the central region, the theoretical PSF of SPRF microscope has a FWHM of ~ 430 nm in comparison to the FWHM of ~ 590 nm for the experimental PSF. Furthermore, the rings in the experimental PSF are observed to be wider and more spread out than those of the calculated PSF. These discrepancies could be due to the difference between the size of the beads used in the experiment and the point dipole model used in the calculations. This is supported by the observation of normal looking PSF with bigger beads of size 0.1μm. Another potential reason is that the actual experimental emission spreads over a spectrum of wavelengths which causes the hollow cone of radiation to be wider than the theoretical predictions (Mattheyses and Axelrod, 2005), thereby resulting in a wider FWHM.

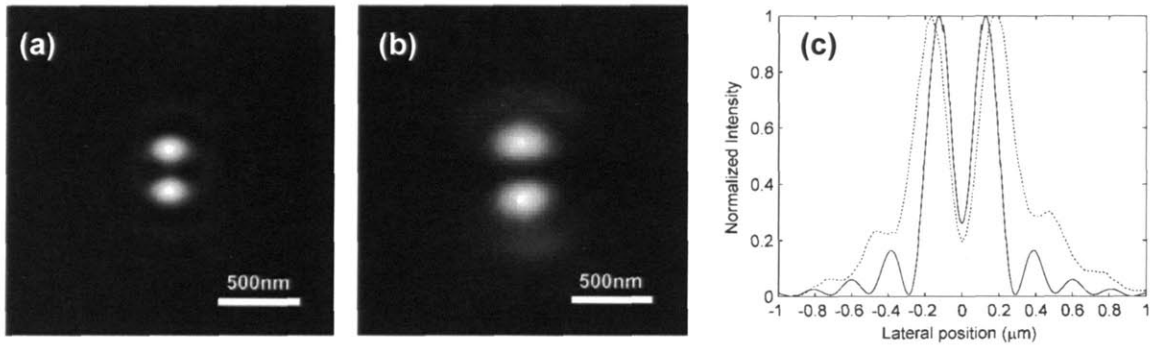

Fig. 5.12 A comparison of the calculated and experimental PSFs with a linear polarizer (a) Theoretical PSF by introducing a linear polarizer between objective lens and tube lens, (b) Experimental PSF with a linear polarizer in the relay optics, (c) Cross-sectional profiles of the modified PSFS. The PSF of SPRF microscopy is shown with a black solid line and the experimental PSF is shown with dashed lines.

When we have tried to put a linear polarizer in the collimated region of the relay optics, we found an anisotropic image shown in **Fig.** 5.12(b). Likewise, we calculated this effect in our theory and reached a similar result as in PSF case. This result reveals the unique axially polarized nature of the SPRF emission since the polarization of the emission between the objective and the tube lens is mostly P-polarized or radially polarized.

Although SPRF microscope is a potentially promising imaging technique due to its small detection volume and good background rejection, the irregular point spread function of SPRF microscopy implies that care must be taken when using this method for applications such as imaging biological specimens since artifacts may be inadvertently introduced. Though the overall PSF FWHM neglecting the central dip is about twice as worse than that of conventional optical imaging, the inside sharp structure may contain as high spatial frequency components as those of conventional counterpart. Thus this seemingly enlarged PSF problem may be easily mitigated by using proper deconvolution while keeping the advantage of enhanced signal-to-background ratio even further from that of the TIRF microscope.

5.5 Standing wave surface plasmon resonance fluorescence (SW-SPRF) microscopy

5.5.1 Motivation

The surface plasmon resonance is based on P-polarized incident light into a metal-coated substrate at a specific SPR angle, usually larger than the critical angle. As is shown in the section 5.3, SPCE is attractive due to its enhanced field near the metal surface, lower background emission and the sensitivity to the wavelength of lights involved and the dependence on material properties. More importantly, surface plasmon has an unusual dispersion property. The magnitude of wave vector of surface plasmon can be enlarged than that of free space light if the surface plasmon can be excited by proper coupling like total internal reflection geometry (Matsubara et al., 1988). Since the resolution of standing wave total internal reflection fluorescence (SW-TIRF) microscopy depends on maximizing the wave vector of the evanescent wave, surface plasmon offers a unique opportunity to substantially increase the magnitude of the evanescent wave vector. It should be noted that the launching of surface plasmons by light requires wave number matching (Raether, 1987). This momentum matching requirement can be achieved by various methods including grating-based launching approaches. However, the implementation of grating-based launching will require the fabrication of nano-scale grooves on the gold substrate and is currently beyond the scope of this thesis. Instead, we will use objective-based launching technique to create surface plasmon with lower wave vector. This experiment aims to demonstrate the feasibility of generating standing surface plasmon waves although it does not provide higher resolution than that of SW-TIRF microscope. The application of this method with grating-based launching technique to access plasmon closer to the plasmon frequency will constitute future work that may significantly improve the final image resolution.

However, the unique shape of SPRF PSF needs some care to be utilized for imaging without artifacts. In addition, the SPR angle may be fixed with given experimental

conditions setting the standing wave fringe period at smaller than that of SW-TIRF. Now that P-polarization excitation can also generate an evanescent standing wave explained in section 2.3, we came up with an idea that it may also be possible to apply SW-TIRF algorithm in our existing SPRFM. In this regards, the potential of SW-SPRFM was explored and a preliminary result was achieved.

5.5.2 Evolution of the SW-SPRF microscopy

As SPRF essentially adapts the same geometry of the TIRF, SW-SPRF can also use the same strategy used in SW-TIRF, which is already built (Chung et al., 2006). One consideration was whether SW-SPRF gives enough contrast to apply the SW-TIRF algorithm. In section 2.3.2, several parameters were calculated and over 77% contrast was feasible for air/gold/glass at the SPR angle of 44.7°. Experimentally SW-TIRF algorithm works well with a standing wave contrast larger than 70%. The other consideration was that the current CMOS phase detector for the standing wave phase estimation was originally designed for S-pol standing wave interference. The contrast for P-pol was substantially lower than S-pol case but it nonetheless gave sufficient contrast for stable feedback control.

One major complication is that the unique shape of SPRF PSF did not allow a direct use of SW-TIRF algorithm due to the central dip and overall widened PSF FWHM. A careful observation of the SPRF PSF profile revealed that all the major peaks in the SPRF PSF have FWHMs comparable with the FWHM of TIRF PSF which is about 260 nm. Therefore, the SPRF PSF contains about the same high frequency information as that of TIRF PSF as expected. Thus it was feasible to apply a deconvolution algorithm to convert the SPRF PSF into a more typical-looking PSF shape. Since we already have a fairly good numerical model of PSF, the Richardson-Lucy algorithm could be adapted with theoretical PSF kernel as an input. Experimentally measured SPRF PSF was also tried but produces relatively poor deconvolution results with slower convergence.

5.5.3 Results of SW-SPRF microscope measurements

The process of generating a SW-SPRF image is shown in **Fig.** 5.13. The sample was again the sub-diffraction-limited fluorescent beads sitting on the gold-coated coverslip glass. The incidence angle of the excitation beams, with P-polarization, were set at SPR angle of 45°. To generate an enhanced SW-SPRF image, three intermediate SPRF images (Orig SPRF) were taken with three different SW phases as in SW-TIRF imaging. Then, the deconvolution algorithm was applied to convert the original doughnut-shape PSFs into new images where each PSF is single-peaked (Decon SPRF) followed by the application of the SW-TIRF algorithm. These three deconvoled SPRF images were used to generate an enhanced image (Decon SW-SPRF) as well as the final one with linear deconvolution for side-band removal (Decon SW-SPRD). This result holds a promise for the SW-SPRF microscopy as a potential imaging tool with even higher signal-to-background.

The profile analysis of the SW-SPRFM in **Fig.** 5.14 demonstrates the FWHMs of both SW-SPRF and SW-SPRD are more than twice narrower than those of deconvoluted SPRF PSFs and more than three times narrower that those of the original doughnut-shape PSFs.

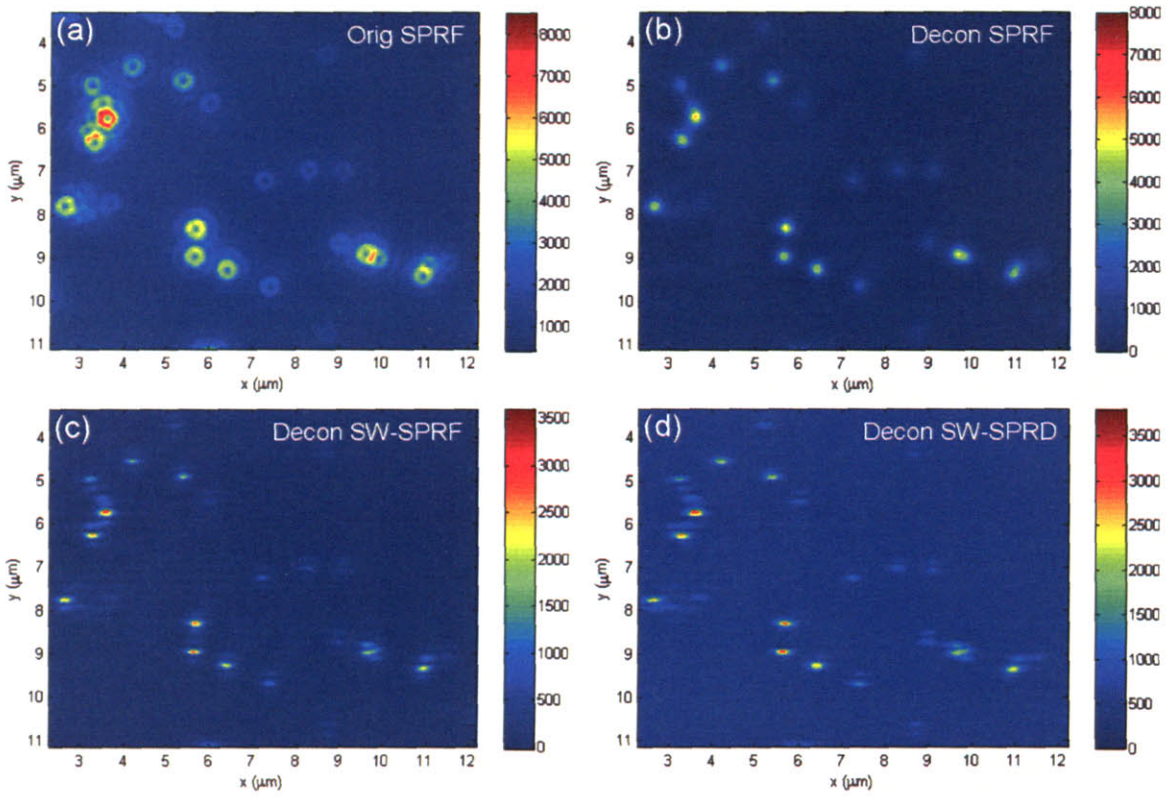

Fig. 5.13 Extended resolution imaging with 1D Standing wave surface plasmon resonance fluorescence microscopy (SW-SPRFM):
(a) Original SPRF image with unique doughnut-shape PSFs, (b) the deconvoluted SPRF image after deconvolution with a theoretical PSF kernel, (c) the SW-SPRF image with the SW-TIRF algorithm using three deconvoluted SPRFs at three SW phases, and (d) SW-SPRF image with linear deconvolution (Sample: 0.04μm fluorescenct microspheres, evanescent standing wave in vertical direction, Deconvolution algorithm: Richardson-Lucy algorithm using Matlab Image Processing Toolbox)

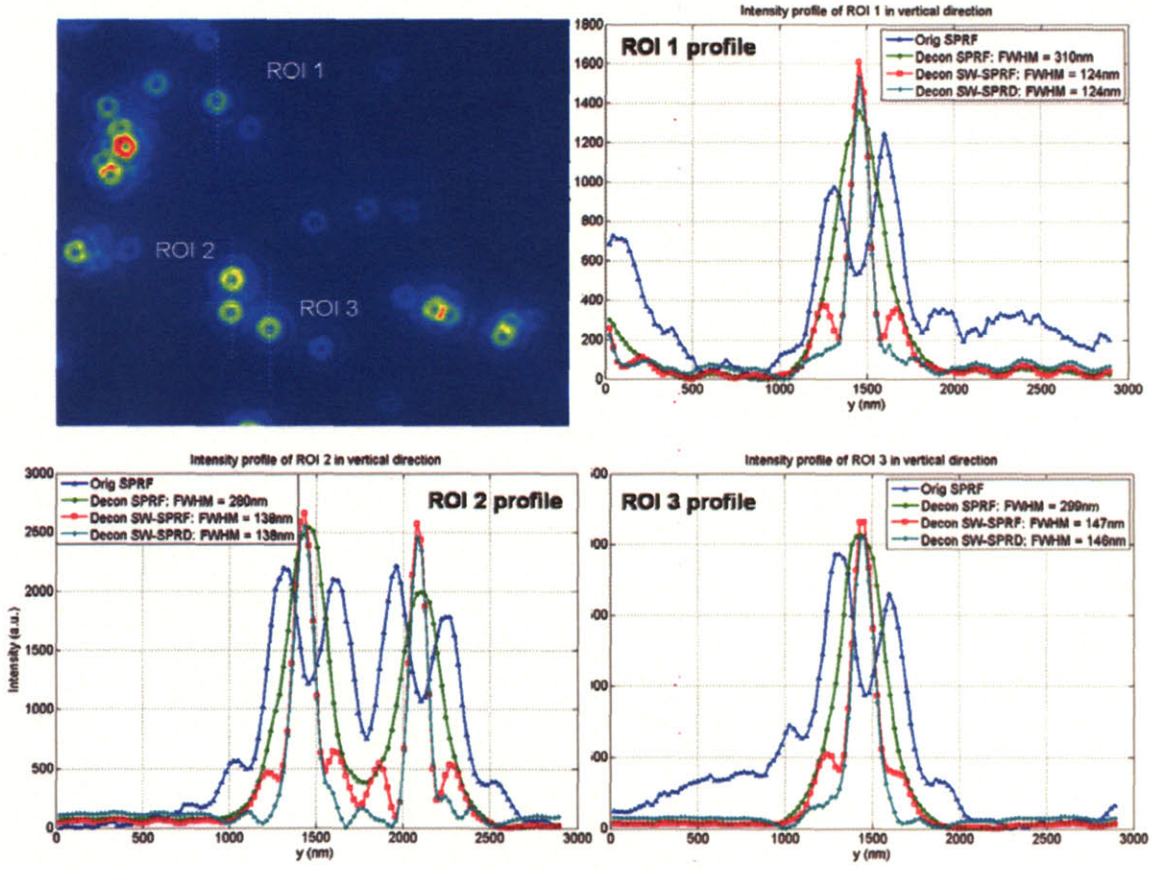

Fig. 5.14 The profiles of SW-SPRFM PSFs at selected regions of interest (ROIs). Top left image shows the original one SPRF image of spread beads. The vertical intensity profiles of the original SPRF, deconvoluted SPRF, SW-SPRF and SW-SPRD is compared. (The SW-SPR fringe period: 244nm)

5.5.4 General comparison of SW-SPRF and SW-TIRF with S- and P-polarization excitations

The capability of generating SW-TIR and SW-SPR excitation with both S-pol and P-pol beam respectively leads to a question of the comparison between these methods. In this section, the transmitted intensity at the interface above the substrate, i.e. the coverslip glass for TIRF and metal film coating for SPRF, will be compared and the exponential decaying profile is also studied.

The refractive index of a coverslip glass $n_1 = 1.52$, a medium $n_3 = 1.0$, and a thin gold film coating (50nm) $n_2 = 0.32 + j\,2.83$ with 532nm laser excitation in the case of SW-SPRF are assumed. The laterally averaged standing wave intensities at $z = 0$ can be expressed as follows. Note that these standing wave results turn out to be the same as the non-standing wave cases.

For SW-SPRF case:

$$\bar{I}^{P}_{SW-SPRF} = \left(\frac{n_1}{n_3}\right)^2 |\tau_P|^2 \left(2\sin^2\theta - (n_3/n_1)^2\right) \tag{5.5}$$

$$\bar{I}^{S}_{SW-SPRF} = |\tau_S(\theta)|^2 \tag{5.6}$$

$$\bar{I}^{P}_{SW-TIRF} = |t_P(\theta)|^2 \left(2\sin^2\theta - (n_3/n_1)^2\right) \tag{5.7}$$

$$\bar{I}^{S}_{SW-TIRF} = |t_S(\theta)|^2 \tag{5.8}$$

where the Fresnel coefficients τ_P is defined in Eqn. (5.2) and τ_S can also be defined by replacing P with S in the same formula. However, care must be taken since the two layer

Fresnel coefficients have different forms depending on the polarization. t_P and t_S are defined in Eqns. (2.31) and (2.26) in Section 2.3.1.

The transmitted intensities are plotted in **Fig.** 5.13(a) with physical parameters found in our current setup. Intensities are plotted since the fluorescence is usually proportional to the intensity on the fluorophores except there is a known quenching effect near to the metal coatings (Hellen and Axelrod, 1987). For SW-TIRF case, the maximum intensity enhancement occurs at the critical angle. However, a higher incidence angle is preferred in SW-TIRF for higher resolution and thus this enhancement effect may not be utilized. On the other hand, for SW-SPRF case, the enhancement is more than 23 times with P-polarized light near the SPR angle. It is also notable that both S-pol SW-TIRF and SW-SPRF do not have as much enhancement effect as their counterparts. Especially, the enhancement in S-pol SW-SPRF is close to zero which depends on the wavelength and material constants. This also explains the unique dependence of SPR with P-polarized light.

While **Fig.** 5.13(a) only shows the transmitted intensity at $z = 0$, **Fig.** 5.13(b) shows the exponentially decaying nature of the intensities assuming at SPR angle. Though all the intensity profiles have the same penetration depths, the images from different modes may not be the same. The SW-SPRF in P-pol has the highest enhancement and also the signal detected may contain information from farther regions then SW-TIRF imaging modes.

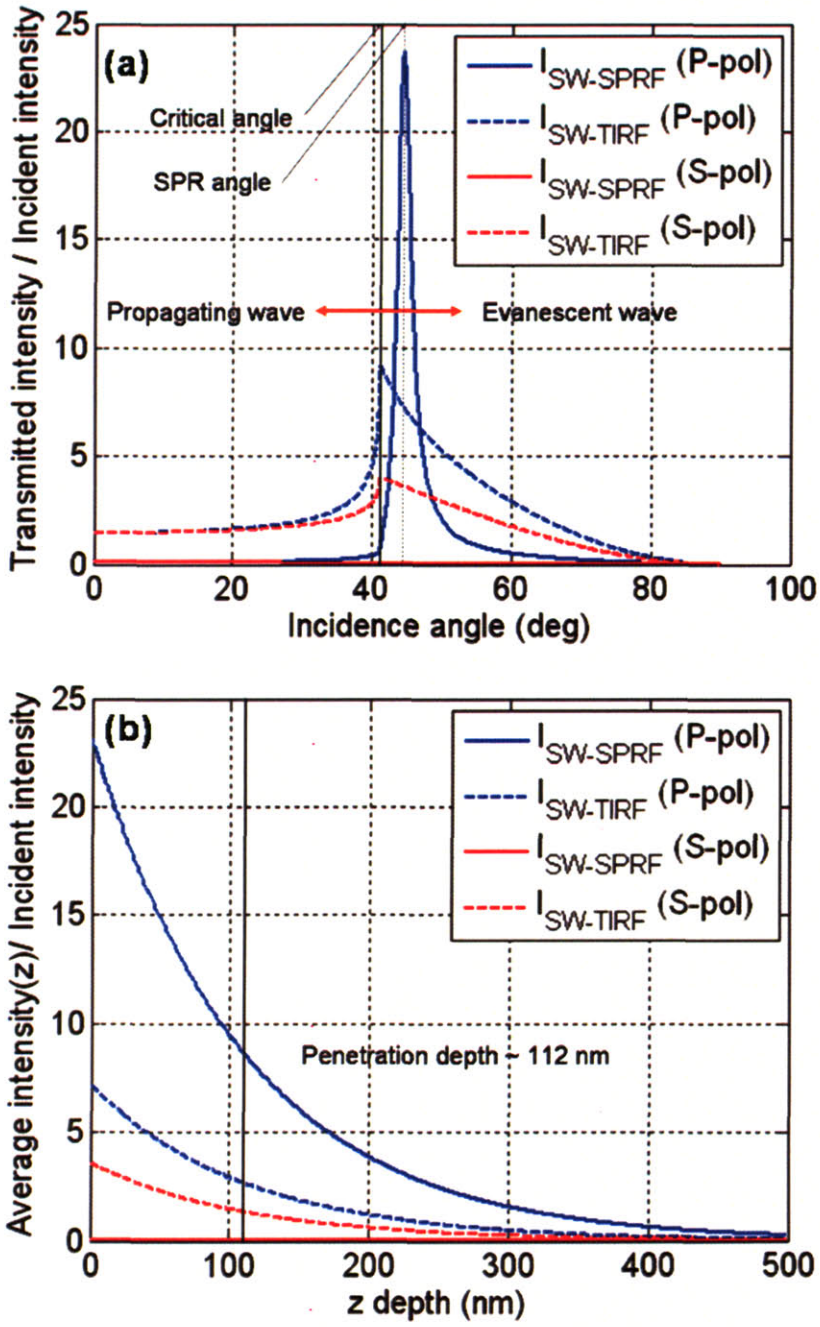

Fig. 5.13 (a) Transmitted intensities at $z = 0$ with respect to the incidence angle for the cases of SW-SPRF and SW-TIRF for S- and P-polarization incident light. Assuming the incident intensities in the glass are set to unity, the transmitted light is either evanescent for incidence angle greater than the critical angle or propagating otherwise.
(b) Average intensities relative to the incident intensities at different depths. All the intensities decay exponentially with the same penetration depth. (Simulation conditions: $n_1 = 1.52$ (coverslip), $n_2 = 0.32 + j2.83$ for Au at 532nm and $n_3 = 1.0$; $\theta_{cr} = 41.1°$, $\theta_{SPR} = 44.7°$)

5.6 Conclusions

Through back and front focal plane imaging, the conditions of SPCE were determined in our SPRF microscope which has unique characteristics by slight modification of the sample substrate from the conventional TIRF microscope. Using a P-polarized excitation beam at the SPR angle, the PSF of SPRF microscope was obtained and compared with the theoretical modeling. Furthermore, the unique SPRF PSF exhibits a doughnut-like structure with concentric rings. This irregularity was compensated with deconvolution for further application of SW-SPRF microscopy.

The already established SW-TIRF microscope was built based on S-polarized excitation light including crucial feedback control of the invisible evanescent standing wave. The known phenomenon of electric field cartwheeling makes an understanding of P-polization SW-TIRF more challenging. However, the formulation and simulation of the evanescent electric field revealed that standing wave can be produced even with P-polarization light. Fortunately, the P-polarization standing wave on the originally S-polarization based detector can still control the standing wave phase and thus allows us to try P-pol SW-TIRF. At the same time, the exploration of SPR by only replacing the coverslip glass coated with metal showed significant signal enhancement while suppressing the background. The unique nature of SPCE gave an unexpected doughnut-shape PSF. However, the seemingly wider PSF still carries its original spatial frequencies of the typical PSF of the optical system and allowed us to apply SW-TIRF algorithm to realize SW-SPRF microscopy with an additional deconvolution step. This new methodology may opens a new way of imaging or sensing modalities with super-high resolution and high signal-to-noise ratio due to still relatively unexplored nonlinear behaviors of surface plasmon coupled emission.

Arnoldus, H.E., and Foley, J.T. (2004). Transmission of dipole radiation through interfaces and the phenomenon of anti-critical angles. J Opt Soc Am A-Opt Image Sci Vis *21*, 1109-1117.

Axelrod, D. (2001). Total internal reflection fluorescence microscopy in cell biology. Traffic *2*, 764-774.

Beaumont, V. (2003). Visualizing membrane trafficking using total internal reflection fluorescence microscopy. Biochem Soc Trans *31*, 819-823.

Borejdo, J., Calander, N., Gryczynski, Z., and Gryczynski, I. (2006a). Fluorescence correlation spectroscopy in surface plasmon coupled emission microscope. Opt Express *14*, 7878-7888.

Borejdo, J., Gryczynski, Z., Calander, N., Muthu, P., and Gryczynski, I. (2006b). Application of surface plasmon coupled emission to study of muscle. Biophys J *91*, 2626-2635.

Chung, E., Kim, D.K., and So, P.T.C. (2006). Extended resolution wide-field optical imaging: objective-launched standing-wave total internal reflection fluorescence microscopy. Opt Lett *31*, 945-947.

Gryczynski, I., Malicka, J., Gryczynski, Z., and Lakowicz, J.R. (2004). Radiative decay engineering 4. Experimental studies of surface plasmon-coupled directional emission. Anal Biochem *324*, 170-182.

Hellen, E.H., and Axelrod, D. (1987). Fluorescence Emission at Dielectric and Metal-Film Interfaces. J Opt Soc Am B-Opt Phys *4*, 337-350.

Kostov, Y., Smith, D.S., Tolosa, L., Rao, G., Gryczynski, I., Gryczynski, Z., Malicka, J., and Lakowicz, J.R. (2005). Directional surface plasmon-coupled emission from a 3 nm green fluorescent protein monolayer. Biotechnol Prog *21*, 1731-1735.

Lakowicz, J.R. (2004). Radiative decay engineering 3. Surface plasmon-coupled directional emission. Anal Biochem *324*, 153-169.

Lakowicz, J.R., Malicka, J., Gryczynski, I., and Gryczynski, Z. (2003). Directional surface plasmon-coupled emission: a new method for high sensitivity detection. Biochem Biophys Res Commun *307*, 435-439.

Malicka, J., Gryczynski, I., Gryczynski, Z., and Lakowicz, J.R. (2003). DNA hybridization using surface plasmon-coupled emission. Anal Chem *75*, 6629-6633.

Matsubara, K., Kawata, S., and Minami, S. (1988). Optical Chemical Sensor Based on Surface-Plasmon Measurement. Appl Optics *27*, 1160-1163.

Mattheyses, A.L., and Axelrod, D. (2005). Fluorescence emission patterns near glass and metal-coated surfaces investigated with back focal plane imaging. J Biomed Opt *10*, 6.

Raether, H. (1987). Surface plasmons on smooth and rough surfaces and on gratings (Berlin ; New York :, Springer-Verlag).

Schmid, E.L., Tairi, A.P., Hovius, R., and Vogel, H. (1998). Screening ligands for membrane protein receptors by total internal reflection fluorescence: The 5-HT3 serotonin receptor. Anal Chem *70*, 1331-1338.

Sonnleitner, A., Mannuzzu, L.M., Terakawa, S., and Isacoff, E.Y. (2002). Structural rearrangements in single ion channels detected optically in living cells. Proc Natl Acad Sci U S A *99*, 12759-12764.

Tang, W.T., Chung, E., Kim, Y., So, P. T. C., Sheppard, C. J. R. (2007). Investigation of the Point Spread Function of Surface Plasmon-Coupled Emission Fluorescence Microscopy. Opt Express. (In preparation)

Torok, P. (2000). Propagation of electromagnetic dipole waves through dielectric interfaces. Opt Lett *25*, 1463-1465.

Wolf, E. (1959). Electromagnetic Diffraction in Optical Systems. I. An Integral Representation of the Image Field. Proceedings of the Royal Society of London Series A, Mathematical and Physical Sciences *253*, 349-357.

6. Summary and Future Directions

6.1 Thesis summary

The main theme of this thesis was to develop a wide-field super-resolution optical microscopy methodology using sub-diffraction limit evanescent standing waves, with faster imaging speed over point-by-point approaches.

To this end, for the first time, we

- Formulated the general imaging theory for one- and two-dimensional standing wave total internal reflection fluorescence (SW-TIRF) microscopy.
- Designed, built and characterized a novel objective-launched SW-TIRF microscope.
- Devised a novel real-time feedback phase control circuit including an accurate phase detector for the evanescent standing wave, a piezo-based actuator to control phase shift and a micro-processor based PDI controller. Active phase control allows robust operation of our experimental system.
- Demonstrated the super-resolution capability of objective-launch SW-TIRF by point spread function measurements providing approximately 100 nm resolution.
- Applied SW-TIRF to imaging biological specimens revealing finer details of actin cytoskeleton structures over conventional imaging modalities.
- Explored theoretically the effect of excitation polarization and confirmed that P-polarization beams can form evanescent standing waves with enough contrast for SW-TIRF algorithm.
- Studied and confirmed the surface plasmon-coupled emission (SPCE) based on surface plasmon resonance by imaging both back focal plane and front focal plane.
- Found, inadvertently, the unique doughnut-shape PSF of surface plasmon resonance fluorescence (SPRF) microscopy.
- Modeled the unique nature of SPRF microscopic image formation and explained the observed PSF with vector field theory.

- Invented a new imaging method, called standing wave surface plasmon resonance fluorescence (SW-SPRF) microscopy, by combining SW-TIRF and SPRF.
- Demonstrated the enhanced resolution of SW-SPRF by PSF measurements and provide a general theoretical comparison with SW-TIRF with polarization effect.

6.2 Future directions

6.2.1 Investigation of further resolution improvements

Seeking further enhancement in resolution should be the most exciting direction for this project. It may require nonlinear modalities such as stimulated emission depletion (STED) which as the potential of adding providing additional resolution improvement by factor of 2 to 5, and multi-photon excitation can provide an additional favorable feature such as suppressing the side-lobes of the original SW-TIRF PSF by an order of magnitude(Hell and Wichmann, 1994; So et al., 2001). On the other hand, even higher-resolution with significantly enhanced excitation field was implied using surface plasmon based approach. By adapting nano-scale grating based launching techniques, SW-SPRF may find new applications in biomedical sensing and imaging field (Raether, 1987; Tetz et al., 2005).

From the perspective of point-spread function engineering, it has been shown that if the excitation field is translatable, the high-frequency information can be extracted from a set of images where the excitation fields have different displacement vectors. Since the Fabry-Perot spectroscopy utilizes the multiple-beam interference and has been shown to have higher resolving power than that provided by a grating monochromator. If one can devise how to convert this high spectral finesse into spatial finesse, this can provide a high spatial frequency containing periodic peaks with narrower than the diffraction limit leading to the high resolution Fabry-Perot microscopy.

6.2.2 New contrast mechanism using scattering mode of evanescent standing wave

The resolution of any imaging system depends on the signal-to-noise ratio which is ultimately limited by the number of collected photons. For fluorescence methods, this imposes an intrinsic limit to any approaches to improve resolution by decreasing the size of PSF due to a reduction of fluorophores in the volume. In this regards, the non-fluorescent or scattering version of SW-TIR a.k.a. standing wave total internal reflection scattering (SW-TIRS) with novel metal nanoparticles may open up broader applications.

Since the photon scattering process is instantaneous instead of having a finite lifetime as in fluorescence process, the signal photon production rate of metal nanoparticles in biological system is only limited by heating processes and can be orders of magnitude higher than fluorescence. This may provide enough signal-to-noise ratio for imaging. Furthermore, there is no concern of photobleaching with metal nanoparticles. These noble metal nanoparticles with very high scattering power may serve as fluorescent analogs in biology for SW-TIR imaging although the imaging process is coherent rather than incoherent as in typical fluorescence imaging (Yguerabide and Yguerabide, 1998a, b).

6.2.3 Multi-color imaging modality using quantum dots for biological study

We are currently developing a real-time SW-TIRF microscope for live cell imaging with multi-color capability. Semiconductor nanocrystals (quantum dots) may be suitable chromophores for long-term live cell imaging because of their excellent photostability and low photobleaching. Most importantly, different colors of quantum dots can be efficiently excited at a single excitation wavelength eliminating the instrumental complications of imaging using different colors and periods of standing evanescent waves (Wu et al., 2003).

However, quantum dots exhibits characteristic blinking behavior. This blinking could interfere with SW-TIRF microscopy where precise intensity information is needed for image reconstruction. This problem might be overcome by biochemical suppression methods (Hohng and Ha, 2004). This development could allow the study of dynamic processes of live cells such as cellular attachment or migration as well as endocytosis and exocitosis(Beaumont, 2003), at super-diffraction limited resolution and single molecular sensitivity.

6.2.4 Combination of image correlation spectroscopy and SW-TIRF

Interactions, distribution and movements of biomolecules are crucial in many processes regulating life. Fluctuations of fluorescent emission contain information about molecular associations and reactions. This information can be extracted from correlation spectroscopy techniques such as fluorescence correlation spectroscopy (FCS) or image correlation spectroscopy (ICS) (Magde et al., 1974; Petersen et al., 1993).

In general, the signal to noise ratio of correlation spectroscopy is inversely proportional to the number of particles in the focal volume. The novel SW-TIR based approach described here can push this technique further with an order of magnitude smaller focal volume of atto-liter by taking advantage of smallest evanescent excitation depth and improved lateral resolution. In addition, an autocorrelation analysis of spatial (and temporal) fluctuations so called ICS has emerged an attractive tool for biological imaging study due to its capability of providing information of the dynamic receptor distribution, aggregation and colocalization (Kulkarni et al., 2005). The use of high-resolution SW-TIR method allow higher signal-to-noise to better quantify even smaller cluster size as well as the study of molecules inside cells with higher concentration which was limited with the conventional method.

6.2.5 Application in the area of photolithography with high lateral resolution

Photolithography technology to pattern surfaces with high resolution has been the driving force underlying the rapid development of semiconductor technology. Among other approaches, laser interference lithography (IL) has been used extensively in the past for the production of periodic sub-micron structures for a variety of applications including interferometry, spectroscopy, metrological standards, and high density magnetic memory. IL is performed by exposing a photo-sensitive resist to a sinusoidally varying standing wave generated by the interference of two coherent monochromatic plane waves. Exposing the resist by a standing wave can produce a periodic grating with its periodicity determined by the wavelength and incidence angle of the interfering waves(Bloomstein et al., 2006).

We propose a standing wave total interflection lithography (SW-TIRL) which is basically the same as IL except the use of either total internally reflecting standing waves or surface plasmon resonance enhanced standing wave. This new technique has the potential to enhance the resolution of the gratings/grids further by the order of 50 nm and features as small as 20-30 nm are possible using deep UV ArF excimer laser with wavelength of 193 nm and high refractive index prism.

Beaumont, V. (2003). Visualizing membrane trafficking using total internal reflection fluorescence microscopy. Biochem Soc Trans *31*, 819-823.

Bloomstein, T.M., Marchant, M.F., Deneault, S., Hardy, D.E., and Rothschild, M. (2006). 22-nm immersion interference lithography. Opt Express *14*, 6434-6443.

Hell, S.W., and Wichmann, J. (1994). Breaking The Diffraction Resolution Limit By Stimulated-Emission - Stimulated-Emission-Depletion Fluorescence Microscopy. Opt Lett *19*, 780-782.

Hohng, S., and Ha, T. (2004). Near-complete suppression of quantum dot blinking in ambient conditions. J Am Chem Soc *126*, 1324-1325.

Kulkarni, R.P., Wu, D.D., Davis, M.E., and Fraser, S.E. (2005). Quantitating intracellular transport of polyplexes by spatio-temporal image correlation spectroscopy. Proc Natl Acad Sci U S A *102*, 7523-7528.

Magde, D., Elson, E.L., and Webb, W.W. (1974). Fluorescence Correlation Spectroscopy .2. Experimental Realization. Biopolymers *13*, 29-61.

Petersen, N.O., Hoddelius, P.L., Wiseman, P.W., Seger, O., and Magnusson, K.E. (1993). Quantitation of Membrane-Receptor Distributions by Image Correlation Spectroscopy - Concept and Application. Biophys J *65*, 1135-1146.

Raether, H. (1987). Surface plasmons on smooth and rough surfaces and on gratings (Berlin ; New York :, Springer-Verlag).

So, P.T.C., Kwon, H.S., and Dong, C.Y. (2001). Resolution enhancement in standing-wave total internal reflection microscopy: a point-spread-function engineering approach. J Opt Soc Am A-Opt Image Sci Vis *18*, 2833-2845.

Tetz, K.A., Rokitski, R., Nezhad, M., and Fainman, Y. (2005). Excitation and direct imaging of surface plasmon polariton modes in a two-dimensional grating. Appl Phys Lett *86*.

Wu, X.Y., Liu, H.J., Liu, J.Q., Haley, K.N., Treadway, J.A., Larson, J.P., Ge, N.F., Peale, F., and Bruchez, M.P. (2003). Immunofluorescent labeling of cancer marker Her2 and other cellular targets with semiconductor quantum dots. Nature Biotechnology *21*, 41-46.

Yguerabide, J., and Yguerabide, E.E. (1998a). Light-scattering submicroscopic particles as highly fluorescent analogs and their use as tracer labels in clinical and biological applications - I. Theory. Anal Biochem *262*, 137-156.

Yguerabide, J., and Yguerabide, E.E. (1998b). Light-scattering submicroscopic particles as highly fluorescent analogs and their use as tracer labels in clinical and biological applications - II. Experimental characterization. Anal Biochem *262*, 157-176.

Biographical Note of Euiheon Chung

Education

03 – 06 **Harvard University and Massachusetts Institute of Technology (MIT)** Cambridge, MA
Division of Health Sciences and Technology (HST)
Medical Engineering/Medical Physics Ph.D. Program Cellular and Molecular Medicine Track
Joint program between Harvard Medical School and collaborating MIT department, ME

01 – 03 **Massachusetts Institute of Technology, Department of Mechanical Engineering (ME)**

98 **Korea Advanced Institute of Science and Technology (KAIST)** Taejon, Korea
M.S. in Aerospace Engineering

96 **Korea Advanced Institute of Science and Technology** Taejon, Korea
B.S. in Aerospace Engineering and Minor in Physics (*Summa cum laude*)

Experience

01 – 06 **Massachusetts Institute of Technology, Peter So laboratory** Cambridge, MA
Concentrate on biomedical optics including optical instrumentation and microscopy
- Developed novel wide-field high-resolution microscopes using evanescent standing waves
- Involved in developing multi-focal multi-photon microscopy for multiple particle tracking
- Involved in developing fast-scanning two-photon microscopy for observing dynamic collapse of lateral intercellular space of human bronchial epithelial cells in collaboration with Nikola Kojic

06 Aug **Global Enterprise in Micro-Mechanics and Molecular Medicine (GEM4) Summer School**
Lab TA on Cytoskeletal Mechanics with Maxine jonas and Yang-Hyo Kim Cambridge, MA

06 Sum **Cambridge Devices (a medical devices startup)** Cambridge, MA
Intern engineer: Built, characterized prototype polarization-based imaging devices to guide surgeons during excisional biopsies of skin cancers and performed preliminary clinical experiments with human skin cancer specimens from New England Medical Center

05 Spr **Massachusetts Institute of Technology, Dept. of Mechanical Engineering** Cambridge, MA
Lab TA of a semester course," System Dynamics and Control" for undergraduate ME major
- Prepared laboratory class lectures and experiments, and grading of lab reports

98 – 01 **Korea Air Force Academy, Department of Aerospace Engineering** Chungbuk, Korea
Full-Time Instructor and Korea Air Force officer
- Lectured Air Force cadets college engineering courses over 6 semesters

96 – 98 **KAIST, Propulsion and power systems laboratory** Taejon, Korea
Research Assistant: Numerical simulation and modeling of turbulent flame propagation

94 Win **Daewoo Heavy Industry, Aerospace Division** Changwon, Korea
Intern, Remotely Piloted Vehicle group for Korean Domestic Airplane Design Project

93 Sum **System Engineering Research Institute** Taejon, Korea
Intern, Computer Aided Design/Engineering division, developed fatigue-diagnosis software

Military Service

98 – 01 Full-time instructor and 1st & 2nd lieutenant of the Korea Air Force

98 Spr Air Force Officer Training Camp and Company Leader of over 330 cadet officers

Honors and Prizes

06 Jul	Gordon Research Conferences on Lasers in Medicine and Biology Active Participant Award, Plymouth, NH ($300 award)
06 Mar	Optical Society of America Biomedical Optics Topical Meetings Student Poster Award, Fort Lauderdale, Florida (ranked in the top 3 presentations in the related category of presentation with $500 NSF award)
06 Feb	Silver Prize, Samsung Electronics *Humantech* Thesis Prize Seoul, Korea ($5000 award)
03 - 05	HST Graduate Fellowship by Medical Engineering and Medical Physics Ph.D. Program
01 – 04	Involved in diverse intercultural activities as a *Rotary International Ambassadorial Scholar*
98 Sum	Ranked top in the Air Force Academic Instructor Course at Korea Air Force College
96	Graduated with honor (*Summa Cum Laude*) from KAIST
92 – 95	Received Honorary Student Scholarship from KAIST

Publications

Refereed Journal Articles:

1. **E. Chung**, Y. Kim, W. T. Tang, CJR Sheppard and PTC So, "Standing Wave Surface Plasmon Resonance Fluorescence Microscopy," (In preparation)
2. W. T. Tang, **E. Chung**, Y. Kim, CJR Sheppard and PTC So, "Investigation of the Point Spread Function of Surface Plasmon Coupled Emission Fluorescence Microscopy," (In preparation)
3. **E. Chung**, D. Kim, Y. Cui and PTC So, "Super-resolution imaging with standing evanescent wave fluorescence excitation for biological imaging," *Biophysical Journal,* (Under revision)
4. **E. Chung**, D. Kim and PTC. So, "Extended resolution wide-field optical imaging: Objective-launched standing wave total internal reflection fluorescence microscopy," *Optics Letters,* **31**, 945-947 (2006).
5. **E. Chung** and Sejin Kwon, "The Effect of Volume Expansion on the Propagation of Wrinkled Laminal Premixed Flame," *Combustion Science and Technology*, Vol. 146, pp. 85-103, 1999
6. **E. Chung**,"The Interaction of Vortex and Premixed Flame," *Journal of Korea Air Force Academy*, No.44, pp.229-244, 1999
7. **E. Chung** and Sejin Kwon, "The Interaction of Vortex and Premixed Flame with Consideration of Volume Expansion Effect," *Journal of Korean Society of Mechanical Engineering (KSME)*, Vol. 22, pp. 230-243, 1999

Conference Proceedings:

1. **E. Chung**, W. T. Tang, Y. Kim, CJR Sheppard and PTC So," Towards the Standing Wave Surface Plasmon Resonance Fluorescence Microscopy," *Photonics West, The International Society for Optical Engineering Biomedical Optics (SPIE BiOS)*, San Jose, CA, Jan., 2007
2. W. T. Tang, **E. Chung**, Y. Kim, CJR Sheppard and PTC So," Effects of using a metal layer in total internal reflection fluorescence microscopy," *International Workshop on Plasmonics and Applications in Nanotechnologies*, Singapore, Dec., 2006
3. **E. Chung**, D. Kim and PTC So,"Toward the Development of Wide-field Super-Resolution Microscopy by Use of Standing Evanescent Waves," *The 4th International Symposium on Nanomanufacturing,* MIT, Cambridge, MA, Nov., pp. 177-180, 2006
4. N. Kojic, **E. Chung**, D. Tschumperlin," Dynamic Geometric And Autocrine Signaling Events In Basolateral Epithelial Microenvironments," *Biomedical Engineering Society Annual Fall Meeting,* Chicago, IL, Oct., 2006
5. **E. Chung**, W. T. Tang, C. Sheppard and PTC So," Towards the Surface Plasmon Resonance Fluorescence Microscopy," *Biomedical Engineering Society Annual Fall Meeting,* Chicago, IL, Oct., 2006
6. **E. Chung**, D. Kim, Y. Cui and P. T. C So, "Super-resolution wide-field optical microscopy using standing evanescent waves for biological imaging," *Gordon Research Conference on Lasers in Medicine and Biology,* Plymouth, NH, July, 2006 (**Active Participant Award**)

7. **E. Chung**, D. Kim and P. T. C So, "Super-resolution Wide-field Imaging: Objective-launched Standing Wave Total Internal Reflection Fluorescence Microscopy," *Optical Society of America Biomedical Optics 2006 Topical Meeting,* Fort Lauderdale, FL, Mar. 2006 **(Graduate Student Poster Award)**
8. **E. Chung**, D. Kim and P. T. C So, "Ultra-high Resolution Optical Imaging beyond the Diffraction Limit by use of Standing Evanescent Wave," *Samsung Electronics Humantech Thesis Prize*, Seoul, Korea, Feb., 2006 **(Silver Prize)**
9. **E. Chung**, D. Kim and PTC So, "Super-resolution wide-field optical microscopy using standing evanescent waves," *Biomedical Engineering Society Annual Fall Meeting,* Baltimore, MD, 2005
10 N. Kojic, **E. Chung**, M. Kojic, J. M. Drazen and D.J. Tschumperlin," Numerical Modeling of Ligand Dynamics in he Compliant Intercellular Space Separating Airway Epithelial Cells," *Harvard-MIT Divisiton of Health Sciences and Technology (HST) Forum,* Boston, MA, Mar. 2005
11. **E. Chung** and PTC So ," Object-launched Standing Wave Total Internal Reflection Microscopy," *Harvard-MIT Division of Health Sciences and Technology (HST) Forum,* Boston, MA, Mar. 2005
12. Y. Y. Chen, M. Jonas, **E. Chung**, H. Huang and PTC So ,"Three Dimensional Multiple Particle Tracking with the Cylindrical-Optics-Induced Aberration in Multifocal Multiphoton Microscopy," *Biophysical Society 49th Annual Meeting*, Long Beach, CA, Feb. 12-16, 2005
13. **E. Chung**, D. Kim and PTC So, "Objective-launched Standing Wave Total Internal Reflection Microscopy," *Biophysical Society 49th Annual Meeting*, Long Beach, CA, Feb. 12-16, 2005
14. **E. Chung**, D. Kim and PTC So, "Ultra-High Resolution Optical Imaging beyond the Diffraction Limit," *The 2nd International Symposium on Nanomanufacturing,* KAIST, Daejeon, Korea, Nov., pp. 158-163, 2004
15. N Kojic, M Kojic, **E. Chung**, PTC So, JM Drazen, DJ Tschumperlin , "Numerical modeling of ligand dynamics in the compliant intercellular space," *Biomedical Engineering Society Annual Fall Meeting,* Philadelphia, PA, October, 2004
16. **E. Chung** and PTC So, "Lateral Resolution Enhancement in Standing-Wave Total Internal Reflection Microscopy using High NA objective lens," *Gordon Research Conference on Lasers in Medicine and Biology,* NH, July, 2004
17. **E. Chung** and PTC So, "Axially Resolved Wide-field Imaging without Degeneracy using Ultrafast Standing Wave Microscopy," *Biophysical Society 47th Annual Meeting*, San Antonio, TX, March 1-5, 2003
18. **E. Chung** and PTC So, "Lateral Resolution Enhancement in Standing Wave Total Internal Reflection Microscopy," *Gordon Research Conference on Lasers in Medicine and Biology,* NH, July 14-19, 2002
19. **E. Chung** and Sejin Kwon, "The Effect of Volume Expansion on the Propagation of Wrinkled Laminar Premixed Flame," *AIAA/ASME/ASEE Joint Propulsion Meeting*, AIAA Paper 98-3088, Cleveland, OH, 1998
20. **E. Chung** and Sejin Kwon, "The Interaction of Vortex and Premixed Flame with Consideration of Volume Expansion Effect," *KSCFE (The Korean Society for Computational Fluid Engineering) Proceedings of Fall Conference*, Nov., 1998
21. **E. Chung** and Sejin Kwon, "The Effect of Volume Expansion on the Propagation of Laminal Premixed Flame," *KSAS (The Korean Society for Aeronautical and Space sciences) Proceedings of Fall Conference*, Nov., 1997

Extracurricular Activities

05 – 06 President, "*MIT Korean Graduate Student in Mechanical Engineering (KGSAME).*" Created webpage, initiated *Monthly KGSAME Newsletter* and organized *KGSAME lecture series.*
04 – 06 *MIT Kouk Sun Do club* member and instructor practicing traditional Korean yoga
02 – 04 *MIT Dan Yoga Meditation club* member
01 Fall Trained in Tai Chi and Chi Kung course, MIT Medical
94 – 01 Taught meditation as a master-instructor to various groups including students and colleagues
95 – 96 President, "*KAIST Dan Meditation Club,*" Editor-in-chief of a monthly "*Han Culture News*"